Digital Twin of an isolated DC/DC converter for electrolysis

Msc SET Thesis project EEMCS

N. Lock

Delft University of Technology

TU Delft

Digital Twin of an isolated DC/DC converter for electrolysis

by

N. Lock

To obtain the degree of Master of Science at the Delft University of Technology,
to be defended publicly on 28/9/2023 at 14.30.

Thesis supervisor:	P. Bauer
Daily supervisors	A. Shekhar, H. Vahedi
Daily co-supervisor	R. S. Deshmukh
Project Duration:	December, 2022 - September, 2023

MSc Sustainable Energy Technology
Faculty of Electrical Engineering, Mathematics & Computer Science Delft
Research group of DC Systems, Energy, Conversion & Storage

An electronic version of this thesis is available on https://repository.tudelft.nl/

Cover: From online article "Europe's energy crisis is boosting green hydrogen. Is it finally a real alternative?" [1]

TU Delft

DCE&S
DC systems, Energy conversion & Storage

Acknowledgements

This thesis report conveys my work on the development of a Real-Time Digital Twin for a DC/DC converter for electrolysis. The document is made in order to gain the degree of Master of Science by graduating from the master track of Sustainable Energy Technology (SET) at Delft University of Technology. The work is performed as a part of the DC Systems, Energy Conversion and Storage (DCE&S) group of Delft University of Technology. This group focuses on the design, analysis, and applications of DC systems for energy conversion, distribution and transport via DC networks, and the integration of (electrical) energy sources using power electronics. This thesis is written and intended for people interested in the subjects of power electronics, green hydrogen production, electrolyzers, DC/DC converters, and Digital Twin.

This master thesis would not have been possible without the help of many people, yet one person's efforts truly stand out. I would like to thank Rohan Deshmukh for his unconditional support, patience, and help during this thesis. Working together on this project has been a great honor. I strongly believe that the work that we have performed can impact power electronic designs all over the world. I wish you good fortunes with the continuation of this research during your Ph.D.

I want to express my gratitude to the following professionals of the Delft University of Technology. Thank you, Aditya Shekhar, for providing guidance and advice during my thesis as the daily supervisor. You have helped me to see the right path more clearly with each step along the way. Your critical view and positive reinforcement have prevented me from going astray. I would like to thank both Gautam Rituraj and Hani Vahedi for helping out during this thesis and providing their insights. I would like to thank Pavol Bauer, my thesis supervisor, for being the chair of my thesis committee. I would like to Patrizio Manganiello for being a part of my thesis committee as the external member. Lastly, thank you Sharmilla Rattansingh for helping schedule my thesis.

I want to thank my colleague students Aashay and Abheek for our fruitful discussions about our topics and relaxed working environment. Foremost, I would like to thank my girlfriend, Anaïs for encouraging and supporting me personally during my thesis. Lastly, I would like to thank my parents Dick & Joke, and brother Joris for cheering me on during my thesis period.

I thoroughly enjoyed performing the work done in this thesis. Likewise, I hope this thesis will spark your interest in hydrogen, DC/DC conversion and Digital Twin technologies.

N. Lock
Delft, September 2023

Abstract

To utilize electronic power converters for water electrolysis in industrial electrical networks, reliable testing methods are required to ensure safe control operation as malfunctions can instigate hydrogen explosion and fierce electrical hazards. In this thesis, Digital Twin modeling via OPAL-RT software and hardware is compared to Simulink and PLECS simulation methods by creating the same power-to-power hydrogen network for all three with a Dual Active Bridge, a Medium Voltage DC grid, and an Alkaline electrolyzer whilst utilizing PI control via single phase shift modulation.

The Digital Twin model showed great control tuneability, while the PLECS model showed superior control performance, modeling complexity, error occurrence, and time-based performance for the designed specifications. It was concluded that the Digital Twin model needs to be developed further or reassessed to outperform the other modeling methods. The recommendations made included re-evaluating the OPAL-RT Digital Twin results for different signal measurement methods and validating the OPAL-RT Digital Twin's performance by comparing the results with other Digital Twin brands. Future work suggestions included creating a hardware-in-the-loop system and expanding on the current network design to include all components of a power-to-power hydrogen network.

Contents

List of Figures

List of Tables

Nomenclature

Abbreviations

Abbreviation	Definition
AEC	Alkaline Electrolyzer Cell
AI	Analog In
AO	Analog Out
COP	UN Climate Change Conference
CPU	Central Processing Unit
CTRL	Control
DAB	Dual Active Bridge
DC/DC Converter	Direct Current to Direct Current converter
DI	Digital In
DO	Digital Out
DT	Digital Twin
EC	Electrolyzer Cell
EL	Electrolyzer
EPS	Extended Phase Shift
FB	Full Bridge Converter
FC	Fuel Cell
FET	Field Effect Transistor
FPGA	Fully Programmable Gate Array
FCN1	Matlab Function Block 1
FCN2	Matlab Function Block 2
GUI	Graphical User Interface
HB	Half Bridge Converter
HIL	Hardware in the loop
HV	High Voltage
IGBT	Insulated-gate bipolar transistor
LV	Low Voltage
MOSFET	Metal-oxide-semiconductor field-effect transistor
MVDC	Medium Voltage Direct Current
NASA	National Aeronautics and Space Administration
PEMEC	Proton Exchange Membrane Electrolyzer Cell
PI control	Proportional Integral control
PP	Push Pull converter
PV	Photovoltaic
P2PH	Power To Power Hydrogen
RTDT	Real Time Digital Twin
SOEC	Solid Oxide Electrolyzer Cell
SPS	Single Phase Shift
TPS	Triple Phase Shift
VRES	Variable Renewable Energy Sources

Symbols

Symbol	Definition	Unit
A_{elect}	Electrode surface area	m^2
a, b	Vapor constants	-
$a_{H_2O,KOH}$	Water activity of KOH solution	-
a_{rev}	Temperature to Voltage constants for electrolyzer reversible voltage calculation	V/K
b_{sat}	Maximum and minimum phase angle that the saturator lets through	°
C_{ano}	Electrolyzer anode capacitance	F
C_{cat}	Electrolyzer cathode capacitance	F
C_{dc}	Capacitance of the input capacitor of the DAB	F
C_{in}	Capacitance of the input capacitor of a converter	F
C_{o}	Capacitance of the output capacitor of the DAB	F
C_{x}	Capacitor in a circuit (x indicates a number)	
D	Duty Cycle	-
D_{x}	Diode in a circuit (x indicates a number)	
DT_{sw}	On time of the SPS signal	s
F	Faraday constant	$C\ mol^{-1}$
f_{sw}	Switching frequency	kHz
I_{stack}	Measured stack current of the electrolyzer	A
I_{Lk}	Measured current of the leakage inductor	A
$i_{\text{act(ano)}}$	Activation current anode	A
$i_{\text{act(cat)}}$	Activation current cathode	A
i_{cell}	Cell current	A
K_{i}	Integral Gain	-
K_{p}	Proportional Gain	-
L_{Llk}	Leakage inductance	μH
L_{o}	output inductor inductance	μH
M	Molar mass of 30% wt KOH	g/mol
M_{x}	MOSFET in a circuit (x indicates a number)	
N_s	Number of cells in an electrolyzer stack	-
n	Transformer turns ratio	-
n_{x}	Transformer turns ratio of one part of a transformer (x indicates a number)	
P_{abs}	5 Absolute pressure of the electrolyzer	bar
P_{diff}	The difference between the reference power and the actual stack power	W
P_{H2O}	Vapor pressure of the water present in the electrolyte	bar
P_{KOH}	Vapor pressure of KOH	bar
P_{rated}	Rated power	kW
P_{ref}	Reference power	W
P_{stack}	Stack power	W
R	Gas constant	$JK^{-1}mol^{-1}$
R_{d}	Drain resistance of the MOSFET	Ω
R_{dc}	Input resistance of the DAB	Ω
R_{int}	Internal resistance of the electrolyzer	Ω
R_{Llk}	Resistance of the leakage inductance	Ω
R_{m}	Magnetization resistance of the transformer	Ω
R_{o}	Output resistance of the DAB	Ω
r	Area-specific resistance of an electrolyzer cell	Ωm^2
s, t, v, w	Temperature dependent constants	-
T_{k}	Cell temperature	K
V_{dc}	Rated voltage of the MVDC grid	V

Symbol	Definition	Unit
V_{in}	Voltage of input voltage source of a converter	V
V_{rev}	Reversible electrolyzer cell voltage	V
$V^0_{rev,T}$	Initial reversible voltage, dependent on cell temperature in Celsius	V
V_{stack}	Stack voltage of the electrolyzer	V
$v_{act(ano)}$	Electrolyzer anode activation potential	V
$v_{act(cat)}$	Electrolyzer cathode activation potential	V
v_{int}	Ohmic potential of electrolyzer cell	V
x	sawtooth signal without any phase shift	-
X_{FCN1}	X output of FCN1 block	-
X_{FCN2}	X output of FCN2 block	-
y	sawtooth signal with 180 ° phase shift	-
Y_{FCN1}	Y output of FCN1 block	-
Y_{FCN2}	Y output of FCN2 block	-
z	Number of electrons in the reaction	-
ϕ	phase angle between HV and LV gate signals	°
ϕ_{PI}	phase angle output of the PI controller	°
ϕ_{rated}	phase angle between high voltage side and low voltage side gate signals at which rated power occurs through the Dual Active Bridge	°

1

Introduction

With the rise in variable renewable energy sources (VRES) in electrical networks, the hardship of keeping continuous green energy in electrical grids has risen as well. As solar (and wind) energy fades in and out during the day, a green generation shortage comes to pass. Currently, this void is filled by fossil-fueled generators. The other way around happens as well, VRES can over-generate during low demand which causes a loss of green energy. An example day where both shortage and overgeneration happen is depicted in Figure 1.1. In order to satisfy the electricity demand with these phenomena, hydrogen is widely proposed as an energy carrier to store the excess green energy and deliver it back whenever this is required. Advantages of using hydrogen include its ability to be stored for a long time and the possibility to transport it to areas in need of hydrogen [2]. This can be done using so-called Power to Power Hydrogen (P2PH) networks [3]. An example of a P2PH network is depicted in Figure 1.2. Here, hydrogen is produced using electricity in an electrolyzer. The hydrogen will then be stored in pressurized tanks. When the energy demand requires it, hydrogen is then used to generate electricity in a hydrogen fuel cell [4].

To fit the use of hydrogen in electricity networks, electrical conversion components are the key to making it work. The creation of hydrogen via water electrolysis requires low voltage and high currents which can lead to enormous stresses within the components of the converters when sized for industrial levels. These high stresses can be dangerous for the safety of the entire P2PH network as the failure of one device can lead to the failure of more. Hydrogen on itself is a gas that is highly flammable, leakage sensitive, and explosive when in large volume. Failures in electricity networks themselves can also lead to fire and explosions. To prevent any harm, the conversion devices should be rigorously tested and should have flawless control [5]. Digital Twins (DT) have great potential to help achieve this.

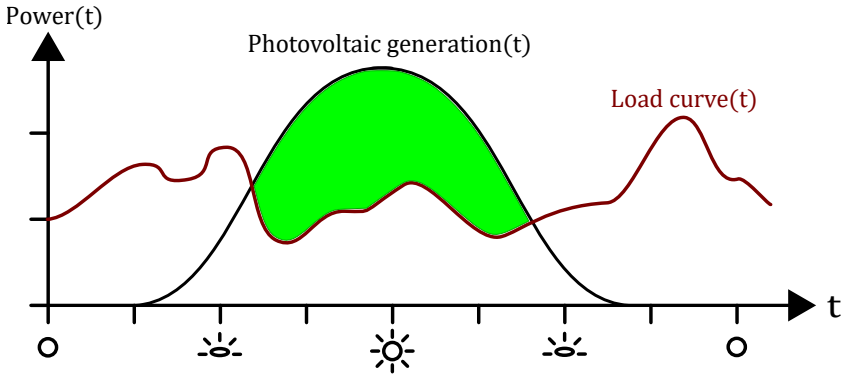

Figure 1.1: Generic network load curve versus photovoltaic generation during a day.

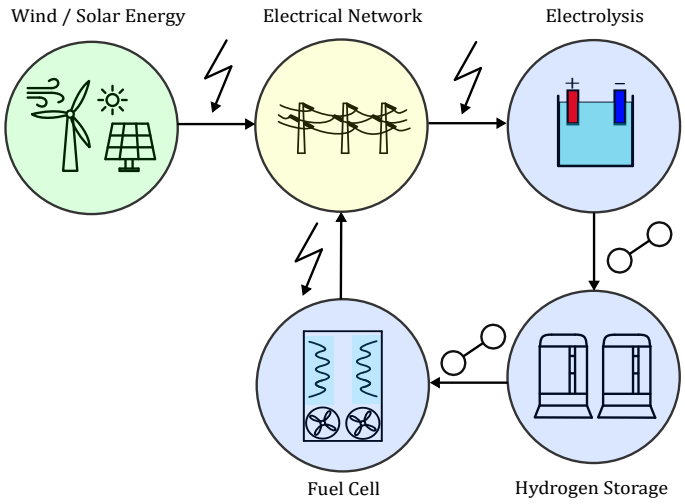

Figure 1.2: A generic P2PH network. The bolt symbol indicates an electrical conversion step and the molecule symbol indicates a hydrogen gas property conversion [3].

A DT is an up-to-date representation of a physical product in operation. When it reflects the product's condition in real-time, it is a Real-Time Digital Twin (RTDT). It uses the current and historical data to refine the control, predict future behavior, and/or optimize operation [6]. The first use of DTs can be traced back to NASA's Apollo mission [7]. Since then, the DT concept has evolved from the aerospace industry into many more industries such as agriculture, medicine, and energy. This has also led to the current evolved definition of the DT [8]. As many countries now want to reach their energy-related climate goals efficiently, inexpensively, and safely, DT technology has popped up in the energy industry. DTs can be used for numerous energy applications such as wind turbines, solar panels, and power converters [9]. On the last one, lies the focus for this thesis.

In this research, emphasis is put on the development of a RTDT of a power electronic converter for the application of high-power electrolysis in a Medium Voltage Direct Current (MVDC) grid. In order to make and test the RTDT, OPAL-RT real-time Simulators are used. Simulink and PLECS are used to validate the OPAL-RT model and to compare its performance. All models will use the same reduced P2PH network, which will ignore the storage, the fuel cell and the fuel cell converter(s). The system overview of the DC network used for this thesis is depicted in Figure 1.3 with the system under design highlighted. The MVDC grid is assumed to be a strong grid with 1400 V connection to the DC/DC converter. The rated power of the selected DC/DC converter will be 10 kW and its output voltage is aimed to be at 70 V.

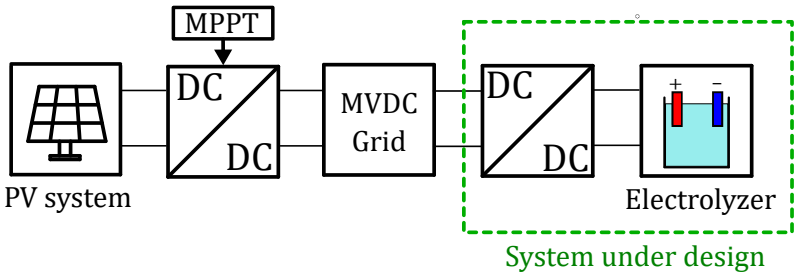

Figure 1.3: Reduced P2PH system considered for this thesis. The dotted green area indicates the components under design. The same area is considered within the development of both the Simulink and the DT models.

1.1. Research questions, challenges and objectives

This section discusses the setup for this thesis. It will go over the topics of research definition, the main research question, challenges, sub-research questions, and the intended goals and outcomes of this thesis. Lastly, an intended time frame is presented.

1.1.1. Main research question

The design and designing process of a power converter for MVDC grid to electrolyzer in a P2PH system have the following five main requirements:

Design requirements

- Efficient power transfer from the MVDC grid to the electrolyzer
- Robust design and control
- Capable of handling a high step-down voltage ratio
- The design, designing method, and testing ought to be cost-effective
- Designing and testing ought to be time-effective

Based on these requirements, the problem definition can be formulated as follows:

Problem definition *To utilize water electrolysis in MVDC grids, a high-step down voltage ratio power converter is required to connect the two. As high current and low voltage are required for water electrolysis, the power converter needs to have robust control. Hardware control tests at industrial level (component) sizes are dangerous as failure can lead to hydrogen explosion and/or electrical hazards. Therefore, the modeling method of the power converters is crucial to the robustness of the design.*

For this thesis, the RTDT approach is selected as a potential way of tackling the problem defined. To assess its viability, a Simulink model is also made for comparison. Simulink is a software application by MathWorks that is currently widely used in the industry to simulate power converters. To specify the research, the P2PH network of Figure 1.3 is used and the DC/DC converter in between the MVDC grid and the electrolyzer is used as a case study. This shifts the problem definition into the following main research question:

Main research question

- What is gained from utilizing an RTDT in comparison to simulation models in achieving a robust design for a DC/DC converter topology for electrolysis?

1.1.2. Challenges and sub-questions

The challenges in answering the main research question are as follows:

Challenges

- An appropriate DC/DC converter topology must be chosen
- The electrochemical characteristics of the electrolyzer must be defined
- The control strategy must be defined
- A modulation strategy must be chosen and modeled
- Establish criteria to compare the simulation and DT models.
- Software differences ought to be minimized when implementing the design.

Methods to implement the designs may differ per software, but the designs ought to have the same operation. For example, if both software require a pulse signal, the pulse signal may be generated using different methods as long as the generated pulse signals are the same for the DT as the Simulink model. This is to ensure that both models can be compared properly. The data relating to the two models' performance statistics will be taken as a key component of this research as they help answer the main research question.

From the challenges, the following sub-questions are made:

Research sub-questions

Design

- Which electrolyzer type should be used for the application?
- Which DC/DC Converter should be used for the application?
- What is the most optimal control and/or modulation strategy for the application?

Comparison

- What data will be used to compare the Digital Twin and Simulink models?
- How does the Simulink model perform for the application?
- How does the Real Time Digital Twin model perform for the application?

1.1.3. Research objectives and timeline

The intended outcome of this thesis is that at the end a Simulink model and an OPAL-RT model of the proposed system are present and their performance is compared. In order to reach this, objectives have been set to make a step-by-step plan. Below are the objectives listed in chronological order.

Research objectives

1. Determine the electrolyzer type to be used
2. Determine the DC/DC converter type to be used
3. Determine the modulation and/or control for the application
4. Determine and create the full system to be analyzed using the components determined
5. Create and execute a Simulink model for the selected combination of components, modulation and/or control
6. Create and execute an OPAL RT model for the selected combination of components, modulation and/or control
7. Create a comparison of the performances of the models
8. Conclusion and recommendations according to the performances of both models

These objectives, together with the deliverables required for completing the master thesis for the study Sustainable Energy Technology, are presented in the timeline in Figure 1.4. In this timeline, the objectives are enumerated in the same order as the list above. Each dot represents the deadline for each deliverable. The type of deliverable is color coded.

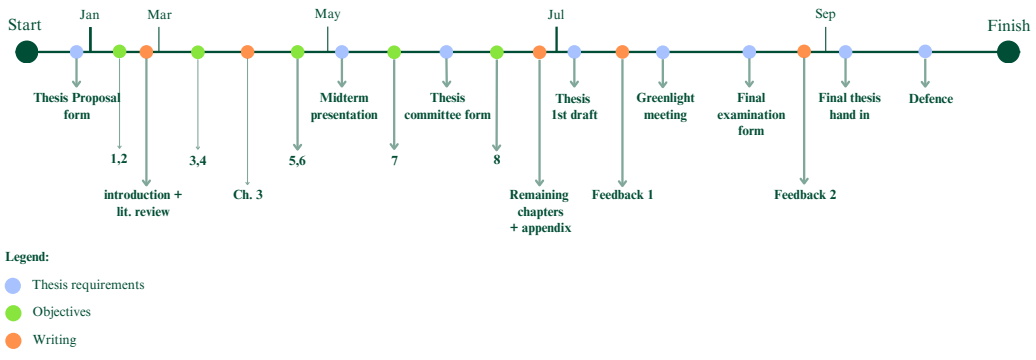

Figure 1.4: Thesis timeline from start to finish with Thesis requirements, objectives, and writing goals indicated.

1.2. Thesis Chapter composition

This thesis is divided into seven chapters, which are in line with the process of the design of DT and simulation models. In this section, the contents of each chapter are briefly presented.

In Chapter 2, the performed literature review is elaborated. The context and current position of hydrogen in the energy industry are explained in Section 2.1. Insights about the possibilities for the system design are elaborated in Section 2.2. The main focus is on the components electrolysis (Subsection 2.2.1), DC/DC converters (Subsection 2.2.2), and Digital Twin (Subsection 2.2.3). The research gap is defined in Section 2.3. Lastly, the conclusions of the literature are discussed in Section 2.4.

In Chapter 3, the system design is presented. This chapter introduces the full system overview, after which the system is split into different parts to elaborate on one by one. Each section following explains the choices, necessary calculations, and implementation approach of each component. Section 3.1 focuses on the electrolysis covering the choice for the type of electrolyzer (Subsection 3.1.1) and the implementation approach (Subsection 3.1.2). Section 3.2 presents the process of selecting the DC/DC converter (Subsection 3.2) and the implementation approach of the chosen design (Subsection 3.2.2). Lastly Section 3.3 discusses the chosen modulation strategy (Subsection 3.3.1) and control strategy (Subsection 3.3.2) to provide insight into the interaction of all the components.

Chapter 4 discusses the design implementation for the simulation models. The modeling approach of the Simulink model is explained in Section 4.1. The modeling approach for a model that utilizes both Simulink and PLECS is explained in Section 4.2.

Chapter 5 discusses the design implementation for the DT. The chapter presents how the model is made in OPAL-RT and the differences with the Simulink model per subsystem in each of the sections. With the fundamental modeling approach presented in Section 5.1, The modulation approach in Section 5.2, The introduction of the eHS toolbox in Section 5.3, The changes for the electrolyzer subsystem in Section 5.4 and for the control in Section 5.5.

The results of the models are presented and discussed in Chapter 6. The Simulink model output and results are presented in Section 6.1, followed by the PLECS model results in Section 6.2 and the DT model results in Section 6.3. The performance of the models is compared in Section 6.4.

In Chapter 7, the conclusions and recommendations of this thesis are presented. Section 7.1 presents the conclusions by answering the research questions presented in Section 1.1. Section 7.2 covers the recommendations that are built upon the findings of this thesis.

The appendices cover the used lines of code in the models and the detailed settings of each component (Appendix A), a guide on how to run the Digital Twin models (Appendix B), a log of the occurred errors and troubleshooting them (Appendix C) and the reference to the conference paper written alongside this thesis (Appendix D).

2

Literature Review

This chapter describes the literature found and the findings of the literature review, focusing on hydrogen, system design, and finding the research gap. The context and the current standings concerning climate change and green hydrogen production using water electrolysis are given in Section 2.1. Existing research on the components required for the system design is described in Section 2.2 focusing on electrolysis, DC/DC converters, and DT. Using the literature found, the research gap is determined and elaborated upon in Section 2.3. In Section 2.4 conclusions are drawn which are used to progress with the system design.

2.1. Context

In 2015 during the UN Climate Change Conference (COP), 196 parties signed the legally binding international treaty on climate change called the Paris Agreement to prevent a global temperature rise of 1.5 °C by the end of the century [10]. During COP27 in Sharm el-Sheikh 2022, the more recent developments since the Paris Agreement have been laid out and updated agreements have been made. For instance, to limit global warming to 1.5 °C, rapid, deep, and sustained reductions in global greenhouse gas emissions of 43% by 2030 (relative to the 2019 level) will be necessary. This decrease should be amongst all applicable sectors, including a thorough increase in low emission, renewable energy, energy transition partnerships, and/or cooperative actions [11].

Within the Dutch government, a coalition accord was reached which stated that the country goes for the extra mile. Using a new "Climate Law" the goal of 2030 is now to reach at least 60% CO_2 reduction. The same accord also states that a fund of 35 billion euros will be made available for the coming ten years to build a green infrastructure [12]. Because of these goals, the Dutch government foresees a great role for hydrogen in the energy transition. The ambition is to create a 500 MW electrolyzer capacity by 2025 and scale that up to a 4 GW capacity by 2030. The capacity will be financed using the National Growth Fund, which will earmark 20 million euros in the period of 2021-2025 [13].

The Hydrogen Roadmap made for [13], states that adequate focus for upscaling hydrogen technologies is required to reach the targets made by the Dutch ministry of climate change. This emphasizes research and innovations that can help improve the production hydrogen using of on- and off-shore VRES. The innovations are investigated, piloted and demonstrated towards 2030. In 2030, the central government will decide on how to proceed reaching their goals with the found innovations on electrolysis and with the 2030 demand of hydrogen [14].

2.2. System Overview

2.2.1. Electrolysis

There are three main forms of electrolyzers; Alkaline (AEC), Proton Exchange Membrane (PEMEC) and Solide Oxide (SOEC). A significant amount of literature have compared and described the three types [3, 15–20]. The common system characteristics found within the literature are described in Table 2.1. In Figure 2.1 the chemical characteristics of each type of electrolyzer have been described as found within the same literature. The flow of these reactions and the elements within each type of electrolyzer have been depicted as well. From Table 2.1, Figure 2.1 and the references [3, 15–20], advantages and disadvantages for each of the three systems have been summarized in Table 2.2. These findings are further explained in the following paragraphs for each type of electrolyzer separately.

Table 2.1: Characteristics of different water electrolysis technologies [3, 15–20]

Characteristics	**AEC**	**PEMEC**	**SOEC**
Operational parameters			
Temperature (°C)	40-90	20-100	650-1000
Pressure (bar)	<30	<200	<20
Current Density (A/cm^2)	0.20-0.40	0.60-2.00	0.30-2.00
Voltage (V)	1.80-2.40	1.80-2.20	0.70-1.50
Nominal features			
Production rate (m^3/h)	<1400	<400	<10
Gas purity (%)	>99.50	>99.99	>99.90
Cold start-up time (min)	>60	>5	>60
Warm start-up time (min)	1-5	<1	>15
System details			
Energy consumption (kWh/m^3)	~5.55	~5.40	~3.80
Electrolyzer efficiency (%)	63-71	60-68	100
System Efficiency (%)	51-60	46-60	76-81
Stack lifetime (kh)	60-120	60-100	8-20
Degradation (%/year)	0.25-1.50	0.5-5.50	3-50
Economic Parameters			
Capital cost (€/kWh)	740-1390	1300-2410	>2000
Yearly cost (% of investment)	2-3	3-5	n.a.

Table 2.2: Summarized electrolyser technology comparison

	AEC	**PEMEC**	**SOEC**
Advantages	Well established technology	Compact design	High electric efficiency
	High durability	Dynamic system response	Hydrogen cost
	Cost Effective	High pressures possible	Reaction kinetics
	High production rate	Operating temperature	Thermal integration
Disadvantages	Corrosive liquid electrolytes	Low availability	Large design
	Slow cold start up time	Use of scarce materials	Still in research phase
	Low hydrogen purity	Low durability	Long term stability
	Low dynamic operation	Maintenance costs	Expensive to make

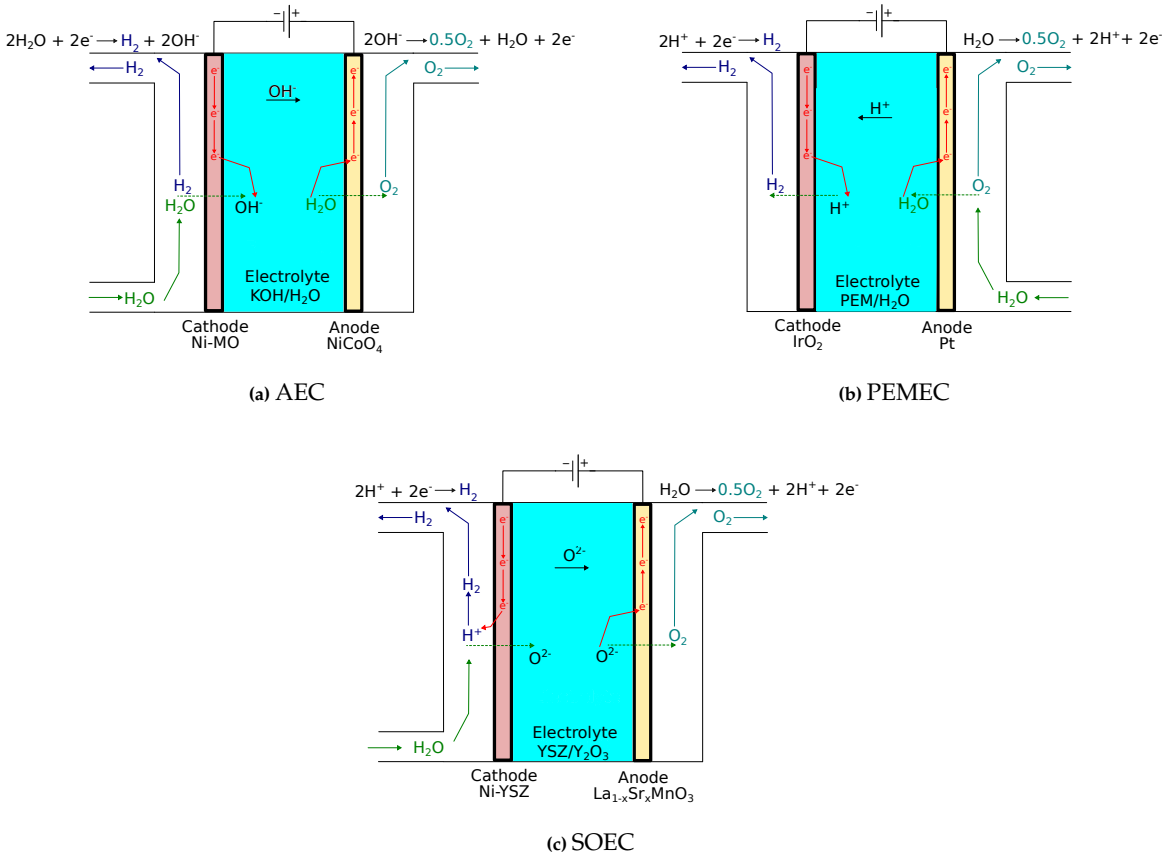

(a) AEC

(b) PEMEC

(c) SOEC

Figure 2.1: Chemical working inside of each electrolyzer type.

AEC can only operate at relatively low temperatures, pressure, and current density. However, AEC requires higher voltages per cell. It has the highest production rate out of the three but gets the lowest purity of hydrogen. The technology is a well-established technology which explains its relatively low costs to make and maintain operation. This gives the AEC its low degradation rate and high stack lifetime. AEC does however present the highest energy consumption to make hydrogen due to the mediocre electrolyzer efficiency and total system efficiency.

PEMEC presents a wider operating temperature range and higher pressure limits than AEC. The PEMEC system size can be kept small as the required cell area is much lower than AEC and the required materials are lightweight. Due to these properties, PEMEC is known for its very dynamic operation and quick start-up time. For its anode and cathode catalysts, PEMEC uses very rare materials. Iridium and Platinum are currently scarce which gives a huge boost in price for the complete system. This also gives PEMEC its low availability on the market.

SOEC is the newest technology out of the three, it is still in the research phase and very limited available on the market. The operational requirements are very steep for it as pressure needs to be low and temperature needs to be very high. These properties ask for a large balance of plant which significantly increase the size of the whole system of a SOEC. Due to the lack of maturity and the rough operating conditions, the life expectancy of the stack is very short and internal degradation is high. All of these properties combined make the current capital cost of a SOEC the highest out of the three. The SOEC does, however, present an amazing system efficiency that can lead to very cheap hydrogen. The high working temperatures allow for good reaction kinetics which gives SOEC its high efficiencies. SOEC technology can be thermally integrated with downstream chemical synthesis i.e. the production of methanol, dimethyl ether, and ammonia due to its temperature regiment [20].

2.2.2. DC/DC converters

In the literature, many types of DC/DC converters have been analyzed for electrolyzer use as well as for MVDC networks. Reference [21] reviewed isolated and non-isolated DC/DC converters for MVDC networks. The presented options mainly included Dual Active Bridge (DAB) (with variants) and Modular Multilevel Converters (MMC). Two tables (for isolated and non-isolated) were devised with recommendations of which to use and when. In [22], three specific types of DC/DC converters are compared for water electrolyzer and hydrogen fuel cell use. Full Bridge (FB), Half Bridge (HB), and Push Pull (PP) converters were taken into consideration for use with single-phase shift modulation (SPS). According to the authors, the FB was the best to use for systems of 3 kW or higher and was also deemed the most cost-effective and efficient. The HB and PP were recommended as feasible and effective when using systems of 1 to 3 kW. Reference [23] compared DC/DC converter topologies for electrolyzers in terms of output current ripple reduction, conversion ratio, energy efficiency, and power switch fault tolerance. Eight different DC/DC converters were reviewed consisting of mainly Buck converter variants (interleaved, stacked, quadratic etc.), HB, and FB. The HB was deemed most attractive for electrolysis, yet research into new DC/DC converter topologies was recommended. In, [24], research on interleaved Buck converters for electrolyzers was conducted and advantages and drawbacks for each topology. It was found that interleaved Buck converters offer more in terms of availability and output current reduction than regular Buck converters. Recommendations were made for which interleaved Buck converter to use when high voltage ratio, low current ripple, high efficiency, or high reliability is prioritized. In [15], the research for interleaved Buck converters was continued for PEMEC electrolyzers. The converters were compared for conversion gain, phase current ripple, and output current ripple. The most suitable converter for high voltage gain was found to be an interleaved Buck converter with coupled windings. In terms of availability and output current ripple point of view, the three-level interleaved step-down converter was found to be the most suitable for hybrid renewable energy systems with hydrogen storage based on a DC bus configuration.

Besides DC/DC converter comparison research, singular ideas for DC/DC converters for electrolysis in MVDC are also presented within the literature. For instance by using quadratic Buck converters [25], utilizing soft switching techniques in DAB [26], and combining multiple input sources in an input series output parallel converter [27]. The researched converters all add up to be variants or modulated versions of DAB, FB, HB, PP, or Buck converters. An overview of the found converters is depicted in Figure 2.2, where the size of each slice represents how many of a DC/DC converter topology were found in comparison to the total amount found in the literature [15, 21–27].

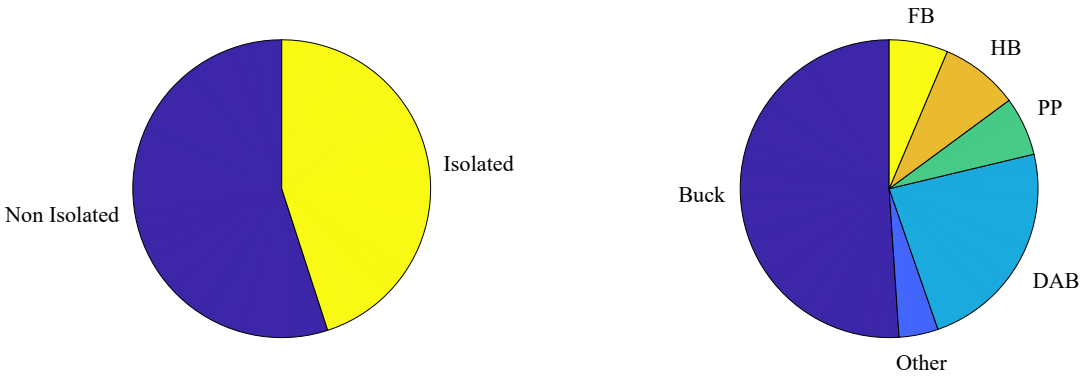

(a) Isolated vs Non Isolated topologies

(b) Topologies used

Figure 2.2: Pie charts of DC/DC converters types used in literature [15, 21–27] for MVDC and Electrolysis applications.

2.2.3. Digital Twin

A DT is a representation of an active unique product which can be a real device, object, machine, service, intangible asset, or a system consisting of a product and its related services. DTs provide seamless integration of the physical and the virtual machine in both directions [8]. The definition of a DT is visualized in Figure 2.3

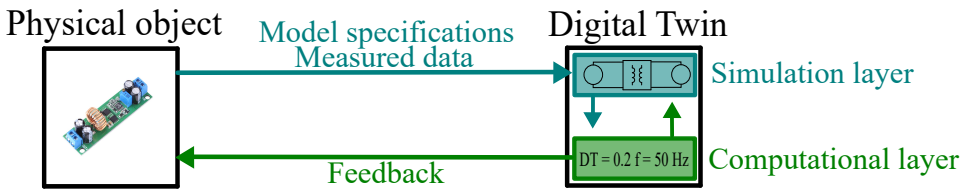

Figure 2.3: Digital Twin concept.

The concept of DT is relatively young as it was first proposed in 2003 and the first paper about DT was written in 2011. Michael Grieves published the first white paper on DT in 2014, which started the growth stage of DT [28]. DT is since then used in many industries ranging from engineering to agriculture and healthcare. Within engineering, uses of DT include design, optimization, real-time monitoring, enhancing operation processes, and predictive maintenance [29].

For water electrolysis, only three elaborate DT models have been made for multiple types of electrolyzers with different focuses. In reference [30], an 500 kW AEC DT was designed focusing on optimization of production cost. It was found that at high pressure, the process equipment costs increase, therefore, it was recommended to take a hydrogen compression stage from the electrolyzer to the storage into consideration to optimize electrolyzer operating conditions. Reference [31] depicted a PEMEC DT to design control strategies in order to suppress fluctuations and improve durability. It was found that a neural network predictive control strategy was able to suppress power overshoots by 92%. Another PEMEC DT was made in [32] in order to design a graphical user interface (GUI) with MATLAB App-designer. The interface allowed monitoring the most significant PEM WE operation parameters and comparing the values both numerically and graphically in real-time.

For DC/DC conversion, mainly DT models exist for predictive maintenance or condition monitoring [9] as for instance researched by [33–36]. Only two other notable research exist on DTs for the control of DC/DC converters. In [37] a proof of concept of a DT for fault detection within power converters is presented, which was validated using a Buck DC/DC converter interfaced with an external Texas Instruments DSP LAUNCHXL-F289D device. The study confirmed that the setup could indeed find faults for overvoltage, overcurrent, and overheating within the converter and can be developed further to find more types of faults. In [38] a DT for a PV system with DC/DC converter was designed which focused on fault detection and control. A traditional algorithm was tested alongside the DT and white noise was inserted to test the strength of both. The DT showed to have the best evaluation scores for F1-Score, precision, and recall.

2.3. Research Gap

A summary of the key findings for the research gap is listed. below Each of the findings is explained in the paragraphs after.

- The current demand for innovations and research in hydrogen technologies is high. The Dutch Ministry of Climate Change actively pursues new innovations and research until 2030.
- Electrolysis has been thoroughly covered in literature, except on the matter of electrochemical modeling.
- DC/DC converter designs vary per combination of input and output components, the choice process made in this thesis is therefore of value as the proposed component combination was not found in the literature.
- DT is a relatively young subject within the energy industry and DT models are discussed scarcely in energy-related papers. The components combination used in this thesis as a DT has not yet been published.

As described in Section 2.1, parties all across the globe are invested in reducing greenhouse gasses. Hydrogen has become part of the plans in doing so at a national and international level. The demand for electrolysis, hydrogen storage, and their possible innovations is rising within the Netherlands. With the hydrogen roadmap in mind, the Dutch Ministry of Climate Change actively pursuing new innovations and research until 2030. This shows that research within those fields is currently of high value.

Regarding electrolysis research, there was no research gap on information on the electrolyzer types themselves. The found literature provides enough insights to continue with choosing an electrolyzer type and rough specifications. However, the proposed application with the combination of PV, MVDC, and electrolyzer seems to be missing within the literature. The current literature mainly shows applications with solar/wind energy directly to electrolyzers, three-phase applications, or other specific electrical grids. Within the literature, various models for electrolyzers have been presented as well. Electrical models of electrolyzers are limited whilst chemical models appear more often in the literature.

As the selection of electrolyzer varies per application, the selection of A DC/DC converter does so as well. As chosen electrical schematics and networks vary, the most useful type of DC/DC converter varies as well. The literature mostly covers studies of DC/DC converter selection for an electrolyzer and for MVDC networks separately. The combination of MVDC networks and electrolysis that has not been found in DC/DC converter literature. Therefore, the selection process of DC/DC converter is of value.

For the energy industry, in 2022 only 35 papers on DT were known to have been made within the energy industry. [39] For comparison, the full division for all industries is depicted in Figure 2.4.

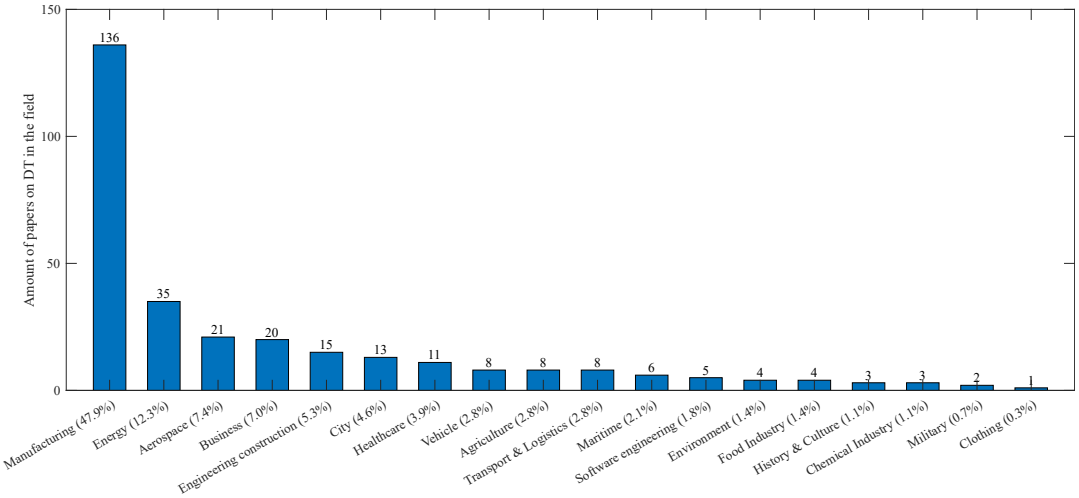

Figure 2.4: Field distribution conveyed within papers on Digital Twin Anno 2022, using the data of [39].

Although DTs have been utilized within the energy industry, the researched applications are still limited. DTs are mainly used for the function of visualization, optimization, and predictive maintenance, control is only known as the main function within 9.80% of all the papers on DT [39]. For comparison, the division of subjects for all papers on DT (Anno 2022) have been depicted in Figure 2.5.

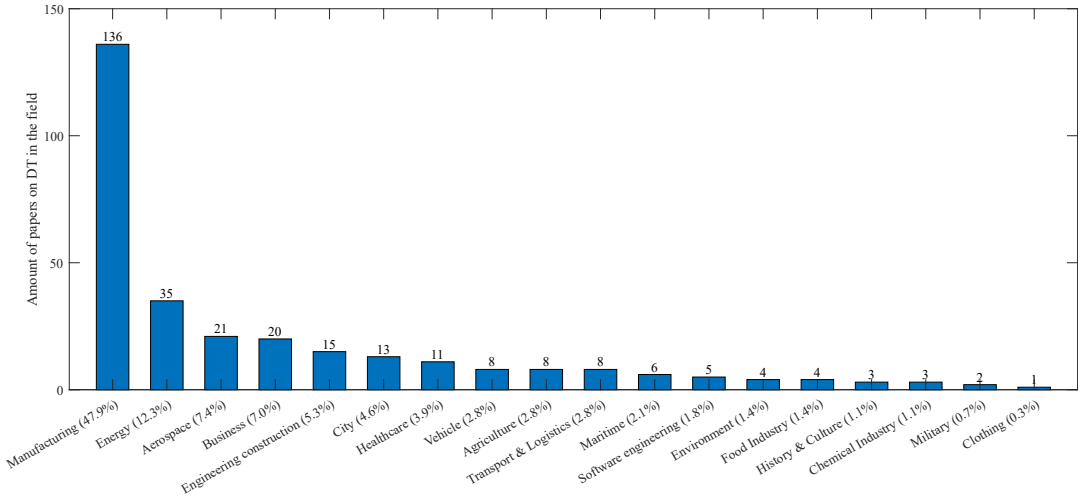

Figure 2.5: Functional distribution conveyed within papers on Digital Twin Anno 2022, using the data of [39].

The research gap within the energy industry concerning DTs is huge but rapidly filling. Electrolysis and DC/DC conversion are uncommon as only three electrolyzer DTs exist. DTs for DC/DC conversion are mainly focused on condition monitoring. This study can add more insights on the subject of DT as the focus lies on the electrical behavior and control of the combination of DC/DC converter and electrolysis.

2.4. Conclusion

As the energy transition accelerates, the demand for hydrogen production and use rises. Road maps have been made locally and globally to achieve hydrogen use in daily life. The Dutch government pushes for innovations to be investigated and piloted before 2030 in order to make the decision on what technologies to use to reach the climate goals.

Electrolyzer technologies such as AEC, PEMEC, and SOEC have their unique strengths and can have a preference over the other depending on the application. There's very little information lacking on electrolyzers benefits and downsides and a choice for the type of electrolyzer can be made. Models of each of the three types do exist but are mainly chemical models. The choices in electrical models are limited.

The literature has compared multiple DC/DC converters for electrolysis and MVDC grid use, but mainly separately. Many different types of converters have been presented but all converters come down to be a variant of either a DAB, FB, HB, PP or a Buck converter. All of these types of converters have been regularly modeled and studied in various applications. For the specific use case presented in this thesis, a new comparison is required. The literature found can be used to justify the selection process.

The DT is a relatively young concept with many opportunities to do research. Knowledge of DT in the energy industry is incredibly limited. Both electrolysis and DC/DC converters appear very little in DT literature and when they do, the focus is not on the electrical and control aspect. This thesis' biggest contribution to the literature will be by providing insight into the electrical behavior and control of a DC/DC converter for electrolysis as a DT.

Key conclusions from the literature review:

- The current context of hydrogen in the world encourages research in innovations of hydrogen technology and its applications.
- AEC, PEMEC, and SOEC are the three options found in the literature to implement for the system design. Enough is covered in the literature to justify a choice.
- DAB, FB, HB, PP, and Buck converters are possible for the DC/DC converter design. The preference of the type changes depending on the specifications of the input and output components. To select a converter, additional research is required.
- Only very little research exists on electrolysis and DC/DC conversion as a DT. The combination of them as a DT does not exist yet.

3

System Design

For the simulations in OPAL-RT and in Simulink the system depicted in Figure 3.1 is used. The system consists of a voltage source that depicts the MVDC grid, a DAB, an AEC model, control logic, and SPS modulation. The voltage source is connected to the input side of the DAB. The electrolyzer is connected to the output side of the DAB. Between the connections of the electrolyzer and the DAB, current measurements are taken to use for the control logic. The control logic drives the phase of the SPS modulation. The SPS modulation drives the gate signals used in the DAB. A summary of key values assigned to the main components is found in Table 3.1

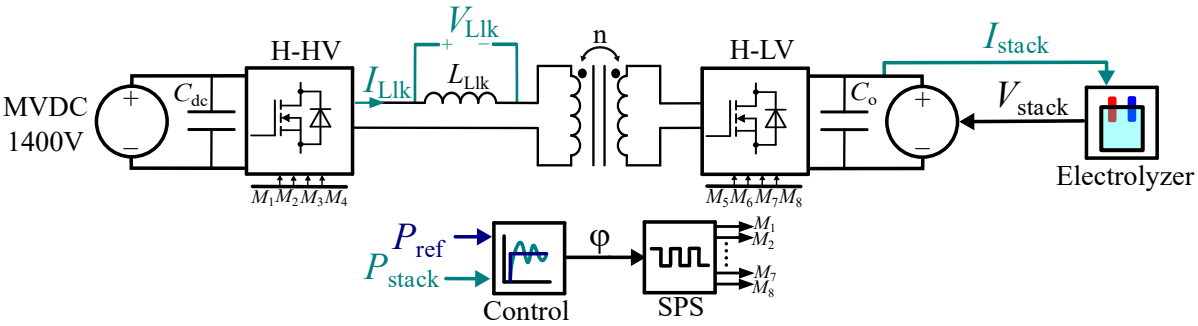

Figure 3.1: System design overview.

Table 3.1: Overview of system key values

Parameter name	Parameter symbol	Value
Switching frequency	f_{sw}	20 kHz
Rated power	P_{rated}	10 kW
Transformer turns ratio	n	0.05
Leakage inductance	L_{Llk}	586 μH
Phase at rated power	ϕ_{rated}	25 °

The implementation and the choices for the individual elements of the system will be discussed in the following sections. The choice of the electrolyzer and the implementation of the electrolyzer model are explained in Section 3.1. The comparison of multiple DC/DC converters and the implementation of the chosen converter are explained in Section 3.2. Lastly, the control logic and SPS modulation strategies used are covered in Section 3.3.

3.1. Electrolysis

3.1.1. Electrolyzer choice

As shown in Section 2.4, the literature found provides sufficient information to make a choice of the electrolyzer. Using Figure 2.1, Tables 2.1 and 2.2, and the literature [3, 15–20], a comparison is made which is depicted in Figure 3.2 via a spider plot. The meaning of the scores is given in Table 3.2. A high score is always positive for a design and a low score always has a negative impact.

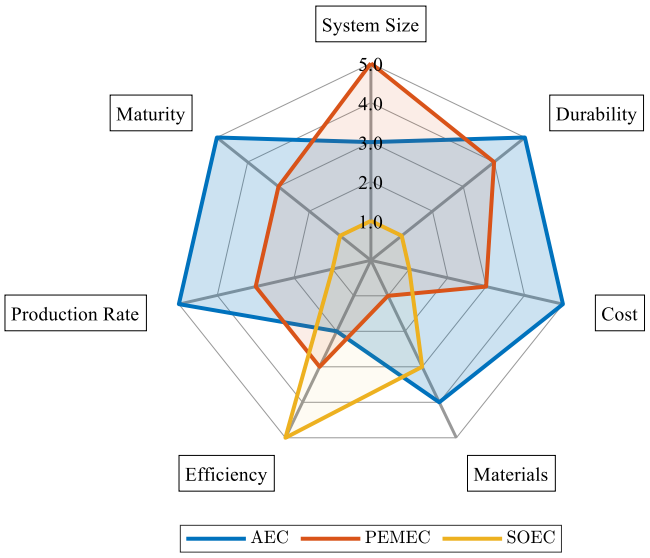

Figure 3.2: Spider Plot for the three types of electrolyzers using the findings of Section 2.4, Figure 2.1, Tables 2.1 and 2.2, and the literature [3, 15–20].

Table 3.2: Meaning of score per category for Figure 3.2

Category	**1**	**5**
System Size	Large	Small
Durability	Low	High
Cost	Expensive	Cheap
Materials	Scarce / Corrosive	Available / Sustainable
Efficiency	Low	High
Production Rate	Low	High
Maturity	Research phase	Fully developed

Whilst AEC has the lowest efficiency and purity, it is the most well-established technology. AEC are cost-effective and have been designed for high hydrogen production rates. This gives it an edge over the other more efficient, but underdeveloped technologies. On top of that, PEMEC uses scarce materials and SOEC is relatively large and expensive compared to the others. The decisive factors were chosen to be maturity, cost-effectiveness, and durability. This is to ensure that models exist and a real-life implementation remains feasible. As AEC scores the highest in these three categories, it was chosen to model an AEC.

3.1.2. Alkaline electrolyzer modeling approach

Several authors have created models of AEC. They mainly fall into the categories of thermal models, electrochemical models, mass transfer models, and fluïdic models [40]. As the DC/DC converter is the main component to be analyzed, the main interest lies in the electrical behavior of the AEC. The AEC model in [41] has been widely used for evaluating electrolyzer behavior in combination with additional electrical components [42]. Therefore, this study applies the model of [41] in the system design.

The AEC modeling used in this research is divided into two parts, The electrical side, and the chemical side. The electrical representation of an AEC is depicted in Figure 3.3. Here the anode and cathode of the AEC are presented as current sources with capacitances. The initial resistance of the AEC is indicated with R_{int}. The voltage source represents the reversible voltage coming from the electrolyzer. In order to utilize this within the full system design. The electrical model is simplified to a current-controlled voltage source and a lookup table according to the methods in [43]. The lookup table uses the stack current and the cell temperature to calculate the stack voltage. The lookup table is depicted in Figure 3.4.

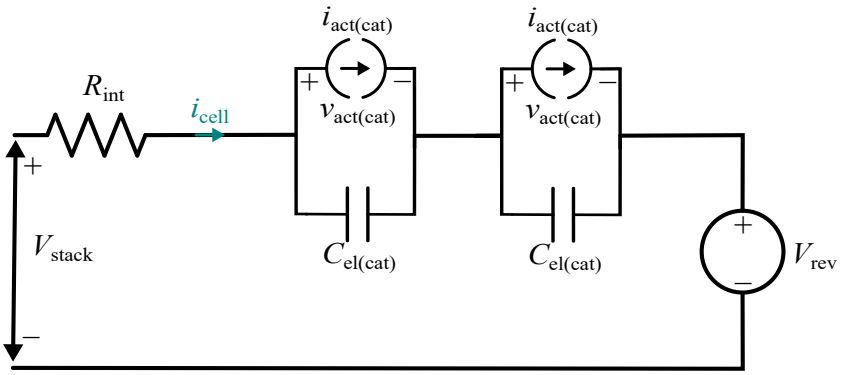

Figure 3.3: Electrical representation of an AEC [44].

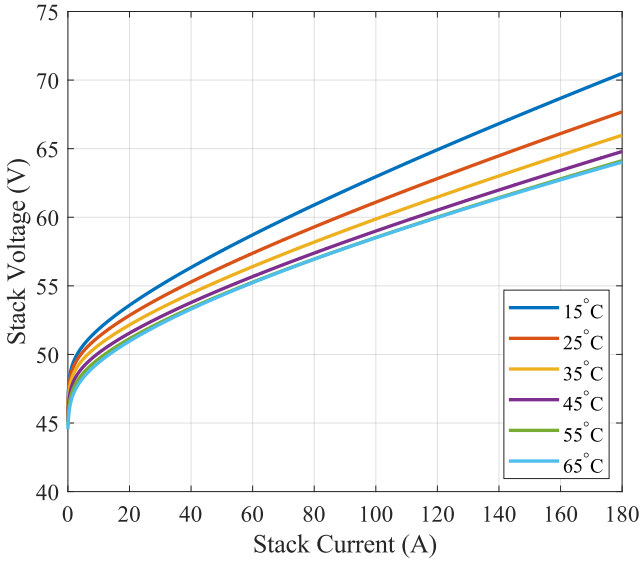

Figure 3.4: Look up table (graphical representation) used to set the current controlled voltage source to the according voltage, depending on temperature and stack current.

As depicted in Figure 3.4, the stack voltage V_{stack} is expressed as:

$$V_{\text{stack}} = N_{\text{s}} \cdot (V_{\text{rev}} + v_{\text{act(ano)}} + v_{\text{act(cat)}} + v_{\text{int}}) \tag{3.1}$$

where V_{rev} is the reversible cell voltage, N_{s} is the number of series connected cells, v_{int} is the ohmic potential, $v_{\text{act(ano)}}$ is the anode activation potential, and $v_{\text{act(cat)}}$ is the cathode activation potential. The expressions for V_{rev}, v_{int}, $v_{\text{act(ano)}}$, and $v_{\text{act(cat)}}$ are given in (3.2)-(3.5), respectively.

$$V_{\text{rev}} = V^0_{\text{rev,T}} + \frac{RT_{\text{k}}}{zF} \ln\left(\frac{(P_{\text{abs}} - P_{\text{KOH}})^{1.5}}{a_{\text{H}_2\text{O,KOH}}}\right) \tag{3.2}$$

$$v_{\text{act(ano)}} = s \ln\left(\frac{i_{\text{act(ano)}}}{t} + 1\right) \tag{3.3}$$

$$v_{\text{act(cat)}} = v \ln\left(\frac{i_{\text{act(cat)}}}{w} + 1\right) \tag{3.4}$$

$$v_{\text{int}} = i_{\text{cell}} \cdot R_{\text{int}} = i_{\text{cell}} \frac{r}{A_{\text{elect}}} \tag{3.5}$$

where $V^0_{\text{rev,T}}$ is the temperature-dependent reversible voltage with temperature in Celsius. R is the universal gas constant ($\text{JK}^{-1}\text{mol}^{-1}$). T_{k} is the cell temperature (K). P_{abs} is the absolute pressure (bar), z is the number of moles of electrons transferred for 1 mol of product, F is the Faraday constant (C mol^{-1}), P_{KOH} is the vapor pressure of KOH (bar), and $a_{\text{H}_2\text{O,KOH}}$ is the water activity of KOH solution. Besides that, the temperature-dependent constants are denoted as s, t, v, and w. Activation currents for the anode and cathode are represented as $i_{\text{act(ano)}}$ and $i_{\text{act(cat)}}$, respectively. r is the area-specific resistance of one of the electrolysis cells (Ωm^2). i_{cell} is the cell current. Finally, A_{elect} and R_{int} are the electrode surface area (m^2) and internal resistance of the electrolyzer cell (Ω), respectively [44].

Using the lookup table in Figure 3.4, the electrical circuit of Figure 3.3 can be simplified to a current-controlled voltage source and the data from the lookup table. This simplification is used in the end product as depicted in Figure 3.1. Here, the output of the DAB is connected to the current-controlled voltage source. The current after the output capacitor is measured and used as an input for the look-up table. For the use within this thesis, the temperature is assumed to be constant at 15 °C.

When the current reaches values of zero or below, the look-up table does not apply anymore. This can happen at any given moment, for instance at the start of running the model or whenever a constant ϕ of zero is introduced. To make sure that model can work, the methods of [41] are used to calculate the stack voltage. The current measurement I_{stack} is linked to a switch where whenever a stack current higher than zero is passing ($I_{\text{stack}} > 0$), the lookup table is used and whenever the current is zero or lower ($I_{\text{stack}} \leq 0$) the calculations of [41] are used with the values given in Table 3.3. The calculations used are given in equations (3.6) to (3.11). The switching process between the two methods for the calculation of V_{stack} is depicted in Figure 3.5.

$$a = -0.0151M - 1.6788 \times 10^{-3}M^2 + 2.2588 \times 10^{-5}M^3 \tag{3.6}$$

$$b = 1 - 1.2062 \times 10^{-3}M + 5.6024 \times 10^{-4}M^2 - 7.8228 \times 10^{-6}M^3 \tag{3.7}$$

$$P_{\text{H2O}} = \exp\left(81.6179 - \frac{7699.8}{T_{\text{k}} + 273.15} - 10.9 \ln\left(T_{\text{k}} + 273.15\right) + 9.589 \times 10^{-3}\left(T_{\text{k}} + 273.15\right)\right) \tag{3.8}$$

$$P_{\text{KOH}} = \exp(2.302a + b \ln P_{\text{H2O}}) \tag{3.9}$$

$$V^0_{\text{rev,T}} = 1.5184 - a_{\text{rev}}(1)\left(T_{\text{k}} + 273.15\right) + a_{\text{rev}}(2)\left(T_{\text{k}} + 273.15\right)\ln\left(T_{\text{k}} + 273.15\right) + a_{\text{rev}}(3)\left(T_{\text{k}} + 273.15\right)^2 \tag{3.10}$$

$$a_{\text{H}_2\text{O,KOH}} = \exp\left(-51.92 \times 10^{-3}M + 3.302 \times 10^{-3}M^2 + \frac{3.3177M - 2.131M^2}{T_{\text{k}} + 273.15}\right) \tag{3.11}$$

Table 3.3: Electrolyzer chemical equation values

Parameter	Value
M	7.64 mol/kg
N_{s}	36
a_{rev}	[1.5421×10^{-3}, 9.526×10^{-5}, 9.84×10^{-8}] V/K
P_{abs}	5 bar

where a and b are vapor constants (-), P_{H2O} is the vapor pressure of the water present in the electrolyte (bar), M is the molar mass of KOH (g/mol), N_{s} is the number of cells in series to form one stack (-), a_{rev} are the temperature related constants for determining the cell voltage (V/K).

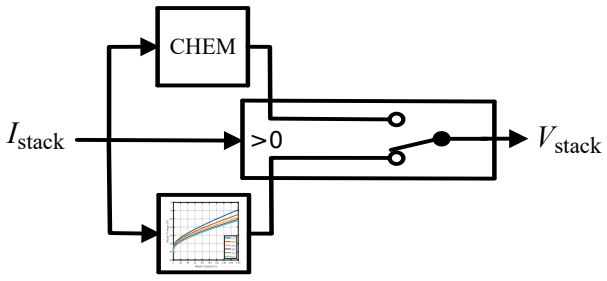

Figure 3.5: Switching process of the Lookup table and the methods of [41].

3.2. DC/DC converter

3.2.1. DC/DC converter choice

When scaled up to an industrial level, the design of DC/DC converters for electrolysis starts to become more complex. Electrolysis requires low voltage and extremely high current for its optimal operation which makes the operating environment of the converter components very tense. On top of that, obligatory design requirements include the presence of galvanic isolation between the input stage and the output stage per ISO22734:2020 and ISO:19880-1:2020 standards [45]. This means that from the gathered converter designs explained in Subsection 2.2.2, four options remain: DAB, FB, HB, and PP. The general schematics of these four converters are depicted in Figure 3.6.

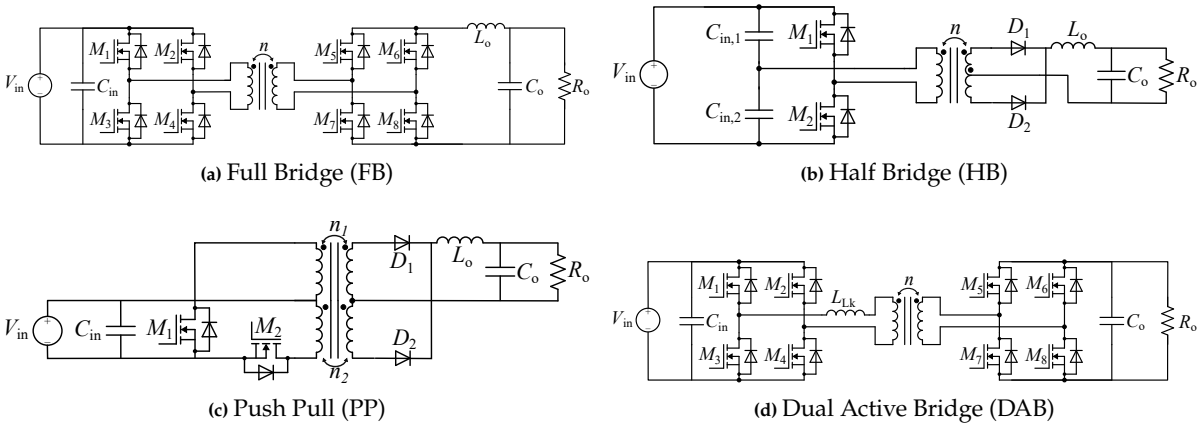

(a) Full Bridge (FB)

(b) Half Bridge (HB)

(c) Push Pull (PP)

(d) Dual Active Bridge (DAB)

Figure 3.6: The four isolated DC/DC converter topology candidates.

The four topologies have been modeled in Simulink to test their capabilities for a resistive load of 10 kW, a constant input voltage of 1400 V, and a constant output voltage of 70 V. All were tested for a system frequency of 20 kHz with the gates of the switches being driven by the most basic modulation variant of each converter. The voltage and current stresses were measured at each of the components of the converters. Ideal transformers were used to simplify the creation process. Diodes were modeled with 0.7 V voltage drop and 1 mΩ on-and-off resistance. Inductor and capacitor values were fitted accordingly to power and step-down requirements and to achieve a voltage ripple of 1% and a current ripple with a maximum of 20%. Key component characteristics found from the models of the topologies are presented 3.4.

Table 3.4: Component characteristics for the four isolated DC/DC converter topologies

Characteristic	**FB**	**HB**	**DAB**	**PP**
Number of transformer input and outputs	2	3	2	4
Transformer turns ratio	0.05	0.1	0.05	0.1
Transformer input voltage (p.u.)	1	1	1	1
Transformer input current (p.u.)	2	2	1	0.9
HV Switch voltage (p.u.)	1	1	1	2
HV Switch current (p.u.)	1	2	1	1
LV Diode/Switch voltage (p.u.)	1	2	1	2
LV Diode/Switch current (p.u.)	2	1	1	1
Output capacitance (p.u.)	2	1	3	2

Using Table 3.4 and the literature [21–23, 27, 45], advantages and disadvantages for each of the topologies are found and given in Table 3.5.

Table 3.5: Summarized isolated DC/DC converter comparison.

	FB	**HB**
Advantages	Reported for high power use (>3kW) Low switch stresses Low voltage stresses	Straightforward control Low output capacitance Transformer turns ratio
Disadvantages	High transformer primary current Complex control High current over diodes	Reported for low power use (<3 kW) High transformer current High switch and diode stresses
	DAB	**PP**
Advantages	Reported for high power use (>3 kW) Low component stresses Series-parallel and bidirectional arrangements	Straightforward control Low primary side transformer current Transformer turns ratio
Disadvantages	Very complex control large output capacitance necessary Quick saturation of transformer core	Reported for low power use (<3 kW) Voltage stress of primary switches is $2V_{\text{in}}$ Multiple transformers required

The FB's strong points are its combination of high power uses and manageable control complexity. The FB is less complex than DAB as only four switches need to be controlled, but is more complex than the HB and PP control. The FB has an upper hand on the PP and HB converters as less copper is required and more silicon for the same performance at high-power applications [21].

The HB has been reported and advised for power lower than 3 kW [22]. Since 10 kW is required, the normally strong points for system size vanishes as components grow out of proportion with the higher required power. On top of that, precise current control at high power is complex for HB converters [27].

The PP shows similar results as HB when compared to the FB and DAB in this application. The component composition of PP is alike HB, reported and advised for power uses lower than 3 kW [22]. The switches of the PP are exposed to a voltage of two times the input voltage. This leads to larger-sized switches than the others.

The DAB shows the least amount of current and voltage stresses on the reported components. The DAB is a very flexible topology with reported options for resonant converters, multi-level uses, series-parallel arrangements, and bidirectional capabilities [45, 46]. With the bidirectional capability, the complete P2PH network can be simplified, as depicted in Figure 3.7.

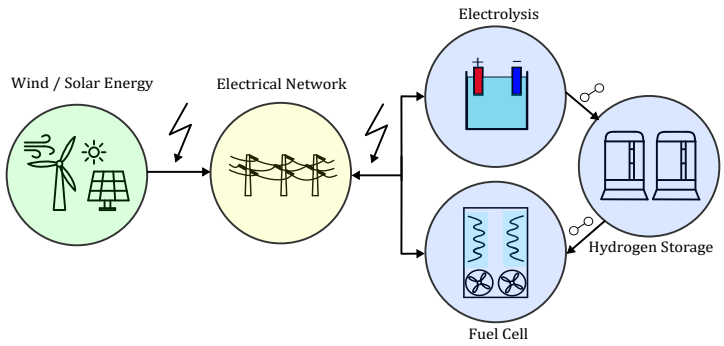

Figure 3.7: A general schematic of a bidirectional P2PH network.

The combined findings of Tables 3.4 and 3.5, Section 2.2.2 and the literature [21–23, 27, 45], have been summarized into a spider plot which is depicted in Figure 3.8. The meaning of the scores is given in Table 3.6. A high score is always positive for a design and a low score always has a negative impact.

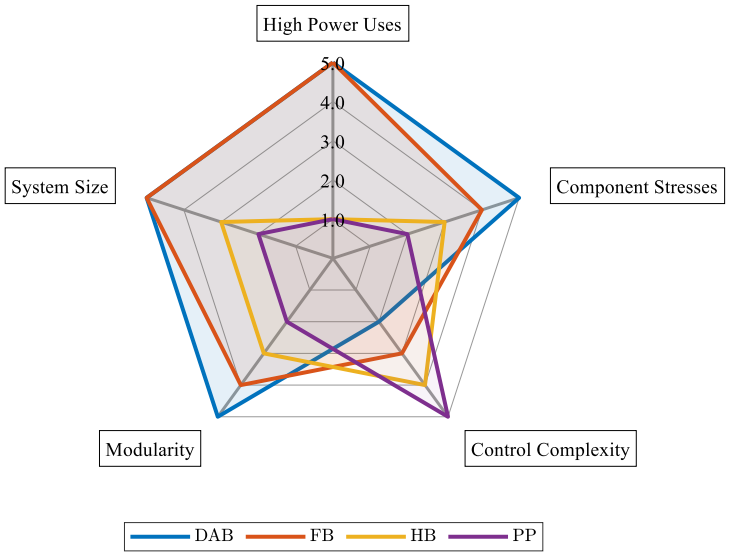

Figure 3.8: Spider Plot for the four types of DC/DC converters filled in using Tables 3.5 and 3.4, Section 2.2.2 and the literature [21–23, 27].

Table 3.6: Meaning of score per category for Figure 3.8

Category	**1**	**5**
High Power Uses	No uses reported	Many uses reported
Component Stresses	Low voltage and current stresses	High voltage and current stresses
Control Complexity	straightforward modulation and control	complex modulation and control
Modularity	No options modify topology	Many options to modify topology
System size	Large	Small

The DAB and FB are both viable choices when comparing them for the use case with a resistor load. This is due to that one offers less control complexity whereas the other allows for more creative ways to control for extremely high efficiencies. For static resistor load use cases, the FB is a better option due to its less complex modulation, however, an electrolyzer does not behave like a static resistor at all times.

The key decisive factors for choosing the DAB over FB, HB, and PP for the MVDC-electrolysis application are the DAB's modularity and component stress levels as reported in Table 3.4. The DAB is a future-proof design as it can be adjusted in both topology and arrangement sense to comply with all components of the P2PH network and to reduce component stresses even further. The DAB's modulation and control are complex yet allow for a robust design.

3.2.2. Dual Active Bridge modeling approach

The DAB is modeled with the following components; eight MOSFETs, an ideal transformer, a leakage inductor (with resistance), and both input and output capacitors (with resistance). These components, along with the measurement points used, are depicted in Figure 3.9. The values used for the DAB modeling are summarized in Table 3.7. The calculations and choices of each parameter are explained below.

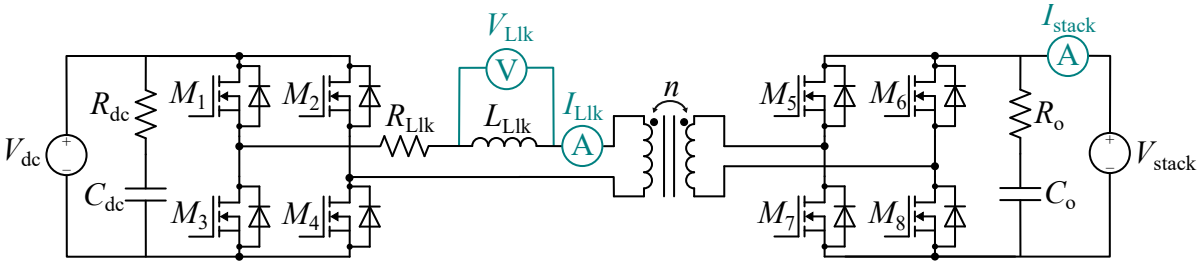

Figure 3.9: Dual Active Bridge modeling components and measurement points.

Parameter name	Parameter symbol	Value
Transformer turns ratio	n	0.05
Rated power	P_{rated}	10kW
Leakage inductance	L_{Llk}	586μH
Leakage inductor resistance	R_{Llk}	1mΩ
MVDC grid voltage	V_{dc}	1400V
DAB input capacitance	C_{dc}	1μF
DAB output capacitance	C_o	2mF
DAB input and output resistance	R_{dc}, R_o	1$\mu\Omega$

Table 3.7: Values used for DAB design

The values for the parameters n and L_{Llk} are calculated via equations (3.12) to (3.14) using the parameters of Table 3.7.

$$n = V_{stack}/V_{dc} \tag{3.12}$$

$$d = \frac{\phi}{180} \tag{3.13}$$

$$L_{Llk} = \frac{V_{dc} V_{stack} d(1-d)}{2nP_{rated} f_{sw}} \tag{3.14}$$

Where d is the normalized phase between the high-voltage side switches and the low-voltage side switches (-) and ϕ is the phase angle in degrees. V_{stack} is the output voltage of the electrolyzer, which for calculation purposes was left to be 70 V. In order to complete the calculation in 3.13 a value for ϕ of 25° was chosen.

The MOSFETs were chosen to be modeled with near-ideal behavior. This led to arbitrary low on-and-off resistance values, high values for the snubber capacitance and resistances, and zero forward voltage drop for all eight MOSFETs. The input capacitor was chosen to keep small as the MVDC network is presented as a voltage source.

The capacitors on both the input and the output of the converter are assumed to be ideal capacitors with very low resistance. The transformer is modeled to not saturate during operation, thus having high magnetization inductance and resistance.

3.3. Modulation & Control

3.3.1. SPS modulation

The gates of the field effect transistors (FETs) of the DAB are driven using SPS Modulation. The advantages of this method are that the modulation is relatively very simple compared to other options such as Extended Phase Shift (EPS) and Triple Phase Shift (TPS). On top of that, SPS is only driven by two parameters. Which simplifies the control of the output voltage and current. This way, the combination of modulation and control can be kept simple to implement and check [47].

SPS modulation is acquired by creating pulse signals for the eight switches according to the pattern depicted in Figure 3.10, where M_{1-4} stand for the switches on the high voltage (HV) side, M_{5-8} stand for the switches on the low voltage (LV) side, V_p represents the voltage behavior on HV side transformer, V_s represents the voltage behavior on the LV side transformer, I_{Lk} represents the current of the leakage inductor, T_a is the time at which gate is set to 'on', DT_{sw} is the fraction of activation time with which the signals of M_{5-8} are delayed (phase shifted). For reference, DT_{sw} is depicted in Figure 3.10 as the time between t0 and t1.

For this modulation, the following has been taken into account. Firstly, the dead time of the switches will be kept (near) zero in order to reduce complexity. Secondly, the gate signals themselves are made in different ways for each type of simulation, these will be discussed in their respective chapters. Lastly, the duty cycle of the gate signals is chosen to be kept at 50% during the process. This way only the parameter DT_{sw} will be controlled via the control logic.

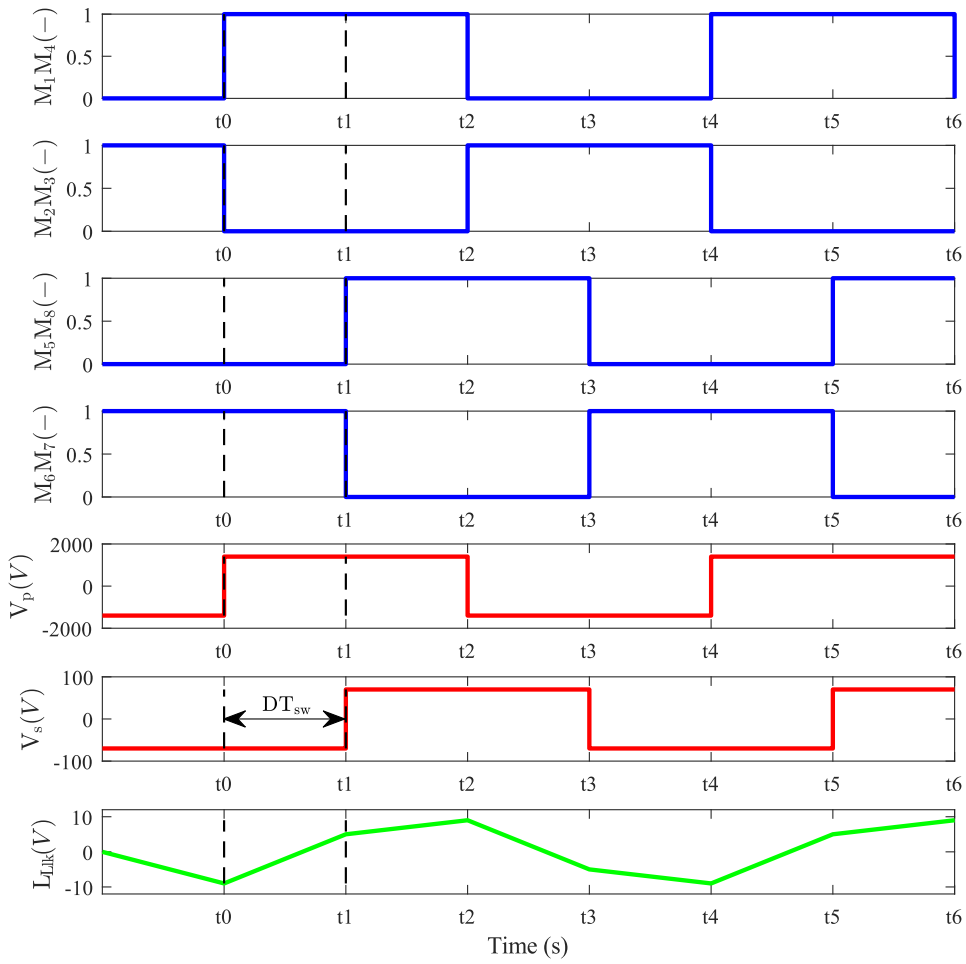

Figure 3.10: SPS Modulation for DAB.

3.3.2. Control approach

The control logic is mainly made out of measurements, signal processing and a PI controller. The full control logic is depicted in Figure 3.11 The inputs of the control logic are the output power of the dual active bridge P_{stack} and the reference power signal P_{ref}. The output power is obtained by measuring the output current and the output voltage and multiplying them. Subtracting these two signals gives the error signal P_{diff} which is the input of a PI controller. The PI controller is designed in "ideal mode". This means that the PI controller is tuned with according to 3.15

$$\phi_{\text{PI}} = K_{\text{p}}(P_{\text{diff}} + K_{\text{i}} \int P_{\text{diff}}) \tag{3.15}$$

Where ϕ_{PI} is the output of the PI controller in degrees, K_{p} & K_{i} are the tuned proportional and integral gains respectively and P_{diff} is the input of the PI controller.

The proportional and integral gains K_{p} and K_{i} are tuned using trial and error for each type of simulation. Lastly, the output PI signal is limited using saturation. The upper and lower bound limits of the saturation are the allowed phase range of the DC/DC converter b_{sat}. All the used settings for both the control logic and the SPS modulation have been summarized in Table 3.8.

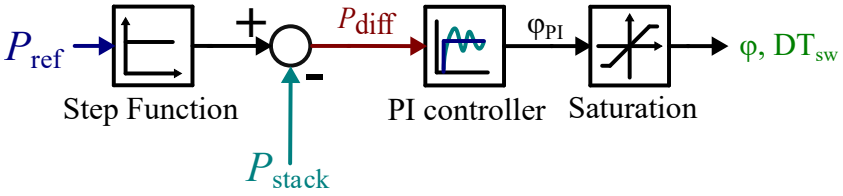

Figure 3.11: Control logic subsystem overview.

Table 3.8: Control logic and SPS modulation design parameter overview

Design parameter	Value
K_{p}, K_{i}	Dependent on simulation model
b_{sat}	$[0, 45]^{\circ}$
D	50%
ϕ_{rated}	25°

In Table 3.8, K_{p} is the proportional gain value of the PI controller, K_{i} is the integral gain of the PI controller, b_{sat} is the bounds of the saturator, D is the duty cycle of the gate signals and ϕ_{rated} is the phase at which the rated power occurs in the system.

4

Simulation Modeling

This chapter covers the Simulation models made for the design discussed in Chapter 3. There are two versions of this model. One is implemented with purely Simulink blocks and the other is implemented using PLECS for the electrical elements.

In Section 4.1, the modeling approach within Simulink is discussed where all the connections and uses of the elements and subsystems are explained. In Section 4.2, the modeling approach for the use of PLECS is discussed along with the similarities and differences with the pure Simulink model. Detailed screenshots and source code of both models are included in Sections A.2 to A.3. The model output and results are discussed in Chapter 6.

4.1. Simulink modeling approach

The Simulink model has the most straightforward modeling of the system design. A top view of the model is included in Figure 4.1. The components are divided up into subsystems for single phase shift modulation (SPS), The control center (Control), the MVDC grid (represented by the 1400V voltage source), the DAB, and the electrolyzer (and the voltage source coupled to it) and a subsystem for monitoring (Scopes). The paragraphs following discuss the setting and modeling for each of the subsystems.

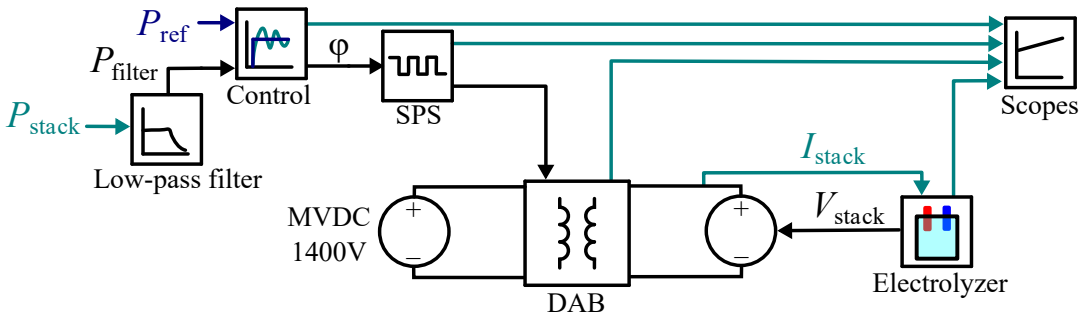

Figure 4.1: Simulink model overview.

4.1.1. SPS subsystem

The SPS subsystem includes the schematic depicted in Figure 4.2. Two sawtooth generators are used to generate a signal with switching frequency f_{sw}. One sawtooth is generated with a 180° phase shift in comparison to the other. Both of these signals then go through two "Matlab Function" blocks. Matlab Function block one (FCN1) holds equations (4.1) and (4.2) and Matlab Function block 2 (FCN2) holds equations (4.3) and (4.4) in order to apply the phase shift to the signals.

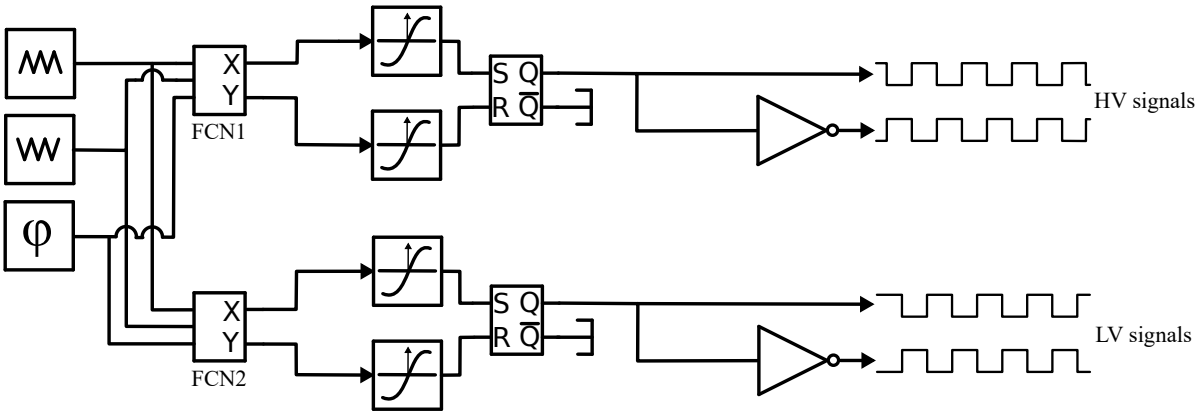

Figure 4.2: SPS modulator that can utilize dynamic phase shift for Simulink

$$X_{FCN1} = 0.5 * ((x + 1) - (1 - \phi/360)) \tag{4.1}$$

$$Y_{FCN1} = 0.5 * ((y + 1) - (1 - \phi/360)) \tag{4.2}$$

$$X_{FCN2} = 0.5 * ((x + 1) - (1 + \phi/360)) \tag{4.3}$$

$$Y_{FCN2} = 0.5 * ((y + 1) - (1 + \phi/360)) \tag{4.4}$$

where x is the incoming sawtooth signal without 180 ° phase shift, y is the incoming sawtooth signal with 180° phase shift (-). ϕ is the phase shift between the HV side and LV side of the DAB in degrees, X_{FCN1} is the signal output of the altered x sawtooth of the FCN1 block (-), Y_{FCN1} is the signal output of the altered y sawtooth of the FCN1 block (-), X_{FCN2} is the signal output of the altered x sawtooth of the FCN2 block (-), Y_{FCN2} is signal output of the altered y sawtooth of the FCN2 block (-).

The outputs X_{FCN1}, Y_{FCN1}, X_{FCN2}, Y_{FCN2} pass through rising edge hit crossing detection blocks. This results in four signals that peak at intervals in every $\frac{1}{f_{sw}}$ seconds. Using the SR-flipflops, the pairs X_{FCN1} & Y_{FCN1} and X_{FCN2} & Y_{FCN2} are merged into one pulse signal. The hit crossing output signals and the SR-flipflop output signals are depicted in Figure 4.3. The output of the SR-flipflops is used for switches M_1 & M_4 (HV side) and M_5 & M_8 (LV side) of the DAB. A NOT gate is used to create the signals for the opposing switch pairs M_2 & M_3 and M_6 & M_7.

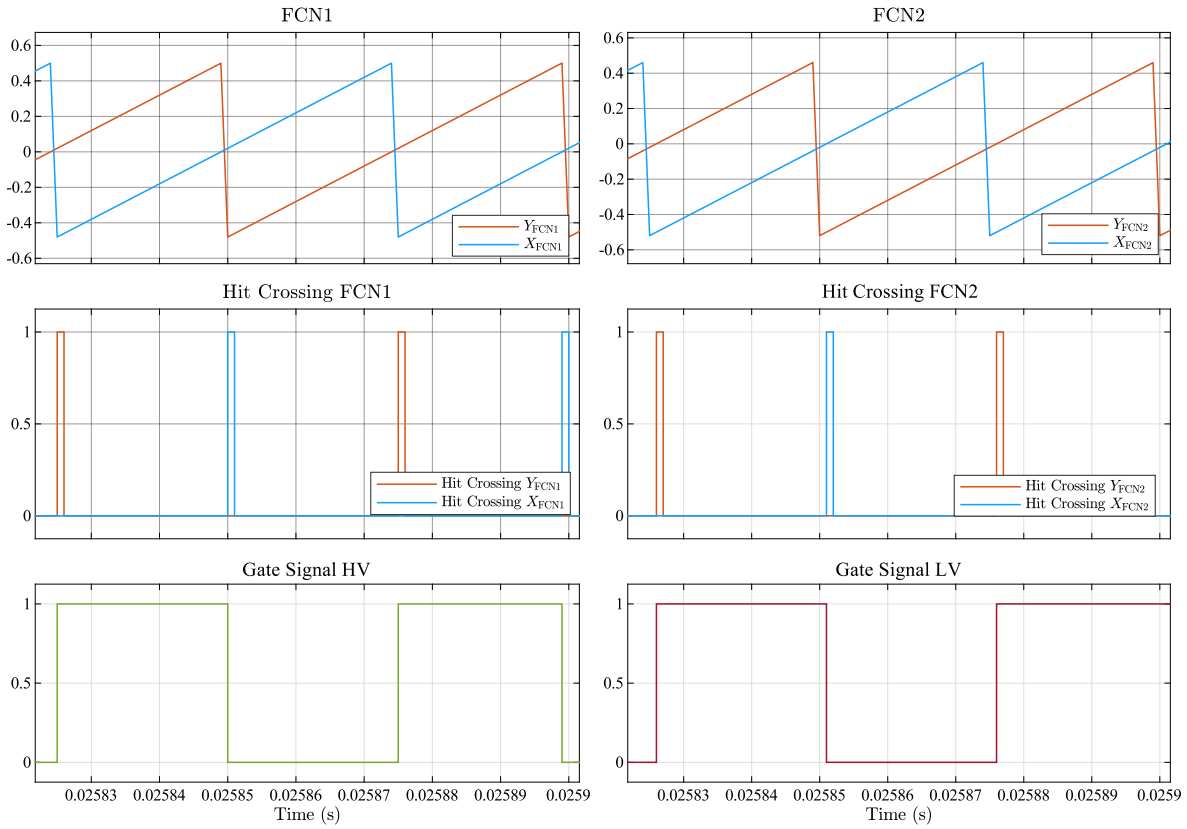

Figure 4.3: FCN function blocks outputs, hit Crossing detection outputs, and resulting gate signal from the SR-flipflops output at the HV side and LV side which create the phase-shifted pulse signals.

4.1.2. Electrical subsystem

The electrical components for the DAB, the MVDC grid, and the Electrolyzer are from the "Specialized Power Systems" pack of Simscape blocks for Simulink. From here the resistors, inductors, capacitors, voltage sources, MOSFETs, transformers, and meters were selected for the model. The electric components have values set according to Table 3.7 and are arranged as shown in Figure 3.9. The blockset requires a "Powergui" block. The blockset allows for easy integration between system signals and electrical signals. The gates of the MOSFETs can be driven using system signals and the electrical signals are easily put into system signals via measurement blocks.

4.1.3. Electrolyzer subsystem

The electrolyzer subsystem handles the determination of V_{stack} using I_{stack}. This susbsytem consists of two parts, The lookup table, and the switching system. These are coupled using the proposed switching mechanism of Figure 3.5. The lookup table of Figure 3.4 is made using the "1-D lookup table" block, and both (3.6) to (3.11) and Table 3.3 are implemented using "Matlab Function" blocks.

4.1.4. Control subsystem

The control subsystem is implemented as depicted in Figure 3.11. The PI controller is set to continuous or discrete mode to comply with the Powergui block. Additionally, due to the heavy oscillations in the P_{stack} signal received when running the model, a low pass filter block was added after the measurement of the P_{stack} signal. The low pass filter operates with a cutoff frequency of 500 Hz. This reduced the oscillation to a degree where PI control could converge.

4.1.5. Discretization

In order to have an accurate DT model, discretization is a must. This is due to the fact that these signals in real life are controlled via machines that sample the signals. The gate signals would be created using a digital machine and the measurements are not processed as continuously as the clocking speed of a controller would not keep up. In a continuous mode, the physical components would overflow with information. Discretization is crucial for the outcomes of the models as the control settings need to be different since the behavior of discrete devices is different.

The model settings for the discrete model are given in Table 4.1. The main settings to change for discrete mode are setting the PI controller and the Powergui blocks. These need to be set to discrete and according to sampling time. The step size is set to 1 μs to stay well below the switching time. The simulation is performed in normal mode.

Table 4.1: Simulation Parameters for discrete Simulink model

Parameter	**Discrete modeling setting**
Solver	ode4 (Runge-Kutta)
Solver type	Fixed step size
Step size	1 μs
Run mode	Normal
Powergui	Discrete
Sample time PI and Powergui	1 μs

4.1.6. PLECS proposition

During testing of the model, lots of noise was detected in the signals for the discrete Simulink model. As modifying the control and the DAB did not result in lowering the oscillations, another reason for them to exist was deduced. The Simulink blockset and solver combination can lead to simulation errors which are depicted as oscillations.

To test this hypothesis, an additional model was designed using PLECS. When using PLECS, the electrical and control environments have to be split. As this is also the case for the DT modeling, it is used as an in-between modeling step.

4.2. PLECS Modeling approach

For the PLECS model, only the electrical signals are moved towards the PLECS environment. The other aspects remain in the Simulink environment. The setup and division of the subsystems are depicted in Figure 4.4. In Appendix A.3 the code used for the PLECS model is given and in Appendix A.4 screenshots of the PLECS modeling are provided.

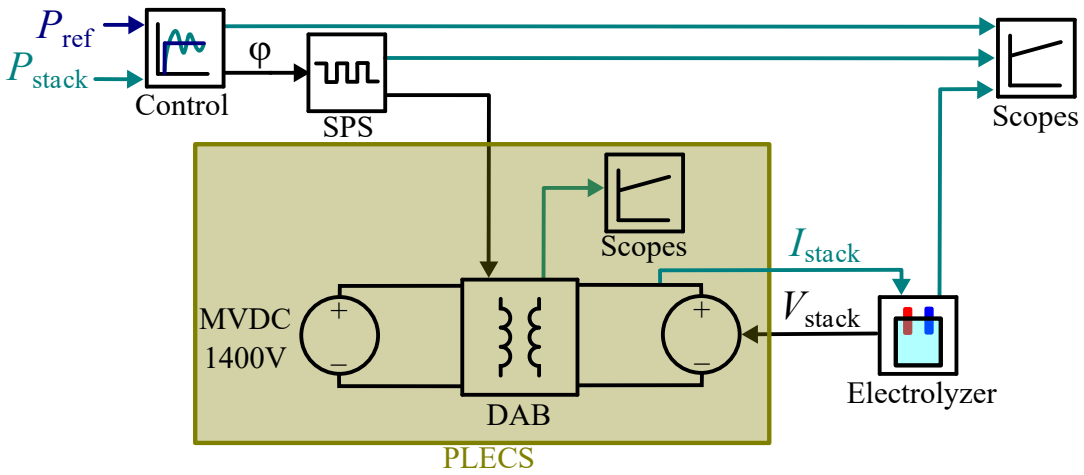

Figure 4.4: PLECS model overview.

Moving the electrical components to the PLECS environment has led to a few minor changes to the DAB design. The inside of the PLECS environment is depicted in Figure A.13. The diodes that are normally inside of the MOSFETs, are now modeled outside of the MOSFETs. Probes with gains were inserted instead of measurement blocks to improve the readability of the measured signals. All other aspects remained the same as the Simulink modeling.

All non-electrical parts of the Simulink modeling can be reused for the PLECS modeling. The working of the SPS subsystem is the same for the PLECS-based model as for the Simulink model. The only difference is that the output signals are now converted for PLECS environment use. The electrolyzer subsystem is split for the electrical signals and the calculations for V_{stack}. The value of I_{stack} is extracted from the PLECS environment and put into the electrolyzer subsystem, which returns a value for V_{stack} to the PLECS environment. Unlike the Simulink modeling, the P_{stack} signal does not need to be filtered for accurate control, thus the filter is removed from the control subsystem. The monitoring of the signals is divided into sections for electrical components and for non-electrical components. Where the leakage inductor, the electrolyzer, the transformer, and the MOSFETs are measured in the PLECS environment and the SPS signals, control signals, and (non-electric) electrolyzer signals are measured in the Simulink environment.

The simulation settings are now set for both Simulink and PLECS environments. These parameters have been summarized in Table 4.2. Ode4 (Runge-Kutta) is chosen once more with a fixed-step simulation for discrete modeling. The fixed step size for PLECS and Simulink needs to be matched, this was set to 0.1μs. To speed up the compilation and simulation time, the accelerator mode is used over the normal mode.

Table 4.2: Simulation parameters of PLECS based model

Parameter	Selected setting
Solver	ode4 (Runge-Kutta)
Solver Type	Fixed Step
Fixed Step Size / PLECS step size	0.1 μs
Simulink Run mode	Accelerator

5

Digital Twin Modeling

The modeling approach for the DT is discussed in this chapter. Screenshots and source code of the DT model are included in appendices A.5 and A.6. As a guide for future users of the models, Appendix B includes a guide on how to execute the DT model and what to take into account. A collection of the occurred errors during the simulation and building of the DT model, and their solutions, have been documented in Appendix C.

For the DT model, the hardware and software made by OPAL-RT are used. The OP4610XG model was used to simulate, which is depicted in Figure 5.1a. The hardware specifications of the OP4610XG are provided in Table 5.1. The complete setup with oscilloscope, computer, and OP4610XG is depicted in Figure 5.1b. The software Scopeview can also be used to look at analog and digital signals.

(a) OP4610XG

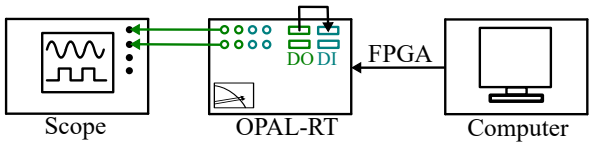

(b) OP4610XG in hardware setup

Figure 5.1: The OP4610XG and its hardware environment.

Table 5.1: OPAL RT hardware specification comparison

Category	OP4610XG specification
CPU Family	AMD Ryzen 5
CPU Specs	6 cores, 3.8 Ghz
FPGA (Xilinx)	Kintex - 7 410T
Number I/O modules with	4
Max number of I/O channels	140
Available software/toolboxes	ARTEMiS, eHSx64/32, ePHASORSIM Orchestra, RT-XSG, ScopeView

5.1. Digital Twin modeling approach

The Digital Twin model is made using the OPAL-RT software "RT-LAB". This software allows the configuration of the OPAL-RT hardware as well as model design using Simulink and additional toolboxes. The OPAL-RT software makes use of Simulink (and Matlab) version R2021b. In order to let the hardware calculate, one part of the model has to stay within the CPU of the computer (SC_GUI) and the other part is transferred to the OPAL-RT Hardware (SM_COMPUTE) using the FPGA. The communication layout between these two parts is depicted in Figure 5.2. The SC_GUI is used as an interface that allows monitoring and communication during simulation whilst SM_COMPUTE contains the calculations, electrical schematics, and non-changeable values. During simulation, the values in SC_GUI can be changed to influence the model [44].

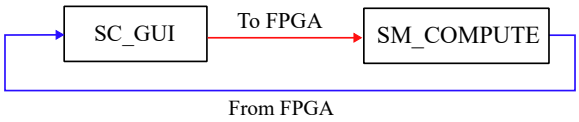

Figure 5.2: Top level DT layout for execution within the real-time simulator [44].

To apply the system design of Chapter 3 into the configuration of Figure 5.2, the components and values are split for redistribution over SC_GUI and SM_COMPUTE. SC_GUI contains scopes to keep track of the control and all the reference signals. SM_COMPUTE contains the largest portion of the system design. The PI control, the SPS modulation, the DAB, and the electrolyzer modeling are implemented in SM_COMPUTE. Figure 5.3 depicts the overview of the component division.

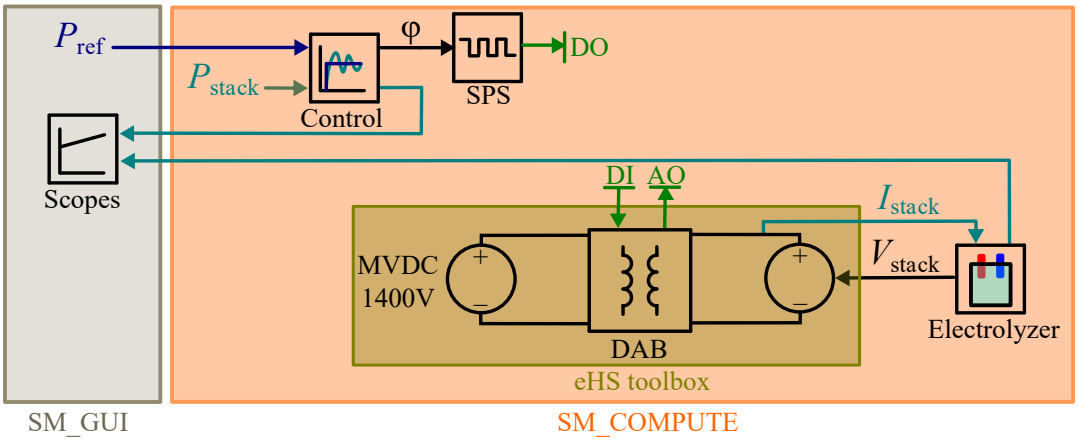

Figure 5.3: DT model overview, where subsystems are divided over SM_COMPUTE, SC_GUI, and the eHS toolbox. DI, DO, and AO are shown in green.

To link the signals between the SC_GUI and the SM_COMPUTE subsystems of the model, blocks of the RT-LAB toolbox are used. The "OPcomm" blocks are placed in both subsystems to facilitate communication. In SC_COMPUTE, the OPcomm block receives the reference signals with a sample time of 50μs. In SC_GUI, the "OPcomm" block is only required to know in what acquisition group the signals of SM_COMPUTE are put in. In this case, the acquisition group was 1. The OPcomm block in SC_GUI allows for dynamic signal acquisition, which in turn can be viewed in scopes. The data of the signals in SM_COMPUTE can also be acquired via the "OPwriteFile" block, which samples the data and puts it in a .mat file.

5.2. SPS subsystem

The SPS modulation subsystem is different for the OPAL-RT in comparison to the Simulink and PLECS models. The designed modulation for Simulink was only able to run for a maximum switching frequency of 1 kHz in the OPAL-RT environment. This limitation led to the use of the digital channels of the OP4610XG to generate the pulse signals. A switching frequency 20 kHz was chosen as higher frequencies showed inaccurate and misshaped output signals. Due to this limitation, the switching frequency of the models in Chapter 4 was also chosen to be 20 kHz for comparison purposes.

The SPS modulation is achieved by sending the pulse signals out through the Digital Out (DO) ports of the OPAL-RT systems and put into the DAB via the Digital In (DI) ports. To couple the DO and DI internally via the software, The SPS subsystem uses the "OPctrl" blocks. A "PWMout" block is made to generate the PWM signals. Only one instance is necessary as the block is capable of generating all signals. A "PWMin" block is used to receive the DI signals which then are routed to the eHS.

Due to the change in SPS signal creation method, normalized values between 0 and 1 are used to express phase. The domain of [0, 0.5⟩ , translates to the phase of [-180, 0⟩° whilst [0.5, 1] is used for [0, 180]°. The domain of [0.5, 1] is used as the SPS is used to shift the phase at the LV leg of the DAB.

As the SPS signals have moved from the Simulink domain to the electrical domain, the form of the signals is changed. The SPS signals for the OPAL-RT model have been depicted in Figure 5.4. The signals display slopes instead of instantaneous switchovers. This happens due to the signals being made with electrical signals, in which natural physics does not allow for instantaneous switchovers.

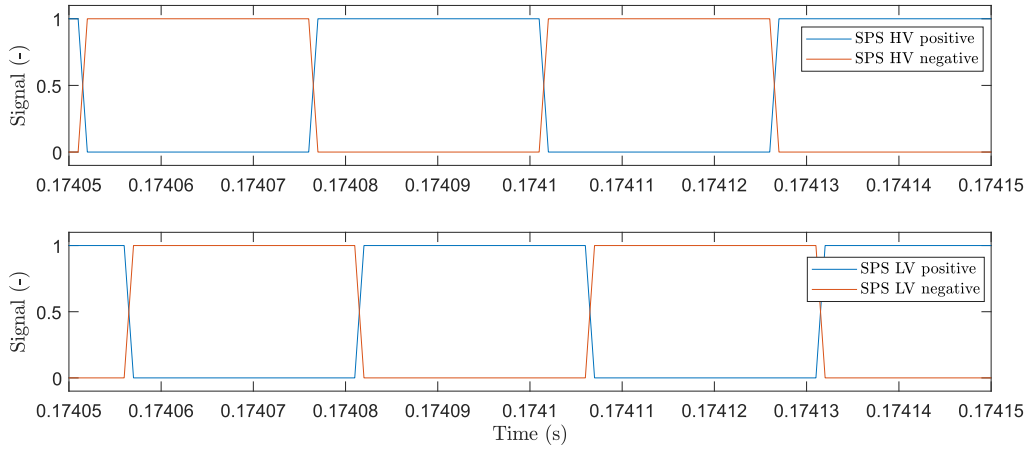

Figure 5.4: SPS signals for the OPAL-RT modeling.

5.3. eHS subsystem

The eHS Toolbox is used to simulate the electrical components. This toolbox helps to translate the behavior of the electrical components so that they can be sent through the FPGA. The eHS toolbox contains the voltage sources, capacitors, inductors, resistors, and electrical measurements of the system design.

Instead of MOSFETs, insulated-gate bipolar transistors (IGBTs) are used in the design. Double-arm IGBT blocks are used to simplify the design. The IGBTs are assumed to have ideal behavior and are modeled with ideal on-and-off resistances. The transformer is assumed to be ideal and does not saturate in the used power range and is modeled with near zero winding resistance and inductance.

The inputs of the eHS subsystem are the signals received at the DI port of the hardware and the voltage signal V_{stack}. The outputs of the system include the measured voltage and current signals over the leakage inductance and the output of the DAB. These four signals are sent to the Analog Out (AO) channels of the hardware to be read by an oscilloscope or Scopeview. A screenshot with the signal routing in the eHS toolbox environment is depicted in Figure 5.5. The AO signals are depicted in green and the DI signals in pink.

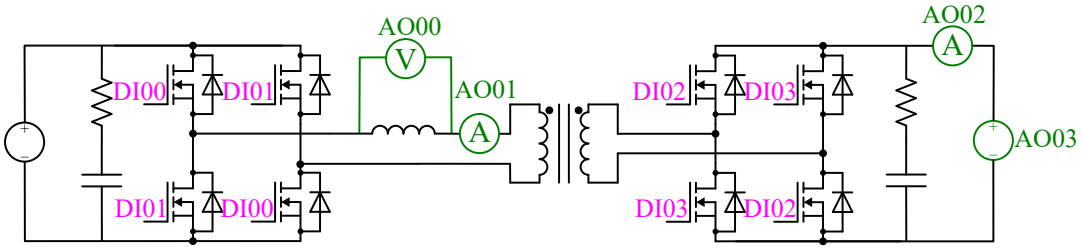

Figure 5.5: eHS modeling and signal routing.

5.4. Electrolyzer subsystem

The V_{stack} signal created by the electrolyzer subsystem is routed into the eHS toolbox to drive the voltage source at the output of the DAB. However, the eHS toolbox does not allow to initialize an output voltage. Therefore, the loop of current measurement and voltage setting cannot be started. The electrolyzer subsystem is modified to receive P_{ref}, instead of I_{stack}, as input to set the electrolyzer V_{stack}. A new lookup table was devised to accommodate for P_{ref} to V_{stack}. The P_{ref} to V_{stack} relation is depicted in Figure 5.6. The new lookup table is also implemented in the model using a "1-D table" block.

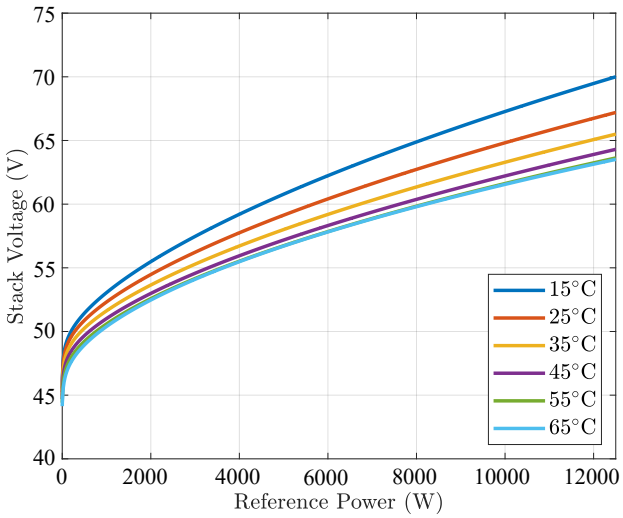

Figure 5.6: Look-up table (graphical representation) used to set the stack voltage depending on temperature and power reference signal.

The switching mechanism of the chemical model and the lookup table is now driven by P_{ref} instead of I_{stack}. As long as P_{ref} is greater than zero, the lookup table is used otherwise, (3.6) to (3.11) are used. The updated switching mechanism is depicted in Figure 5.7

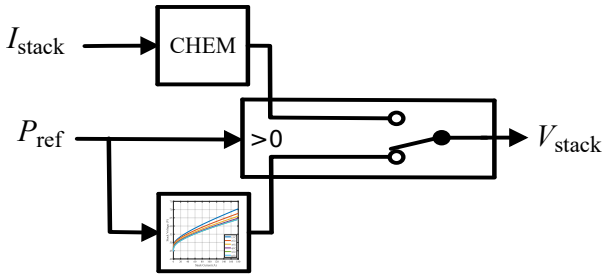

Figure 5.7: Switching process of the Lookup table and the methods for DT modeling.

5.5. Control subsystem

The control modeling has one big difference in comparison to the design of Section 3.3.2. Again, a PI controller is used with the P_{ref} and P_{stack} signals. However, the output is now controlled for a different domain than in Simulink. Therefore, the saturation bounds b_{sat} are changed accordingly to a lower bound of 0.5 and an upper bound of 0.625 representing the bounds of [0, 45]°. Additionally, buttons to set a phase value and to turn PI on and off were added.

6

Results

A literature study was performed in order to assess the component candidates for the system design, find information on the use of DT and exploit the research gap. AEC, PEMEC, and SOEC were found as candidates for the electrolyzer. DAB, FB, HB, PP, and Buck converters were found as candidates for the DC/DC converter.

The system was chosen to be designed with a DAB connected to an AEC and a voltage source representing an MVDC grid and PV generation whilst utilizing SPS modulation and PI control. An AEC was chosen as the literature showed that these are cost-effective, have high durability, and have matured in development. A DAB was chosen as isolation of the HV and LV sides is an ISO requirement, it can be used for high power with high efficiency, and it offers growth for larger networks with possibilities for series-parallel arrangements and bidirectional capabilities. The DAB is designed for a system frequency of 20 kHz and a rated power of 10 kW at a phase of 25°. The input voltage of the DAB is created with a 1400 V voltage source and the output of the DAB is rated for 70 V. SPS modulation and PI control were both chosen for their simplicity as the phase shift is the only variable to be controlled for. All models were made according to this system design and simulations were run.

To validate the working of the DAB in each model, the leakage inductor and the output voltage and current were measured. The current and voltage of the leakage inductor are measured at rated power. To test and tune the PI controller, a power reference sequence of 5 kW, followed by 8 kW, 6 kW, 9 kW, and 10 kW was made for an interval of 50 ms. Each power occurred for an interval of 0.01 seconds. In the first 5 ms, the PI control was turned off to initialize the DAB for a constant phase shift. The PI control values K_p and K_i were tuned using trial and error until the best perceived settling time was reached.

The Simulink modeling results are discussed in Section 6.1, the PLECS model results are discussed in Section 6.2 and the DT modeling results are discussed in Section 6.3. The results chapter is concluded with a performance comparison in Section 6.4, summarizing and rating the performance of each model.

6.1. Simulink model results

The system design was first implemented in Simulink models in order to test the design before moving to the DT environment. The Simulink model progressed in steps, which resulted in multiple variations of the model. The first Simulink model ran in continuous time, however, since RTDTs use discrete time, a switch was made to a discrete version of the same model (Subsection 4.1.5). The model output for the discrete model is discussed in this section.

The leakage inductor voltage and current for the discrete Simulink model are depicted in Figure 6.1. The behavior of the voltage curve is as expected as the signal is moving around zero as their baseline at the rate of the switching frequency and peaking at the expected values of 2800 V. However, the current signal is expected to stay below an absolute value of 10 A for the design. This indicates that the current signal is exposed to oscillations.

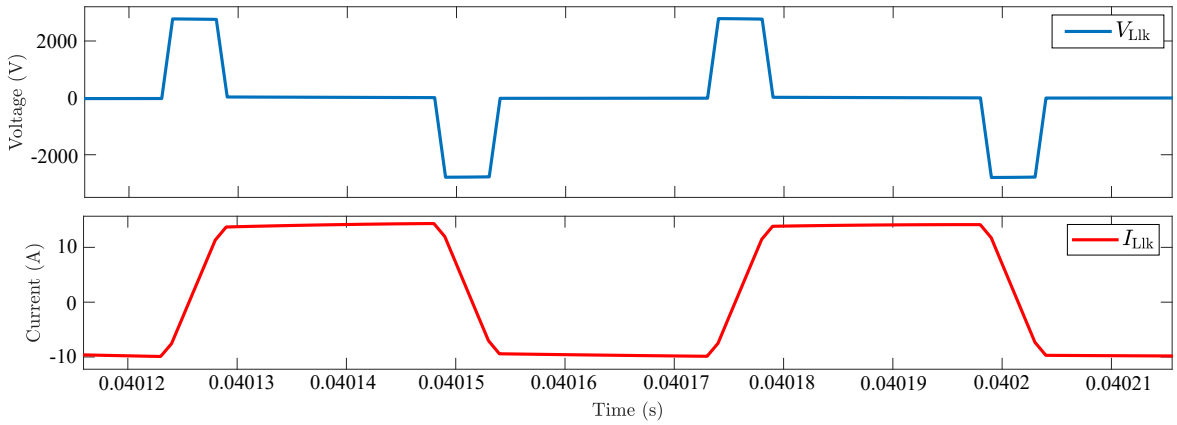

Figure 6.1: Leakage inductor voltage and current measurements for Simulink discrete model.

The output voltage and current for the discrete Simulink model are depicted in Figure 6.2. From Figure 6.2 can be seen that the oscillations are the strongest in the current signal, which are a direct consequence of the current oscillations in the leakage inductor.

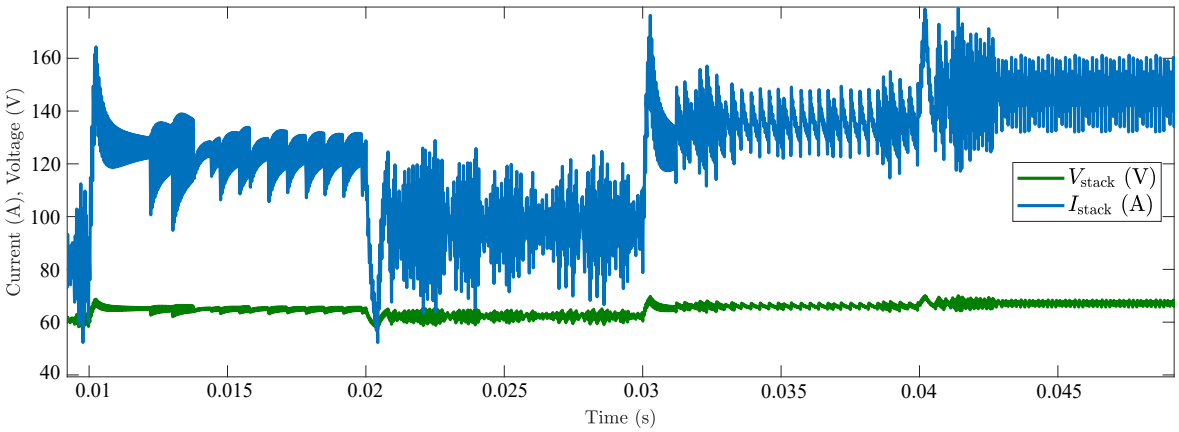

Figure 6.2: Stack voltage and current of the electrolyzer for Simulink discrete model.

The PI control response for phase, reference power, stack power, and filtered stack power for the discrete Simulink model is depicted in Figure 6.3. To converge the stack power signal to the reference power signal, filtering was necessary as oscillations occur. Without a filter, these PI signals do not converge. The control converged with the best settling time of 0.004 s using a K_p value of 0.006 and a K_i value of 2000. The settling time was measured using the filtered stack power signal.

The power oscillations that occur in the discrete model have a maximum amplitude of 2.5 kW in steady state. It was attempted to reduce oscillations by heavily increasing the output capacitance of the DAB (e.g. quadrupling and ten folding the capacitance value C_o). This resulted in a longer PI settling time and an oscillation reduction of less than 5%.

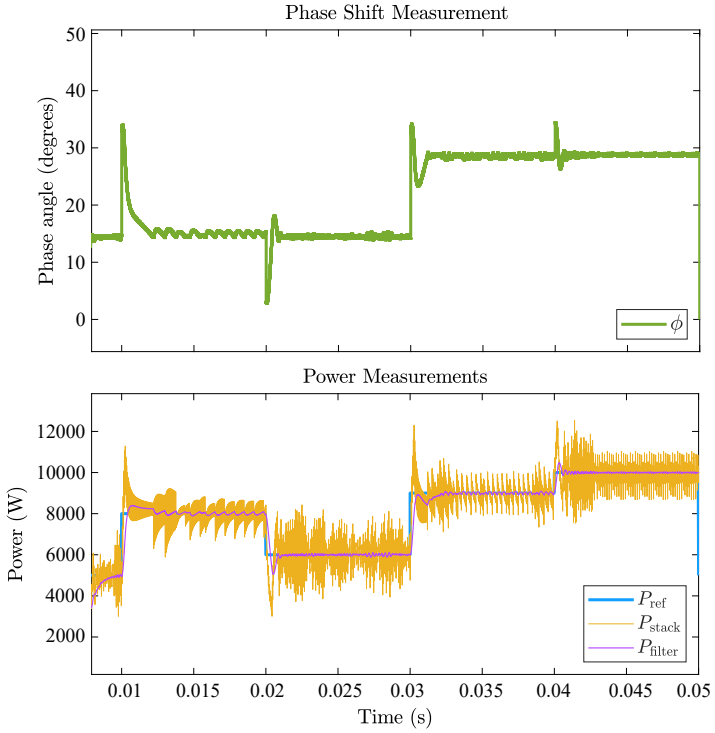

Figure 6.3: PI control measurements for power and phase for Simulink discrete model.

During the simulations, time measurements were made for run time and compiling time. The compiling time is measured at 3 s. The simulation run time to simulate for 50 ms is 5 s.

6.2. PLECS model results

As much noise and oscillations within the control signals were found for the discrete model, a hypothesis was made that simulation errors could be the cause of them. To test this, the electrical part of the Simulink model was placed into PLECS which resulted in the PLECS model. The model output for the PLECS model is discussed in this section.

The leakage inductor voltage and current for the discrete Simulink model are depicted in Figure 6.4. The signals have straightened out in comparison to the Simulink model. The voltage switches without slopes to the next value and the current now shows slopes instead of rounded curves when progressing to the next value. Both signals behave as designed, moving around zero as their baseline at the rate of the switching frequency, and peaking at the expected values of 2800 V and 9.6 A.

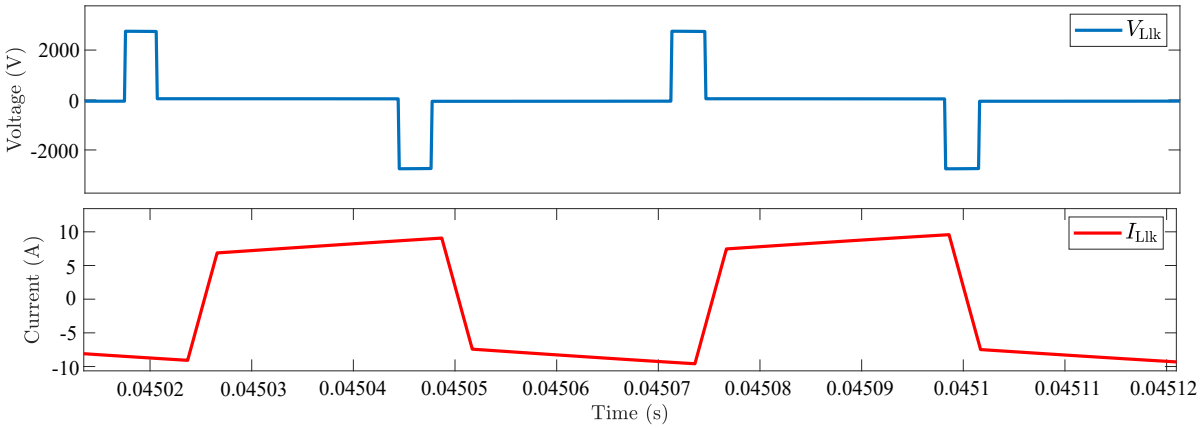

Figure 6.4: Leakage inductor voltage and current measurements for Simulink PLECS hybrid model.

The stack voltage and current for the PLECS model are depicted in Figure 6.5. Both measurements go up and down according to the power reference without filtering. The oscillation in the current and voltage waveform is significantly less than for the discrete Simulink modeling. Due to the lack of oscillations, the maximum current during the power sequence is lower for the PLECS model leakage inductor than for the Simulink model leakage inductor.

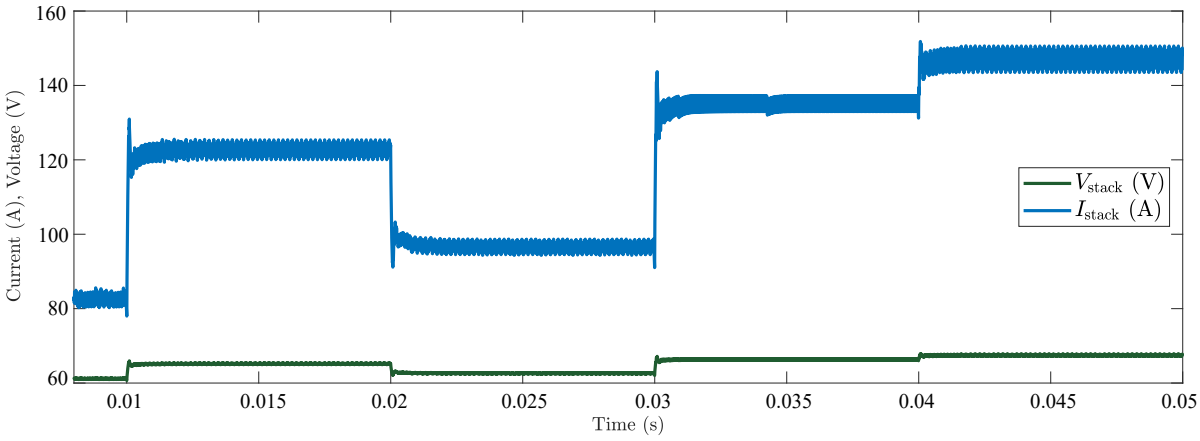

Figure 6.5: Stack voltage and current of the electrolyzer for Simulink PLECS hybrid model.

The PI control response for phase, reference power, and stack power, for the PLECS model is depicted in Figure 6.6. The power oscillation amplitude is now reduced to a maximum of 50 W in steady-state. The PLECS model results show more peaking signals in the phase, which can be seen at for instance the 0.01 s mark. This is also due to the fact that the value of K_p has risen to 0.01. The K_i value was again to be found as 2000. The oscillations stay constant after the settling time. The settling time is reduced in comparison to the Simulink model, for PLECS the settling time is 2 ms.

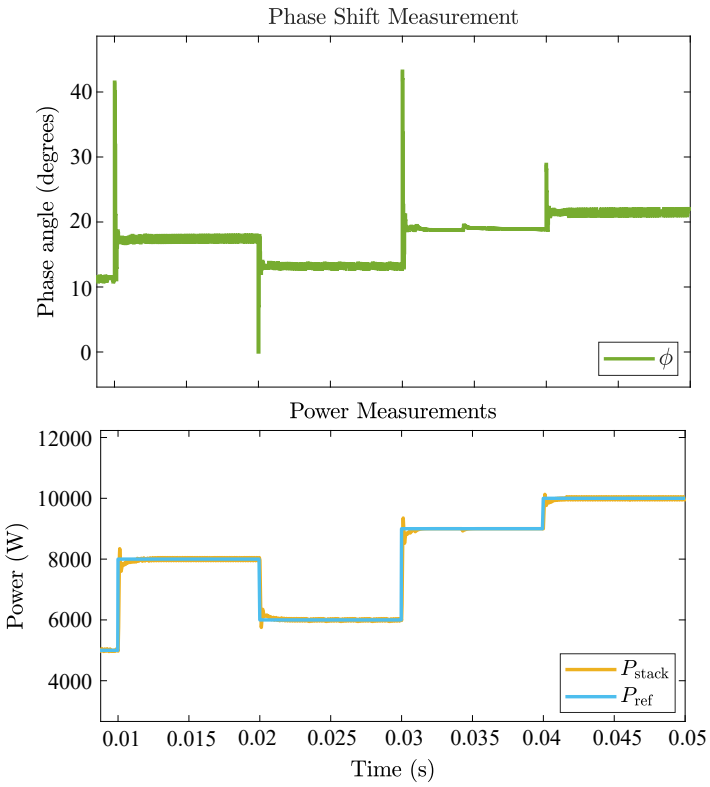

Figure 6.6: PI control measurements for power and phase for Simulink PLECS model.

The PLECS modeling simulation time performance is worse than for Simulink modeling. The time to run the simulation has risen to 205 s. An additional 91 s is added to that when the time the PLECS model needs for building is taken into account. The compilation time of the Simulink part of the model stays equal to the discrete Simulink model at 3 s.

6.3. Digital Twin model results

An RTDT model was made using the OPAL-RT hardware and software, in which the latter has Simulink capabilities. The Simulink models were adapted to fit the needs of the DT environment. A computational subsystem was executed on the OP4610XG hardware and an interface subsystem was executed on the RT-LAB GUI. The eHS toolbox was utilized for the electrical components. Using the DI and DO ports, electrical signals were created to use for the SPS modulation. The model output for the DT OPAL-RT model is discussed in this section. The used setup to gather the data of the RTDT model is depicted in Figure 6.7

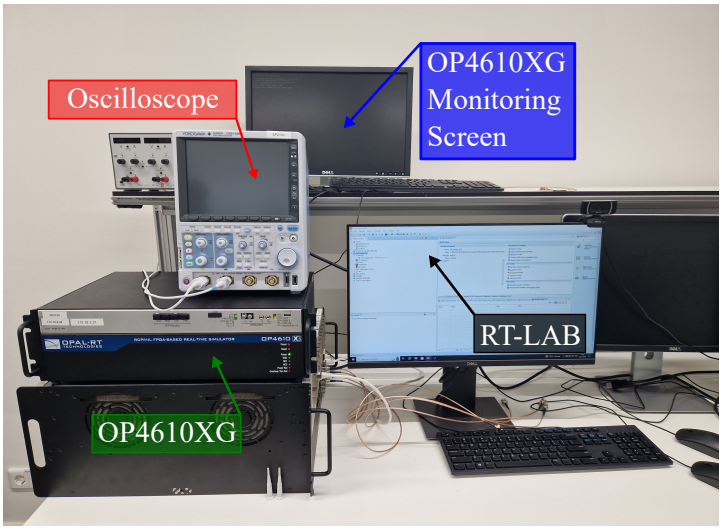

Figure 6.7: Hardware setup to execute the RTDT model and make measurements.

In order to read all the current and voltage signals via the AO channels on the oscilloscope and Scopeview, gains must be applied to the measured signals. The AO channels are only able to create with an absolute maximum of 16 V. The maximum expected value is used to determine the gains, which are displayed in Table 6.1.

Table 6.1: Measurement gains for DT modeling

Measurement	Expected absolute maximum	Gain value
I_{Llk}	16 A	1
V_{Llk}	3000 V	$5.33{*}10^{-3}$
I_{stack}	210 A	$76.2{*}10^{-3}$
V_{stack}	80 V	0.2

The leakage inductor voltage and current for the DT model are depicted in Figure 6.8. The voltage and current have signal spikes moving over time. When taking the gains of Table 6.1 into account, the scaled values match the designed values of peak voltage of 2800 V and peak current of 9.6 A.

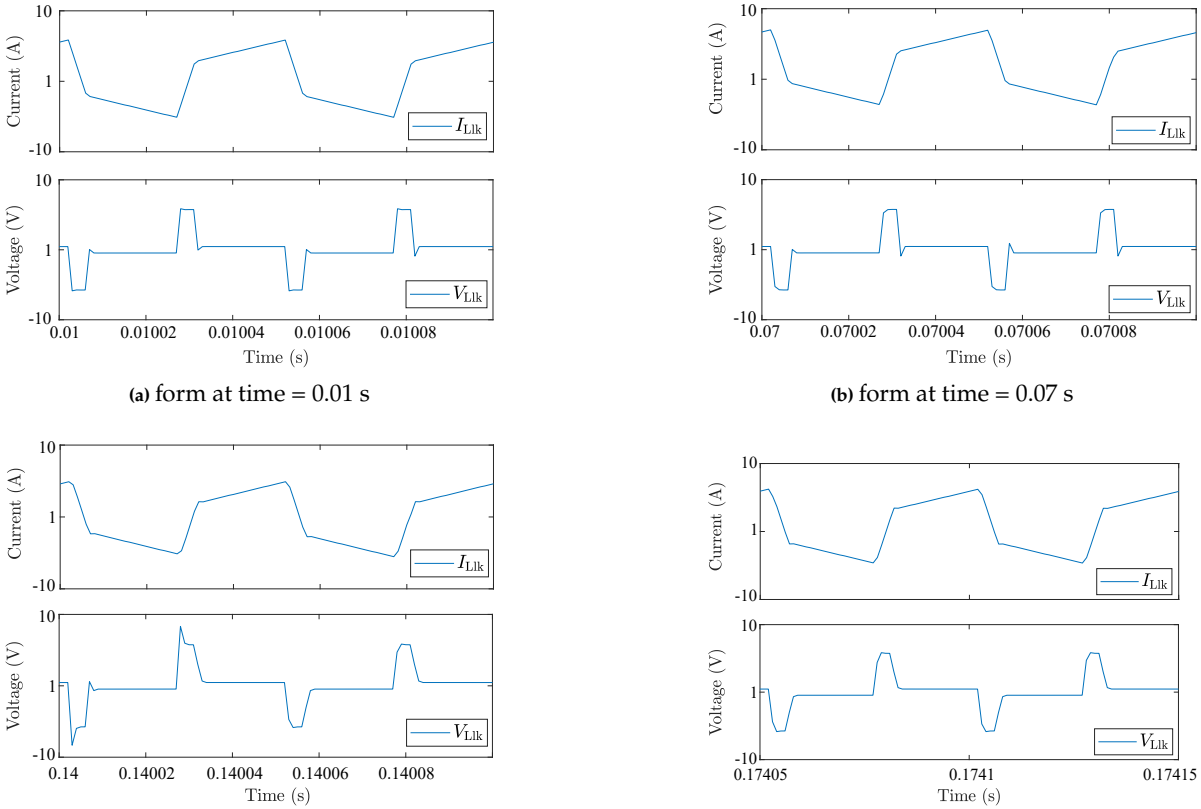

(a) form at time = 0.01 s

(b) form at time = 0.07 s

(c) form at time = 0.14 s

(d) form at time = 0.17 s

Figure 6.8: Current and Voltage measured over the leakage inductor in OPAL, shifting forms over time. Values are normalized for oscilloscope readings using the gains in Table 6.1.

The stack voltage and current for the DT model are depicted in Figure 6.9. Measurements were made at separate moments for different reference power levels as Scopeview cannot show the full sequence. The stack voltage and current have been depicted in Figure 6.9. The voltage is a near-straight line with a small oscillation amplitude whilst the current expresses more oscillations. The voltage has oscillations of less than 0.5% whilst the current portrays oscillations of 5% up to 10%. Current oscillations grow larger for larger values of I_{stack}. The current is depicted below the voltage in Figure 6.9 due to the use of the gains. When taking the gains into account, the voltage and current follow the trends of Figure 3.4.

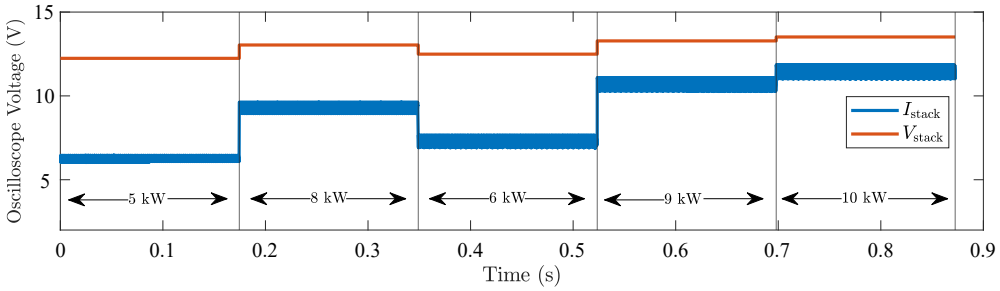

Figure 6.9: Stack voltage and current of the electrolyzer in OPAL-RT, normalized for voltage output of the AO channels using the gains in Table 6.1.

Reference power sequences were put in manually in real time for the OPAL-RT modeling as the previously used reference step signal was too quick to measure in the GUI. The phase shift and power measurements are depicted in Figure 6.10. Two different sequences are shown to summarize the behavior of the signals.

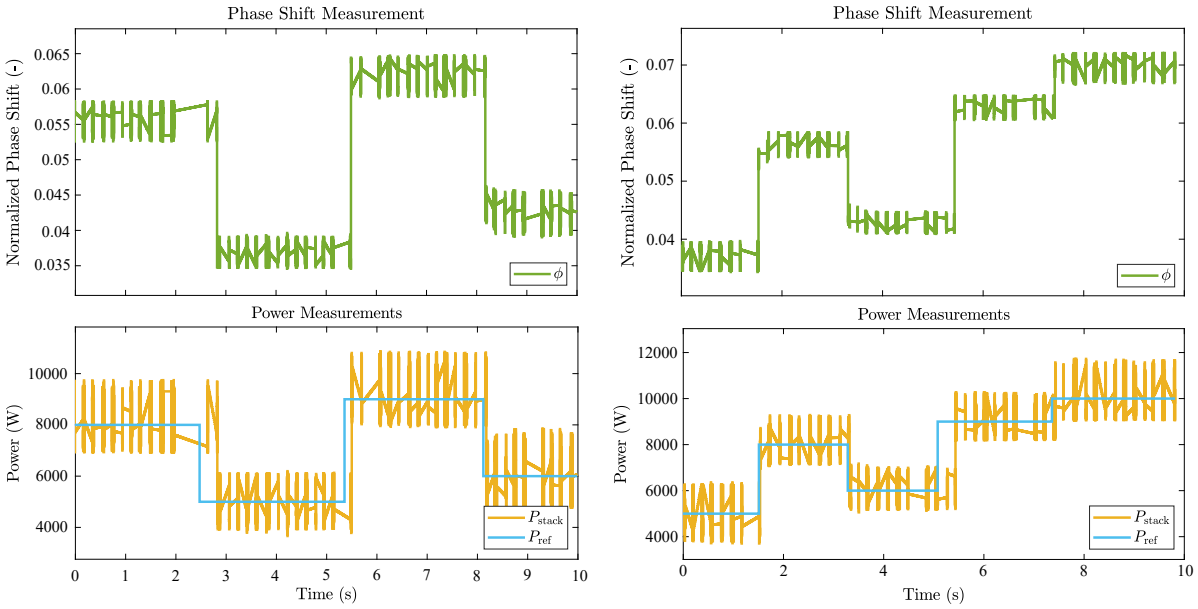

(a) Reference pattern 1

(b) Reference pattern 2

Figure 6.10: PI signals for OPAL-RT modeling.

The RTDT model shows two characteristics: system delays and reoccurring measurement errors in the form of oscillations. The system delays can be seen in Figure 6.10a from the 2 s mark until 3 s and in Figure 6.10b from the 5 s mark until 6 s. The measurement errors occur six times every second unless there is a system delay.

In both sequences the stack power converges for the given reference. During the simulation errors, the power oscillations occur with a minimal amplitude of 1 kW and a maximum of 1.15 kW, where the oscillations become stronger for higher values of power. This excludes oscillations whilst being in a system delay as the system does not realize where the power should be during the time of the error. During system delays, the error can become larger than 1.15 kW

Depending on when the power reference signal is given and when the last error happens, the settling time can change. The settling time is measured for a minimal and a maximal time due to the system delays and the oscillations not solely oscillating around the value of P_{ref}. In Figure 6.10a the slowest settling time happens from 2 s to 3 s whilst in Figure 6.10b the quickest settling time is perceived around the 1.8 s mark.

The DT model allowed to set the values K_p and K_i whilst running the simulation in real time. By accessing the variables tab in the RT-LAB environment, these values (among other variables) were adaptable. The K_p for the DT model is reduced to $2{\times}10^{-6}$ which is significantly lower in comparison to the other models due to the phase being expressed in values of 0.5 to 1 instead of 0 to 45. The K_i value was once more 2000.

The time the DT model needs to get running is significantly longer than for the other models. The model is first compiled within the Simulink environment, then built in the RT-Lab environment in order to use the OP4610XG. which in total takes up 4 m 26 s. After loading the model onto the hardware, the simulation can be immediately started. Since the DT model is able to run as long as desired, the simulation run time and stop time are perceived as N/A and infinite, respectively.

6.4. Performance comparison

By running the simulation of each model, data was gathered on the PI control performance and software performance. Table 6.2 summarizes the data gathered from each of the models in Sections 6.1, 6.2 and 6.3.

Table 6.2: Simulation data for all models

Parameter	Simulink (Discrete)	PLECS	OPAL-RT (DT)
K_p	0.006	0.01	2×10^{-6}
K_i	2000	2000	2000
Settling time PI controller	4 ms	ms	min 0.16 s, max 1 s
Power oscillation amplitude	min 1 kW max 2.5 kW	max 50 W	min 1 kW max 1.15 kW
Simulation stop time	50 ms	50 ms	∞
Simulation run time	5 s	205 s	N/A
Compiling time	3 s	3 s	14 s
Build time	N/A	91 s	4 m 12 s

The PLECS PI control showcases the lowest settling time and the lowest amount of oscillations of the P_{stack} signal. As seen in Figure 6.6, the P_{stack} signal follows the P_{ref} signal with the highest accuracy. The oscillations for Simulink and the DT OPAL-RT model, as depicted in Figures 6.3 and 6.10 respectively, occur due to simulation errors. The Simulink modeling has constant oscillation errors whilst the DT model has errors six times per second. To converge the PI signals for the Simulink model, a filter was required whilst this was not required for the other models.

Whilst the Simulink and PLECS models show K_p near each other, the DT model shows a much lower value. The phase is perceived at an interval of 0 to 1 instead of an interval of 0 to 45° as the SPS signals are created via different methods.

To compile, build, and run the simulation is the quickest in Simulink as a total of 8s is required and no building is required. The total time for a PLECS simulation is longer, but control performance is significantly better. The DT OPAL-RT model has the slowest compiling and building time but allows for changes to be made whilst running for an indefinite amount of time. For instance, the tuning of the PI signals can be done during simulation run time.

To summarize the performance differences, a spider plot is devised and depicted in Figure 6.11 using Sections 6.1, 6.2 and 6.3, and Table 6.2. The meaning of the scores for the spider plot is elaborated in Table 6.3. Scores are given as '1' for worst performing and '5' for best performing in a category.

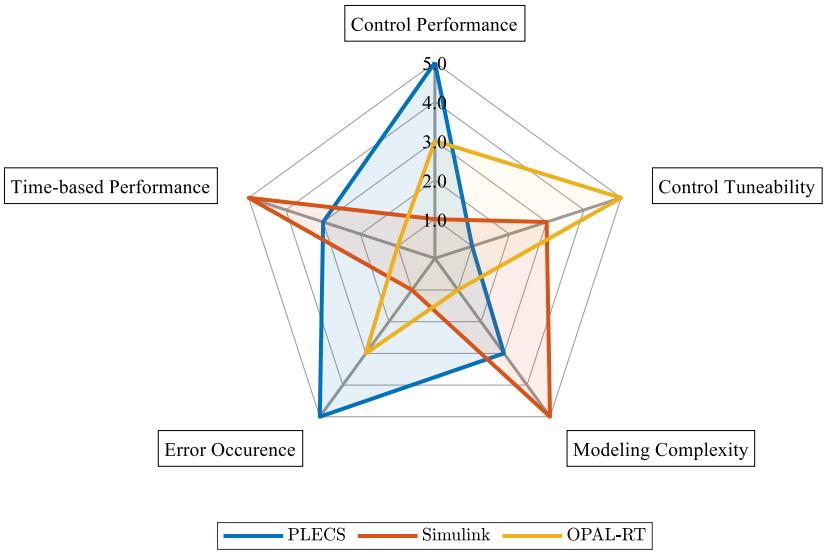

Figure 6.11: Spider plot for the Simulink, PLECS, and OPAL-RT (DT) performance comparison using the information of Table 6.2, and Section 6.1, 6.2 and 6.3.

Table 6.3: Clarification of the scores in Figure 6.11

Category	**1**	**5**
Control Performance	Not converging Long settling time Non-usable signals	Converging, Quick settling time, Usable signals
Control Tuneability	Tuning process is time-consuming	Tuning process is quick and responsive
Modeling Complexity	Extra devices are required Non-straightforward design Data acquisition has limitations	No extra devices are required Straightforward design Data acquisition presents clear data
Error Occurance	Continuously showing simulation errors in signal	No simulation errors occur
Time-based performance	Model runs slow Compiling and Building the model takes a lot of time	Model runs fast Quick compiling and building of the model

PLECS outperforms the other models with its near-ideal control performance and low simulation error occurrence, however, the tuning process of the control signals takes longer than for the other models. The Simulink model outperforms the other models for its low modeling complexity and swift simulation and compiling time, however, the signals are unusable without filtering thus resulting in a low control performance. The DT OPAL-RT model outperforms the other models for its intuitive real-time control tuning but is outperformed by the other models in all the other rated aspects.

7

Conclusions & Recommendations

The work presented in Chapters 2 to 6 is performed to answer the research definition and research questions that were devised in Chapter 1. The answers to the research questions and concluding remarks drawn from the results are discussed in Section 7.1. The sub-research questions are answered first, building up to answering the main research question which in turn helps to answer the research definition. Furthermore, the author highlights recommendations and presents ideas for future studies in Section 7.2.

7.1. Conclusions

For this thesis, emphasis was put on the development of a DT of an electronic power converter for the application of high-power electrolysis in an MVDC grid. Simulink was used to build up toward the DT model and for performance comparison. In total four models were made; a continuous-time Simulink model, a discrete-time Simulink model, a PLECS hybrid Simulink model, and a DT OPAL-RT model.

7.1.1. Design research sub-questions

With the literature review (Chapter 2) and the system design (Chapter 3) made in order to make the models, the design research sub-questions were answered.

- Which electrolyzer type should be used for the application?

AEC, PEMEC, and SOEC have been studied and the literature provided comparisons of the three. An AEC was chosen as this type of electrolyzer is the most well-established technology, is the most cost-effective, has the highest durability, and is designed for the highest hydrogen production rates. The AEC was modeled using methods presented by [41] and [43]. The nominal electrical power requirements for the electrolyzer were chosen to be 10 kW at 70 V.

- Which DC/DC Converter should be used for the application?

DAB, FB, HB, and PP converters have been studied as ISO requires converters in hydrogen environments to have isolated HV and LV sides. Using the literature found and models of each converter with the step-down and power requirements, a comparison was made. A DAB was chosen as this technology is able to perform with high efficiency at high-power applications and offers growth for future studies including series-parallel arrangements and bidirectional capabilities for implementing a full P2PH network. The DAB was designed for a rated power of 10 kW at a phase of 25° with an input voltage of 1400 V to comply with MVDC grid levels and output voltage of 70 V to comply with the nominal electrolyzer levels. The DAB operated at 20 kHz in order to work in all Simulation environments as the DT environment significantly dropped in measurement accuracy for higher frequencies.

- What is the most optimal control and/or modulation strategy for the application?

To minimize complexity, the modulation and control strategies were chosen so only one parameter was necessary to control the power level outputted by the DAB. The combination of PI control and SPS modulation was therefore made to only have the phase shift ϕ as a parameter. The PI control reacted to a reference power signal and the power measurement at the LV side of the DAB. The PI control outputs the desired phase shift to the SPS modulation, which applies the phase shift on the LV side of the DAB. For each model, the K_p and K_i values were tuned using trial and error.

7.1.2. Comparison sub research questions

After designing and running the Simulink and DT models (Chapters 4 and 5), data was recorded in various topics. The results from these data were discussed in Chapter 6. Using these chapters, the comparison research sub-questions can be answered.

- What data will be used to compare the Digital Twin and Simulink models?

To assess control performance, error occurrence, and time-based performance, the PI control signals P_{ref}, P_{stack} and ϕ were plotted and the time to compile, build, and run the models was measured. From PI plots, the settling time, error magnitude and frequency, and oscillations were measured. The process of modeling and tuning as explained in Chapters 4 and 5 were taken into account to assess control tuneability and modeling complexity.

- How does the Simulink model perform for the application?

The continuous time Simulink model performed near ideal as oscillations were kept low and settling time was quick whilst having fast compiling and running of the model. However, as DTs are discrete models, comparisons can not be made. A discretized version of the same model was made which kept its good performance for compiling and running but showed oscillations ranging from 1 kW up to 2.5 kW. Filtering was required to realize PI signal conversion and a settling time. A hypothesis was made that the oscillations could occur through constant simulation errors. To test this hypothesis, a Simulink model version was made where PLECS was used to model the electrical components. For the PLECS model, the total time to compile, build, and run the model increased, and the oscillations decreased to a maximum of 50 W.

- How does the Real-time Digital Twin model perform for the application?

The DT model has the capability that the K_p and K_i can be adapted whilst running the model for an indefinite amount of time. This made the process of tuning the PI signals quick and responsive. However, before this capability is ready for the user, the total compiling and building time of the model is 4 m 26 s. The PI signals converge with a minimal settling time of 0.16 s, which is eight times slower than for the PLECS model. The PI signals of the DT model showed that measurement errors occur six times every second which was portrayed with oscillations. System delays occurred within the measurements as well, which led to longer responses to the reference signals.

7.1.3. Main research question

The main research question can be answered by combining the answers of the research sub-questions.

- What is gained from utilizing a Real-time Digital Twin in comparison to simulation models in achieving a robust design for a DC/DC converter topology for electrolysis?

When utilizing the current DT OPAL-RT model, the ability to tune the control signals in real-time is gained. However, the Simulink PLECS hybrid model control performance is observed to be more accurate and faster due to lower oscillations, fewer errors during the simulation, and faster control signal convergence. When comparing the DT OPAL-RT model for solely Simulink modeling, the DT OPAL-RT model was observed to show less strong oscillation and fewer error occurrences. The main trade-off of using the DT OPAL-RT model is its increased modeling complexity.

However, this answer is bounded by the modeling techniques. RTDTs can be made using different software or can be expanded to test the control on a physical DAB (with test loads and sources). The current DR OPAL-RT model shows structural measurement errors in the form of temporary oscillations and system delays. These can possibly be avoided by using different measurement methods or modeling. The switching frequency in all models was kept at 20 kHz as the OPAL-RT environment did not support accurate component measurements for higher switching frequencies. In industrial-level designs, higher switching frequencies are used. Changing the switching frequency could lead to different results for the control performance.

The answer is also bounded by the current design implemented. This design did not consider the full P2PH network including MVDC loads and PV and FC electricity generation. The addition of these may influence the performance of the control. The DAB was designed for 10 kW and an input voltage of 1400 V and controlled for an output voltage of nominally 70 V using PI control and SPS modulation. Any changes in the converter topology, the converter specifications, the control strategy, or the modulation strategy may lead to different results. An AEC was modeled with the methods of [41], different AEC modeling methods and specifications could lead to different results.

7.1.4. Concluding remarks

The problem defined in Section 1.1.1 is not completely solved, but a step is made towards it. For the current design, the DT is not the most reliable method to assess the robustness of the design yet, however, The Simulink PLECS hybrid showed the most robust results out of the models. Therefore, the Simulink PLECS hybrid model has the greatest potential to be utilized for a real industrial-level application. The DT approach can be developed further according to the recommendation made in Section 7.2

7.2. Recommendations

The work presented in this thesis can be utilized or modified for different uses. An overview of the suggested recommendations is listed below.

Overview of recommendations

- Acquire data of OPAL-RT model with different methods
- Use different component specifications for the DAB and electrolyzer
- Create Hardware in the Loop (HIL) systems with DAB and/or electrolyzer
- Compare more DT brands to verify results
- Complete the system design to a full P2PH network
- Change converter design for multilevel topologies and full P2PH network design
- Utilize DT modeling for more types of converter analysis

More methods of data acquisition in real-time can be tried to check whether the perceived errors in the SC_GUI are throughout the whole model. The OPWriteFile block was tried but without success, which can be retried in future endeavors. The measurements can also be brought to Scopeview or oscilloscopes by creating analog signals with the P_{ref}, P_{stack} and phase signals.

The electrolyzer was modeled according to the measurements provided by [41]. The DAB and electrolyzer can be adjusted for different electrolyzer specifications to provide results for real applications.

A HIL system can be created by making a converter design (and/or electrolyzer design) into a physical object and connecting it to the DT inputs and outputs. A Printed Circuit Board (PCB) containing the DC/DC converter(s) and control connections can be connected to the AO and DO channels of the DT system. The control can be implemented via the DT whilst the electrical side is moved to the physical world. This technique allows for safe control reliability tests and component performance assessments.

Within this research, OPAL-RT technology was utilized for the DT. The performance for the same power conversions can be compared for different DT brands. Comparing system performance and electrical accuracy is recommended to follow up on the results of this thesis.

The system architecture can be adapted to include more components of the P2PH network. This thesis simplified the MVDC grid, and the FC and PV generation in a P2PH network. The PV generation can be added by controlling the reference signal according to the generated power. The FC and electrolyzer will require network-level electricity management to prevent interference from each other. To utilize the generated green energy, loads can be added to the MVDC grid.

The converter design can include multilevel topologies to increase the amount of electrolyzers used per converter instance or vice versa. As concluded in Chapter 3, the DAB is a very suitable converter for modifications. Parallel H-HV and/or H-LV bridge topologies such as depicted in [45] can be utilized to reduce component stresses and optimize efficiency. Different types of phase shift modulations such as EPS and TPS can be implemented and tested. These, in turn, have an effect on the (type of) control strategy. The addition of a more in-depth MVDC grid can also give rise to the addition of more components in the converter which will require a re-evaluation of the converter design.

When utilizing DT modeling for converter analysis, possibilities lie in modeling for more control strategies, thermal modeling, online health estimation, monitoring, and in-depth component analysis. These can be implemented by building upon the DT modeling methods of this thesis. For thermal and component analysis, the eHS toolbox is not sufficient as it does not have any data entries regarding this in the component models. The electrical modeling should be split up into multiple parts to facilitate these analysis possibilities.

7.2.1. Future work

Researchers at the department of DCE&S at the faculty of EEMCS will be continuing their research with the use of this thesis. A HIL system will be created by designing and producing a DAB with connection points to the DT. The main focus will be on controlling the DAB. In parallel, the RT Box by PLECS will be utilized to compare its performance to that of the OPAL-RT.

References

1. Huet, N. *euronews.com* https://www.euronews.com/next/2022/11/24/europe-energy-crisis-is-boosting-green-hydrogen-is-it-finally-a-real-alternative.
2. Taibi, E. *et al. Hydrogen from renewable power: Technology outlook for the energy transition* ISBN: 978-92-9260-077-8. www.irena.org (2018).
3. Vidas, L. & Castro, R. Recent developments on hydrogen production technologies: State-of-the-art review with a focus on green-electrolysis. *Applied Sciences (Switzerland)* **11.** ISSN: 20763417 (23 Dec. 2021).
4. Guilbert, D. & Vitale, G. Hydrogen as a Clean and Sustainable Energy Vector for Global Transition from Fossil-Based to Zero-Carbon. *Clean Technologies* **3,** 881–909. ISSN: 25718797 (4 Dec. 2021).
5. Jaribion, A., Khajavi, S. H., Öhman, M., Knapen, A. & Holmström, J. A Digital Twin for Safety and Risk Management: A Prototype for a Hydrogen High-Pressure Vessel. *Lecture Notes in Computer Science (including subseries Lecture Notes in Artificial Intelligence and Lecture Notes in Bioinformatics)* **12388 LNCS,** 369–375. ISSN: 16113349 (2020).
6. MathWorks. *Digital Twins for Predictive Maintenance* (2023).
7. Glaessgen, E. H. & Stargel, D. S. The Digital Twin Paradigm for Future NASA and U.S. Air Force Vehicles (2012).
8. Stark, R. & Damerau, T. Digital Twin. *CIRP Encyclopedia of Production Engineering*, 1–8. http://link.springer.com/10.1007/978-3-642-35950-7_16870-1 (2019).
9. Moghadam, H. M., Foroozan, H., Gheisarnejad, M. & Khooban, M. H. A survey on new trends of digital twin technology for power systems. *Journal of Intelligent and Fuzzy Systems* **41,** 3873–3893. ISSN: 18758967 (2 2021).
10. UNFCCC. *Paris Agreement* (United Nations, 2015).
11. UNFCCC. *Decision-/CP.27 Sharm el-Sheikh Implementation Plan* (United Nations, Nov. 2022). https://public.wmo.int/en/our-.
12. Rijksoverheid. *Coalitieakkoord 2021 – 2025* (Rijksoverheid, Dec. 2021).
13. Of Economic Affairs, M. & of the Netherlands, C. P. *Eighth Netherlands National Communication Under The United Nations Framework Convention On Climate Change Ministry of Economic Affairs and Climate Policy* (Ministry of Economic Affairs and Climate Policy of the Netherlands, Dec. 2022).
14. Programma, N. W. *Hydrogen Roadmap for the Netherlands* (2021). www.nationaalwaterstofprogramma.nl.
15. Guilbert, D. & Douine, B. Literature Survey of Interleaved DC-DC Step-Down Converters for Proton Exchange Membrane Electrolyzer Applications. *TRANSACTIONS ON ENVIRONMENT AND ELECTRICAL ENGINEERING* **3** (1 2019).
16. Koponen, J. *Review of water electrolysis technologies and design of renewable hydrogen production systems* (2015).
17. Nami, H., Rizvandi, O. B., Chatzichristodoulou, C., Hendriksen, P. V. & Frandsen, H. L. Techno-economic analysis of current and emerging electrolysis technologies for green hydrogen production. *Energy Conversion and Management* **269.** ISSN: 01968904 (Oct. 2022).
18. Pei, W., Zhang, X., Deng, W., Tang, C. & Yao, L. Review of Operational Control Strategy for DC Microgrids with Electric-hydrogen Hybrid Storage Systems. *CSEE Journal of Power and Energy Systems* **8,** 329–346. ISSN: 20960042 (2 Mar. 2022).
19. Rashid, M. *et al. Hydrogen Production by Water Electrolysis: A Review of Alkaline WaterElectrolysis, PEM Water Electrolysis and High Temperature Water Electrolysis* (2015), 2249–8958. https://www.researchgate.net/publication/273125977.

20. Kumar, S. S. & Lim, H. An overview of water electrolysis technologies for green hydrogen production. *Energy Reports* **8,** 13793–13813. ISSN: 23524847 (Nov. 2022).
21. Alhurayyis, I., Elkhateb, A. & Morrow, J. Isolated and Nonisolated DC-to-DC Converters for Medium-Voltage DC Networks: A Review. *IEEE Journal of Emerging and Selected Topics in Power Electronics* **9,** 7486–7500. ISSN: 21686785 (6 Dec. 2021).
22. Andrijanovitsh, A., Steiks, I., Zakis, J. & Vinnikov, D. Analysis of State-of-the-Art Converter Topologies for Interfacing of Hydrogen Buffer with Renewable Energy Systems. *Scientific Journal of Riga Technical University. Power and Electrical Engineering* **29.** ISSN: 1407-7345 (1 Oct. 2011).
23. Guilbert, D., Collura, S. M. & Scipioni, A. DC/DC converter topologies for electrolyzers: State-of-the-art and remaining key issues. *International Journal of Hydrogen Energy* **42,** 23966–23985. ISSN: 03603199 (38 2017).
24. Guida, V., Guibert, D. & Douine, B. *Candidate Interleaved DC-DC Buck Converters for Electrolyzers: State-of-the-Art and Perspectives* ISBN: 9781538651865 (2018).
25. Gorji, S. A. Reconfigurable Quadratic Converters for Electrolyzers Utilized in DC Microgrids. *IEEE Access* **10,** 109677–109687. ISSN: 21693536 (2022).
26. Viswamohan, K. & Jayakrishna, G. *Soft-Switching Techniques for DC-to-DC Converters in Electrolyzer Application* (2014), 1021–1026. `www.ijatir.org`.
27. Zhang, C., Wang, J., Pan, Y., Diao, Y. & Li, D. A DC/DC Converter for Electrolytic Hydrogen Production Based on DC Microgrid. *PEAC 2022 - 2022 IEEE International Power Electronics and Application Conference and Exposition, Proceedings,* 1348–1353 (2022).
28. Tao, F., Zhang, H., Liu, A. & Nee, A. Y. Digital Twin in Industry: State-of-the-Art. *IEEE Transactions on Industrial Informatics* **15,** 2405–2415. ISSN: 15513203 (4 Apr. 2019).
29. Attaran, M. & Celik, B. G. Digital Twin: Benefits, use cases, challenges, and opportunities. *Decision Analytics Journal* **6,** 100165. ISSN: 27726622 (Mar. 2023).
30. Shin, Y., Oh, J., Jang, D. & Shin, D. Digital Twin of Alkaline Water Electrolysis Systems for Green Hydrogen Production. *Computer Aided Chemical Engineering* **49,** 1483–1488. ISSN: 15707946 (Jan. 2022).
31. Zhao, D. *et al.* A data-driven digital-twin model and control of high temperature proton exchange membrane electrolyzer cells. *International Journal of Hydrogen Energy* **47,** 8687–8699. ISSN: 0360-3199 (14 Feb. 2022).
32. Folgado, F. J., González, I. & Calderón, A. J. PEM Electrolyser Digital Twin Embedded within MATLAB-Based Graphical User Interface. *Engineering Proceedings* **19.** ISSN: 2673-4591. `https://www.mdpi.com/2673-4591/19/1/21` (2022).
33. Xiong, J. *et al.* A monitoring and diagnostics method based on FPGA-digital twin for power electronic transformer. *Electric Power Systems Research* **210.** ISSN: 03787796 (Sept. 2022).
34. Peng, Y., Zhao, S. & Wang, H. A Digital Twin Based Estimation Method for Health Indicators of DC-DC Converters. *IEEE Transactions on Power Electronics* **36,** 2105–2118. ISSN: 19410107 (2 Feb. 2021).
35. Nezio, G. D., di Benedetto, M., Lidozzi, A. & Solero, L. Digital Twin based Real-Time Analysis of DC-DC Boost Converters. *2022 IEEE Energy Conversion Congress and Exposition, ECCE 2022* (2022).
36. Chen, S., Wang, S., Wen, P. & Zhao, S. Digital Twin for Degradation Parameters Identification of DC-DC Converters Based on Bayesian Optimization. *2021 IEEE International Conference on Prognostics and Health Management, ICPHM 2021* (June 2021).
37. Lima, A. A. D. M., Souza, F. A. A., Morais, E. E. C., Honorio, D. D. A. & Barreto, L. H. S. Proof of concept of Fault Detection and Identification Framework applied in Power Converter based on Digital Twins. *2022 Workshop on Communication Networks and Power Systems, WCNPS 2022* (2022).
38. Dias, J. M. & Lino, B. *Digital Twin (DT) of a DC-DC converter for Photovoltaic (PV) Applications* (Mestrado em Engenharia Eletrotécnica e de Computadore, Nov. 2022).
39. Tao, F., Xiao, B., Qi, Q., Cheng, J. & Ji, P. Digital twin modeling. *Journal of Manufacturing Systems* **64,** 372–389. ISSN: 02786125 (July 2022).

40. Olivier, P., Bourasseau, C. & Bouamama, P. B. Low-temperature electrolysis system modelling: A review. *Renewable and Sustainable Energy Reviews* **78,** 280–300. ISSN: 18790690 (2017).

41. Ursúa, A. & Sanchis, P. Static-dynamic modelling of the electrical behaviour of a commercial advanced alkaline water electrolyser. *International Journal of Hydrogen Energy* **37,** 18598–18614. ISSN: 03603199 (24 Dec. 2012).

42. David, M., Alvarez, H., Ocampo-Martinez, C. & Sánchez-Peña, R. *Dynamic modelling of Alkaline self-pressurized electrolyzers: a phenomenological-based semiphysical approach* (2020).

43. Ulleberg, I. Modeling of advanced alkaline electrolyzers: a system simulation approach. *International Journal of Hydrogen Energy* **28,** 21–33. `www.elsevier.com/locate/ijhydene` (2003).

44. Deshmukh, R. S. *et al.* Implementation of Real-Time Digital Twin of Dual Active Bridge Converter in Electrolyzer Applications (2023 [TO BE PUBLISHED]).

45. Deshmukh, R. S., Shekhar, A. & Bauer, P. *Adaptive Modularity for Power Electronics Based Electrolysis Systems for Green Hydrogen* (2022).

46. Akagi, H., Kinouchi, S.-i. & Miyazaki, Y. Bidirectional isolated dual-active-bridge (DAB) DC-DC converters using 1.2-kV 400-A SiC-MOSFET dual modules. *CPSS Transactions on Power Electronics and Applications* **1,** 33–40 (2016).

47. Bu, Q., Wen, H., Shi, H. & Zhu, Y. A Comparative Review of High-Frequency Transient DC Bias Current Mitigation Strategies in Dual-Active-Bridge DC-DC Converters under Phase-Shift Modulations. *IEEE Transactions on Industry Applications* **58,** 2166–2182. ISSN: 19399367 (2 2022).

A

Code & Model screenshots

This appendix presents the codes used and screenshots of the models used. Section A.1 shows the code generated for the Simulink model, Section A.2 shows the screenshots of the Simulink model, Section A.3 shows the code generated for the PLECS model, Section A.4 shows the screenshots of the PLECS model, lastly Section A.5 shows the code generated for the OPAL RT model and Section A.6 shows the screenshots of the OPAL RT model.

A.1. Simulink Model Code

This section presents the code which is run before running the Simulink model.

```
    %% Initialization file for DAB module SIMULINK MODEL
% Made by N. Lock and R.S. Deshmukh
% Version 20-7-2023
clc
clear

%% QUICK ACCES : GUI
t_stop = 0.05; %stop time simulation (s)
fsw = 20e3; %switching frequency (Hz)
P_rated = 10e3; %rated power DAB (W)
phi_init = 25; %initial phas shift (deg)

%% Electrolyzer modelling + Lookup Table
N_s = 36; %series connected cells
N_series = 1; %series connected stacks
N_par = 1; %parallel connected stacks

% modelling reversible voltage of the cell
T_cell_C = 15:10:65; %Cell Temperature sweep in Celsius
T_cell = T_cell_C + 273.15; %Cell Temperature sweep in Kelvin
% constants for reversible potential (V/K)
a_rev = [1.5421e-3, 9.526e-5, 9.84e-8];

%Temperature dependent reversible potential in (V)
U_rev_0 = (1.5184 - a_rev(1)*T_cell + a_rev(2)*log(T_cell).*T_cell
+ a_rev(3)*T_cell.^2);

%Alkaline Electrolyte KOH 30% wt
m = 7.64; % mol/Kg
```

```
a = -0.0151*m - (1.6788e-3)*m^2 + (2.2588e-5)*m^3; %vapor calc a
b = 1 - (1.2062e-3)*m + (5.6024e-4)*m^2 - (7.8228e-6)*m^3; %vapor calc b

%vapor pressure H2O (Pa)
P_v_H2O = exp(81.618 - 7699.7*T_cell.^-1 - 10.9*log(T_cell)
+ 9.589e-3 * T_cell);

%KOH vapor pressure
P_v_KOH = exp(2.302*a + b*log(P_v_H2O));

% Water activity in KOH (Pa)
a_H2O_KOH = exp((51.92e-3)*m+ (3.3e-3)*m^2
+ (3.3177*m - 2.131*m^2)./T_cell);

%Reversible Potential calc
P_abs = 5; %pressure of electrolyzer cell (bar)
R = 8.314463; %R constant
F = 96485; %Faraday constant
z = 2; %amount of electrons

%reversible potential for T_cell (V)
U_rev = N_s*(U_rev_0 +
(R.*T_cell)./(z*F).*log(((P_abs -P_v_KOH).^1.5)./a_H2O_KOH));

%Activiation potential
S_set=  [25.23e-3, -234.0338e-6, 3.1832e-6];
T_set = [54.6185e-3, -2.4601e-3, 52.1217e-6];
V_set = [110.3623e-3, -1.6466e-3, 22.8382e-6];
W_set = [45.7027, 0.7781, -10.5743e-3];

S = S_set(1) + S_set(2).*T_cell_C + S_set(3).*T_cell_C.^2;
T = T_set(1) + T_set(2).*T_cell_C + T_set(3).*T_cell_C.^2;
V = V_set(1) + V_set(2).*T_cell_C + V_set(3).*T_cell_C.^2;
W = W_set(1) + W_set(2).*T_cell_C + W_set(3).*T_cell_C.^2;

% Capacitances associated with the double layer at electrodes
C_el_a = 0.6375; %(F)
C_el_c = 0.0307; %(F)

% Step - 3 Ohmic Losses
R_set = [59.5482e-6, -340.8224e-9, -106.9708e-6, 2.7075e-3];
A = 300e-4; % Electrode Area (m^2)

% Temperature dependent resistivity
r = R_set(1) + R_set(2).*(T_cell_C) + R_set(3)./(T_cell_C)
+ R_set(4)./(T_cell_C).^2;

Farad_eff = 0.95; % faradaic efficiency

% Script for plotting the characteristics
% Do not change the number of points. This will lead to power inaccuracies.
i_cell = 0:0.0001:180; %init i_cell
U_cell = zeros(length(T_cell_C),length(i_cell));
R_int = zeros(1,6);
for i = 1:length(T_cell_C)
    for j = 1:length(i_cell)
```

```
        R_int(1,i) = N_s*r(i)/A; % Internal Resistance

        U_ohm = i_cell(j)*R_int(1,i); %Ohmic Potential


        %Activation currents
        i_act_anode = i_cell(j); %anode and cathode currents are equal
        i_act_cathode = i_act_anode;

        %Voltages acros anode, cathode & cell
        U_act_anode= N_s*S(i)*log(i_act_anode/(T(i)) + 1);
        U_act_cathode= N_s*V(i)*log(i_act_cathode/(W(i)) + 1);
        U_cell(i,j) = N_series*(U_rev(i)
        + U_act_anode + U_act_cathode + U_ohm);
    end
end

figure(1)
plot(i_cell, U_cell)

%% DAB modelling
% ----------------- Settings -----------%
%MVDC/INPUT
V_DC = 1400; %input voltage in V
C_in = 100e-6; %input capacitor capacitance
R_in = 1e-3; %input capacitor capacitance


%output
V_o = 70; %estimated rated output voltage

%resistors
R_lk = 1e-3; %(Ohm)
R_o = R_in; %(Ohm)

% SPS & Control
phi_c = 180; %carrier phase of the SPS modulator (deg)
phi_up = 45; %saturator upper bound (deg)
phi_low = 0; %saturator lower bound (deg)
K_p = 3e-3; %Kp value for PI
K_i =2000;  %Ki value for PI
f_lpf = 500; %(Hz)
tau = 1/(2*pi*f_lpf);


% MOSFET values
Ron = 1e-4; %on resistance (Ohm)
Rd = Ron; %diode resistance (Ohm)
Rs = 1e5; %snubber resistance (Ohm)
Cs = inf; %snubber capacitance (F)
Vf = 0; %Foward voltage drop (V)

% transformer
magnz = [1e6 inf]; %magnetization values tranformer (Ohm, H)
wind1 = [V_DC, 0, 0];
```

```
wind2 = [V_o, 0 , 0];
pf = [P_rated, fsw];



% ---------------- calculations -----------%
N = V_DC/V_o; %primary to secondary transformer turns ratio
n = 1/N;
d = phi_init/180; %normalize phase shift
Ts = 1/fsw; %Switching time
L_lk = V_DC*V_o*d*(1-d)/(2*n*P_rated*fsw); %Leakage inductance in H
%C_o = V_DC*d^2*Ts^2*((1-d)+d^2/4)/(4*L_lk*n); %calculation for output
%capacitor

% calculator for lookup table control
P_cell = U_cell(1,:).*i_cell; %cell power
%Determine lookup
Deter = sqrt((-1)^2 -
8*U_cell(1,:).*i_cell*L_lk*fsw./(V_DC*U_cell(1,:)*N)));
D = abs(0.5*(1 - Deter)); % Correct solution
phi_1 = D*180; % Converting the phase shift ratio into phase angle
```

A.2. Simulink Model Screenshots

This section presents screenshots of the Simulink model. All subsystems are included.

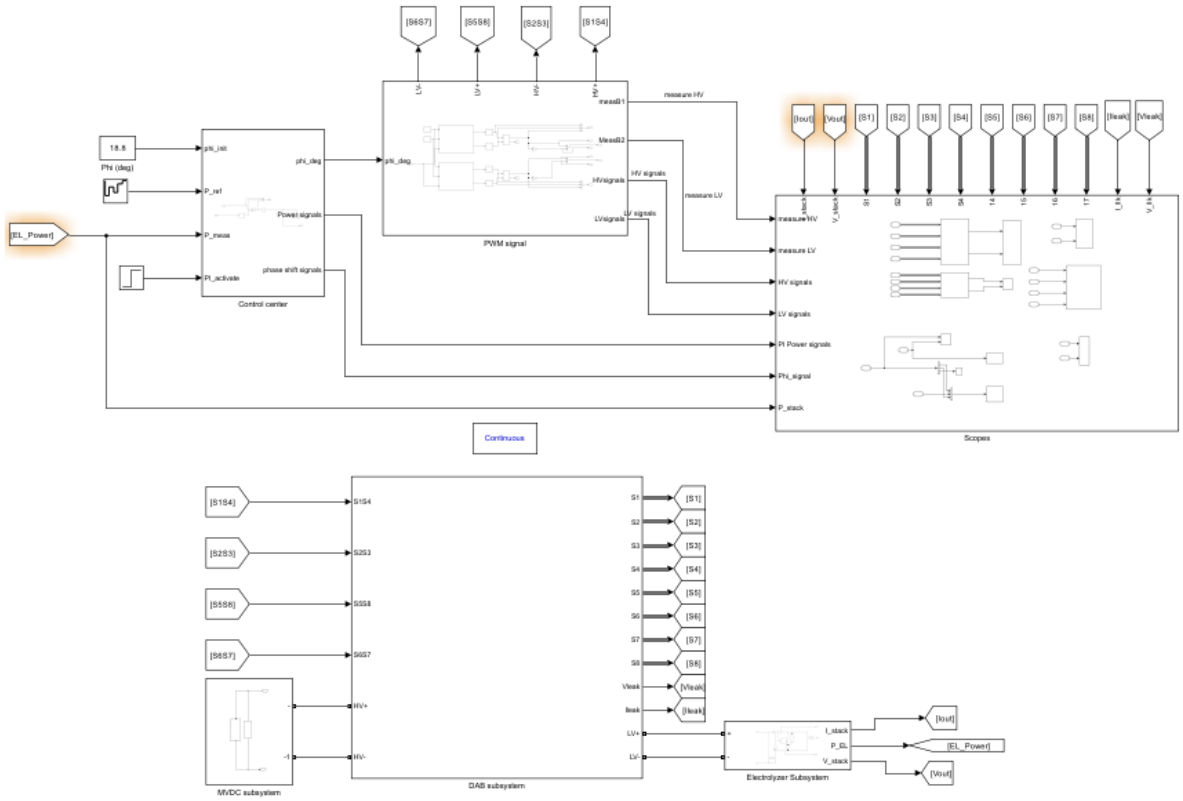

Figure A.1: Simulink model top view.

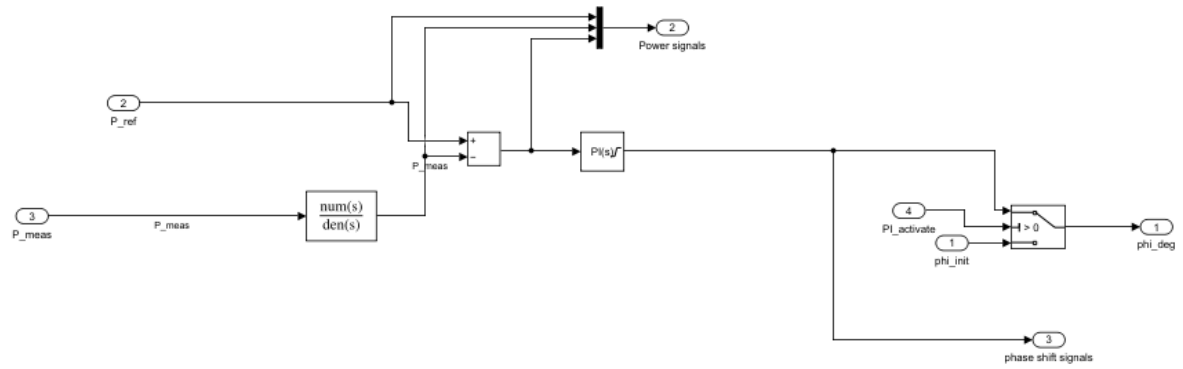

Figure A.2: Simulink model Control subsystem.

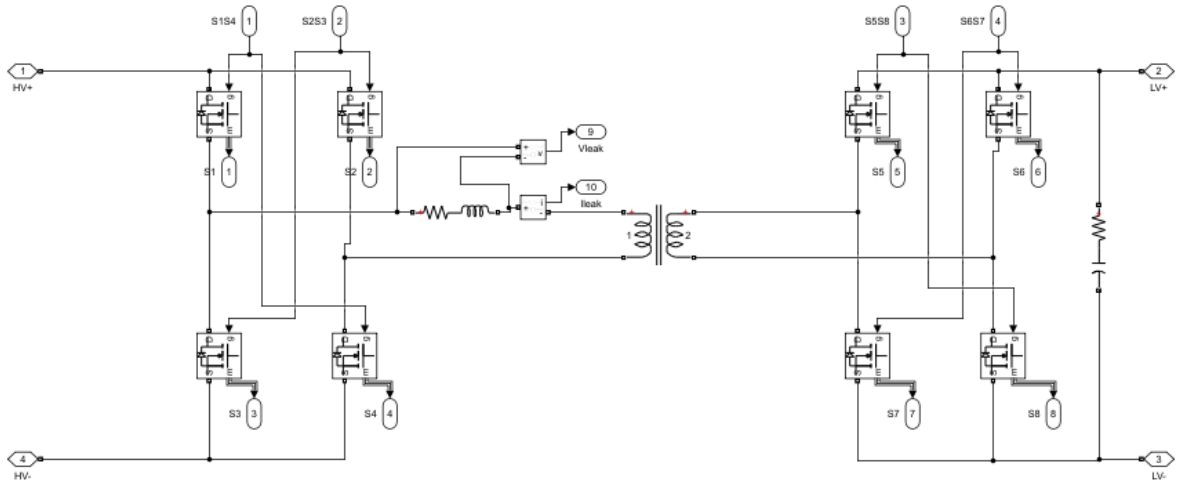

Figure A.3: Simulink model Dual Active Bridge subsystem.

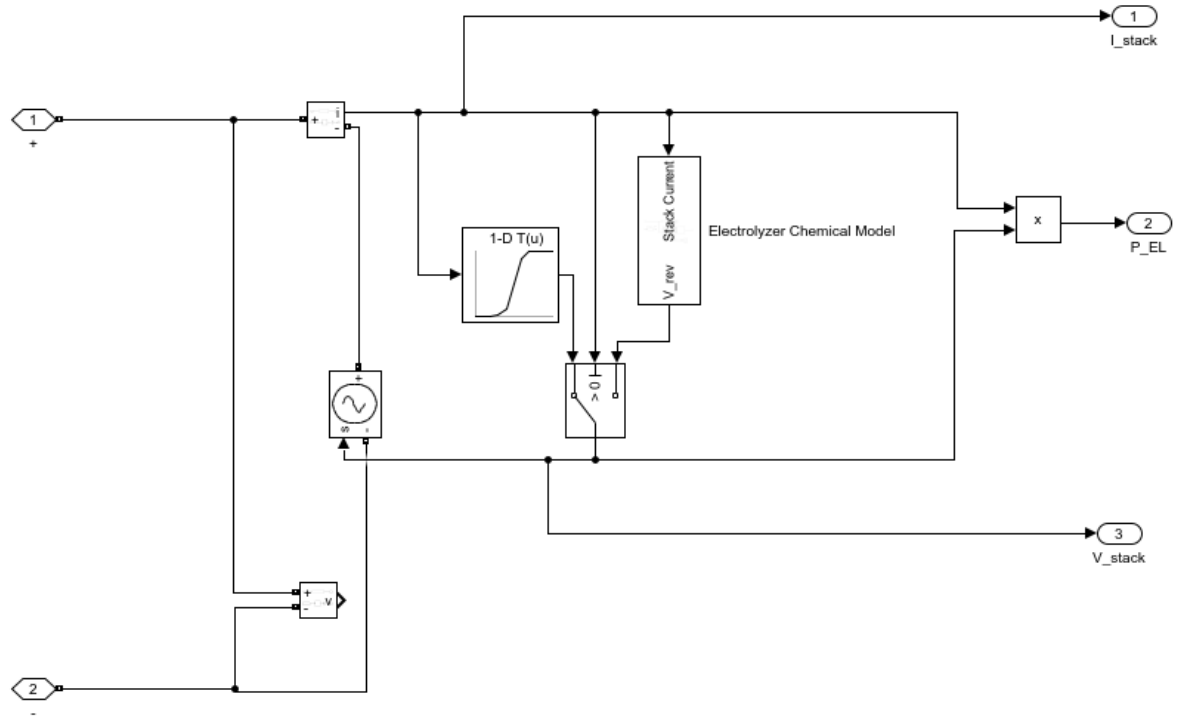

Figure A.4: Simulink model Electrolyzer subsystem.

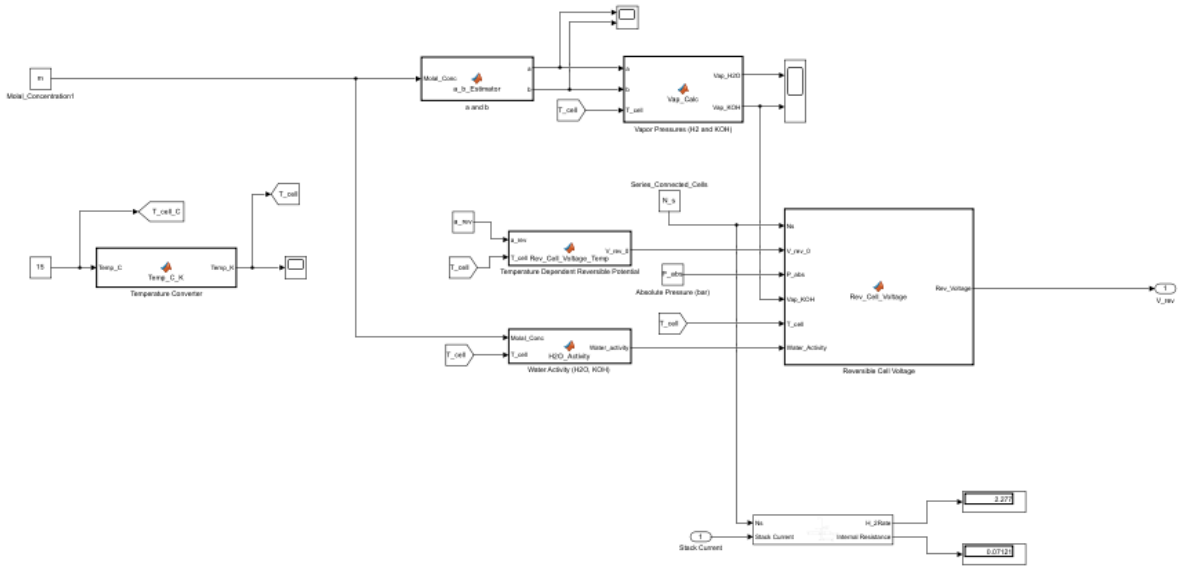

Figure A.5: Simulink model EL subsystem, chemical model subsystem.

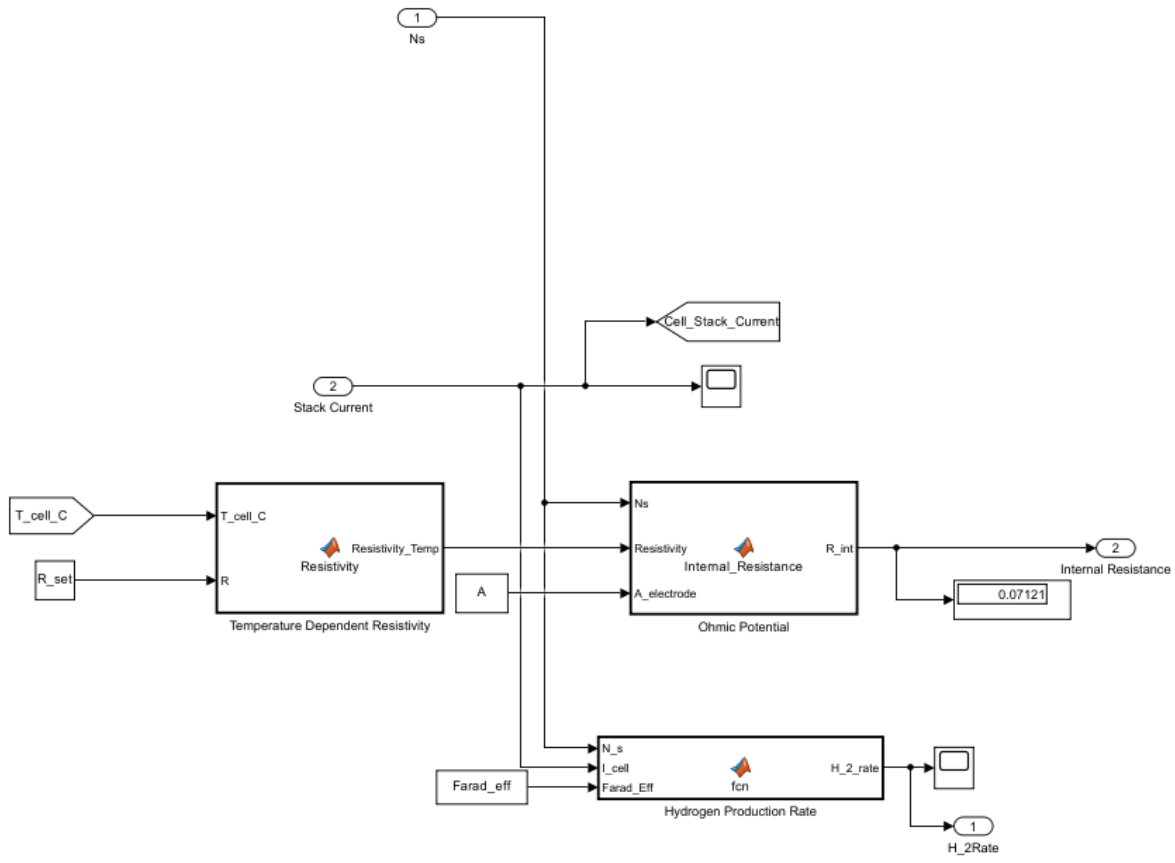

Figure A.6: Simulink model EL subsystem, chemical model subsystem, production rate subsystem.

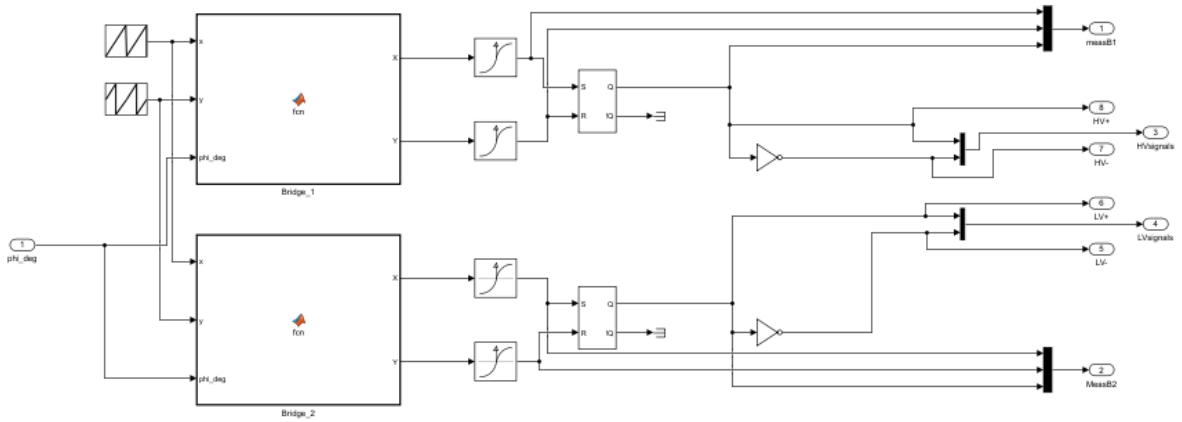

Figure A.7: Simulink model SPS subsystem.

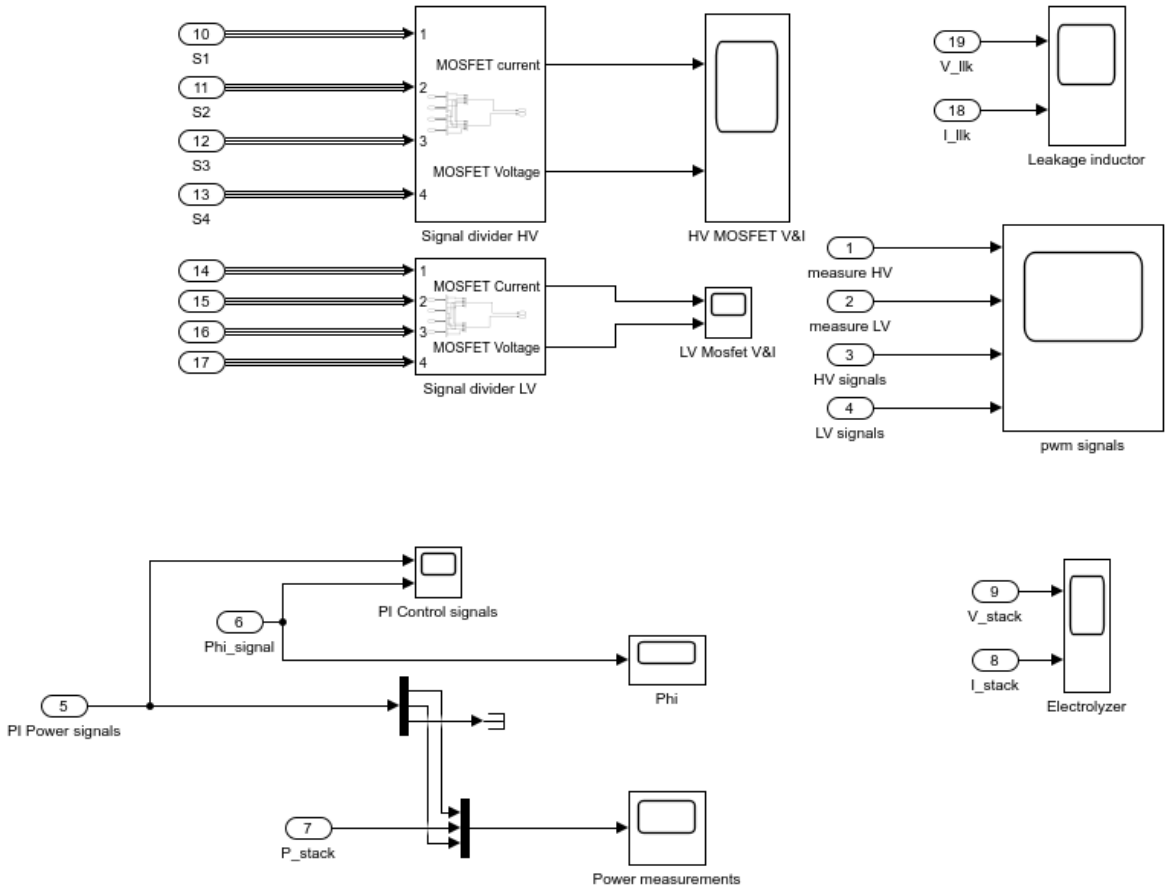

Figure A.8: Simulink model Scopes subsystem.

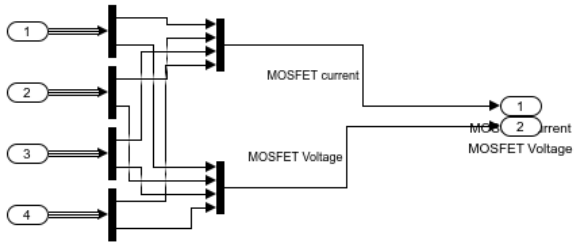

Figure A.9: Simulink model Scopes subsystem, mosfet division subsystem

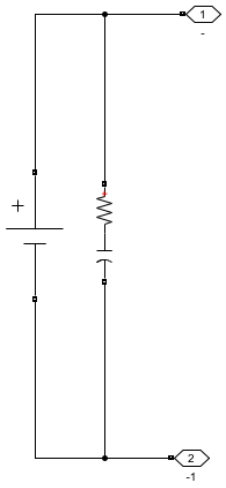

Figure A.10: Simulink model MVDC subsystem.

A.3. PLECS Model Initialization Code.

This section shows the code used to run before the PLECS based Simulink model.

```
%% PLECS BASED SIMULINK MODEL CODE TO RUN BEFORE RUNNING PLECS MODEL
% Made By N. Lock and R.S. Deshmukh
% version 20-7-2023
clear all
clc
close all

% Electrolyzer cell Modelling
% Number of series connected cells
N_s = 36;
% Number of series connected stacks.
N_series = 1;
% Number of parallel connected stacks.
N_par = 1;

% Step - 1 Modelling Reversible Voltage of the cell.

% Cell Temperature in Celsius
T_cell_C = 15:10:65;

% Cell Temperature in Kelvin
T_cell = T_cell_C + 273.15; % K

% Constants
a_rev = [1.5421e-3, 9.526e-5, 9.84e-8];

% Temperature-dependent reversible potential
U_rev_0 = (1.5184 - a_rev(1)*T_cell + a_rev(2)*log(T_cell).*T_cell
+ a_rev(3)*T_cell.^2);

% Alkaline electrolyte of KOH will be used therefore
% Molal Concentration of KOH 30 % wt

m = 7.64; % mol/Kg
a = -0.0151*m - (1.6788e-3)*m^2 + (2.2588e-5)*m^3;
b = 1 - (1.2062e-3)*m + (5.6024e-4)*m^2 - (7.8228e-6)*m^3;

% Vapor Pressure of H2O
P_v_H2O = exp(81.618 - 7699.7*T_cell.^-1 - 10.9*log(T_cell)
+ 9.589e-3*T_cell);

% Vapor Pressure of KOH
P_v_KOH = exp(2.302*a + b*log(P_v_H2O));

% Water Activity in KOH
a_H2O_KOH = exp((-51.92e-3)*m
+ (3.3e-3)*m^2 + (3.3177*m - 2.131*m^2)./T_cell);

% Reversible Potential
P_abs = 5;
R = 8.314463;
F = 96485;
```

```
z = 2;
U_rev = N_s*(U_rev_0
+ (R.*T_cell)./(z*F).*log(((P_abs -P_v_KOH).^1.5)./a_H2O_KOH));

% Step 2 - Activation Potential

% Set of constants given in the paper (Ursua 2012). These were obtained experimentally
% and with the help of MATLAB optimization and curve-fitting tools

S_set=  [25.23e-3, -234.0338e-6, 3.1832e-6];
T_set = [54.6185e-3, -2.4601e-3, 52.1217e-6];
V_set = [110.3623e-3, -1.6466e-3, 22.8382e-6];
W_set = [45.7027, 0.7781, -10.5743e-3];

S = S_set(1) + S_set(2).*T_cell_C + S_set(3).*T_cell_C.^2;
T = T_set(1) + T_set(2).*T_cell_C + T_set(3).*T_cell_C.^2;
V = V_set(1) + V_set(2).*T_cell_C + V_set(3).*T_cell_C.^2;
W = W_set(1) + W_set(2).*T_cell_C + W_set(3).*T_cell_C.^2;

% Capacitances associated with the double layer at electrodes
C_el_a = 0.6375;
C_el_c = 0.0307;

% Step - 3 Ohmic Losses

R_set = [59.5482e-6, -340.8224e-9, -106.9708e-6, 2.7075e-3];

% Electrode Area

A = 300e-4;

% Temperature dependent resistivity

r = R_set(1) + R_set(2).*(T_cell_C)
+ R_set(3)./(T_cell_C) + R_set(4)./(T_cell_C).^2;


% Script for plotting the characteristics
% Do not change the number of points. This will lead to power inaccuracies.
i_cell = 0:0.0001:180;
U_cell = zeros(length(T_cell_C),length(i_cell));
R_int = zeros(1,6);
for i = 1:length(T_cell_C)
    for j = 1:length(i_cell)
        % Internal Resistance
        R_int(1,i) = N_s*r(i)/A;
        %Ohmic Potential
        U_ohm = i_cell(j)*R_int(1,i);
        %Activation currents
        i_act_anode = i_cell(j);

        i_act_cathode = i_act_anode;

        U_act_anode= N_s*S(i)*log(i_act_anode/(T(i)) + 1);

        U_act_cathode= N_s*V(i)*log(i_act_cathode/(W(i)) + 1);
```

```
        U_cell(i,j) = N_series*(U_rev(i)
        + U_act_anode + U_act_cathode + U_ohm);
    end
end
%-----------------------------------------%
% Converter Parameters
%-----------------------------------------%

% DC Link Input Voltage

V_DC = 1400;

%Input DC Link Capacitance

C_in = 100e-6;
C_in_ESR = 1e-3;

%Output Capacitance

C_out = 200e-6;
C_out_ESR = 1e-3;

% Rated Power/Base Power for the pu plotting
P_base = 10e3;

% Output Voltage
V_out = 70;

% Primary to Secondary Turns Ratio
N = V_DC/V_out;

% Switching Frequency

fsw = 20e3;

% Carrier Phase Shift

phi_carrier = 180;

% PI Controller Gains

Kp = 0.0007;
Ki = 1200;

% Controller Limits for Phase Shift Angle

Upper_phi = 89;
Lower_phi = -89;

%Series Inductance
R_L = 1e-3;
order_mag = 1e-6;
t_step_max = 1e-7;
t_start = 0;
t_samp = 1/(2*fsw);
```

```
t_stop = 0.05;
L_s = 500e-6;
n = V_out/V_DC;
Ts = 1/fsw;
phi_init = 25;
d = phi_init/180;
Llk = V_DC*V_out*d*(1-d)/(2*n*P_base*fsw);
Llk2 =  500e-6;
C_o = V_DC*d^2*Ts^2*((1-d)+d^2/4)/(4*Llk*n);
c_o2 = 1e-3;
V_stack = 70;
V_DC = 1400;
P_cell = U_cell(1,:).*i_cell;
Deter = sqrt((-1)^2 -
8 * (U_cell(1,:).*i_cell*Llk*fsw./(V_DC*U_cell(1,:)*N)));
% Correct solution
D = abs(0.5*(1 - Deter));

% Converting the calculated phase shift ratio into phase angle in radians.
phi_1 = D*180;

%added for PI control
phi_up = 45; %degrees, upper bound saturator
phi_low = 0; %degrees, lower bound saturator
K_p = 10.01e-3; %Kp value PI
K_i = 2000; %Ki value PI
```

A.4. PLECS Model Screenshots

In this section, screenshots for the PLECS based Simulink model are presented.

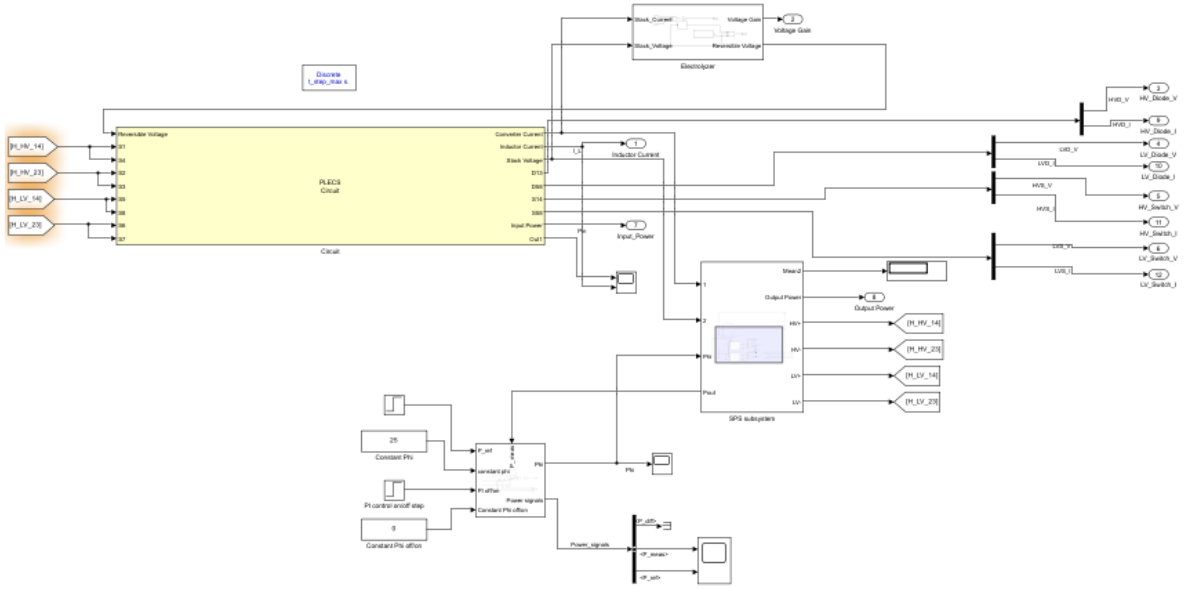

Figure A.11: PLECS model overview.

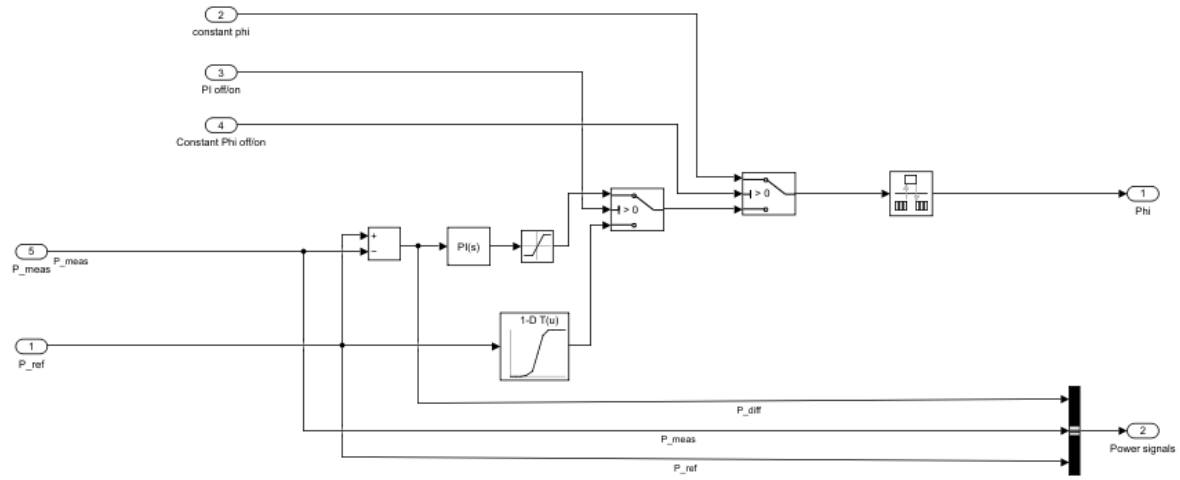

Figure A.12: PLECS Control subsystem

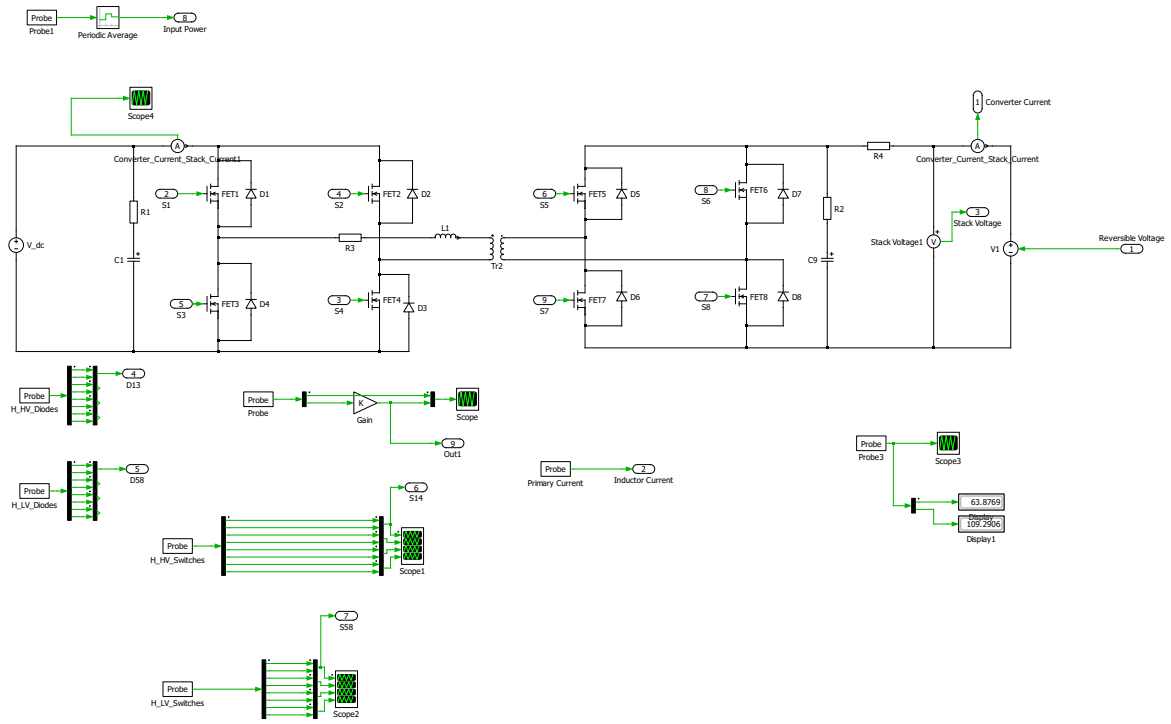

Figure A.13: PLECS Electrical subsystem.

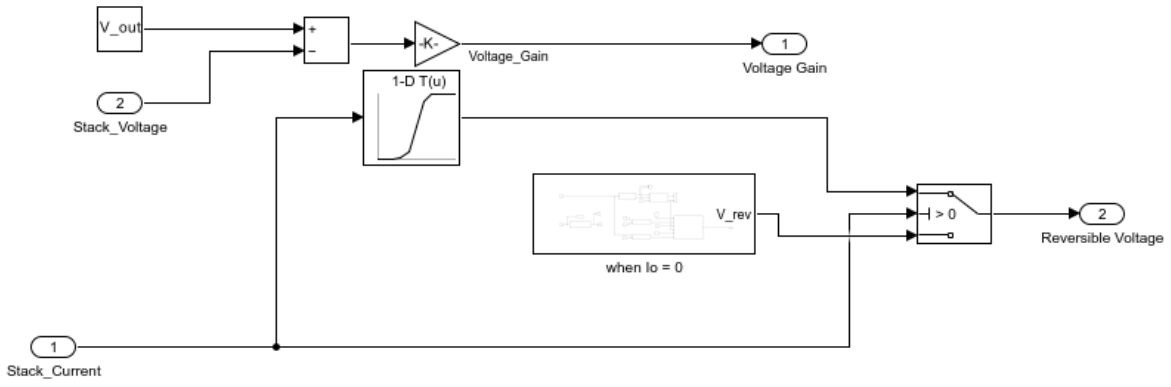

Figure A.14: PLECS Electrolyzer subsystem.

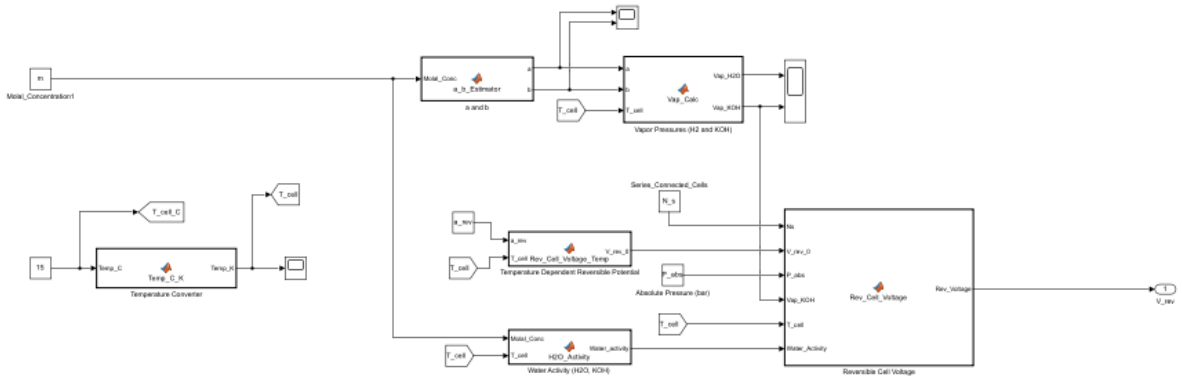

Figure A.15: PLECS Electrolyzer subsystem, chemical model.

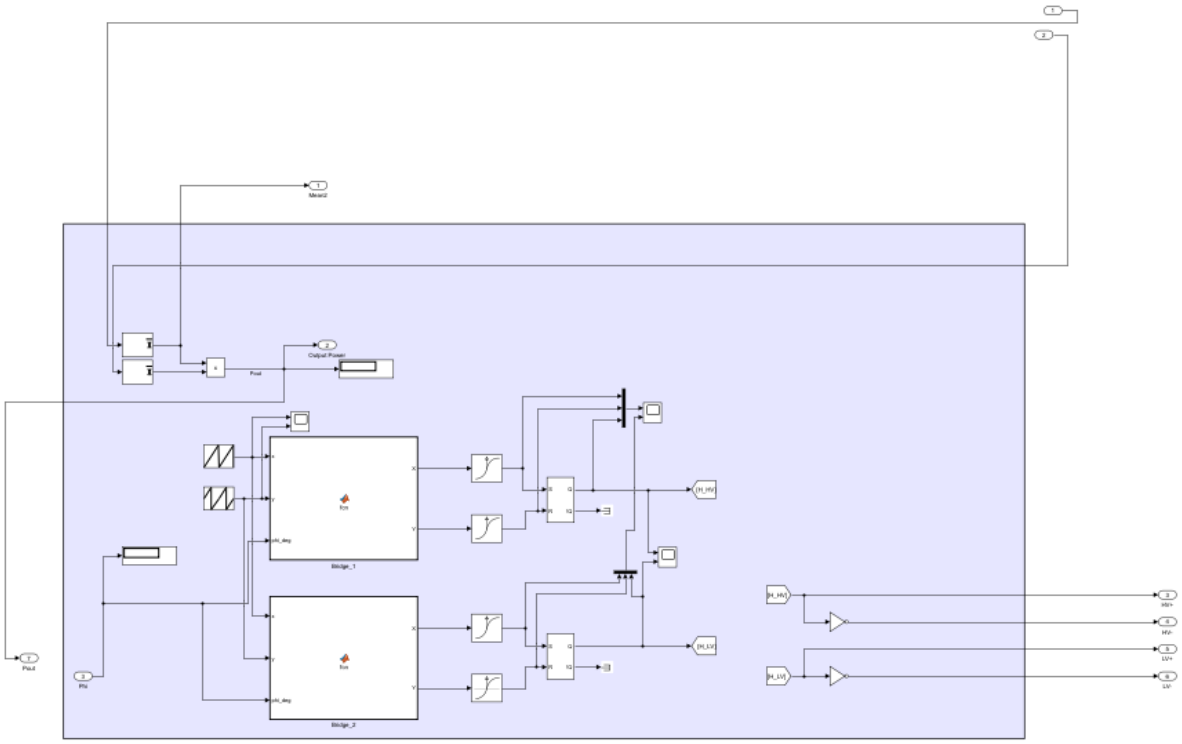

Figure A.16: PLECS SPS subsystem.

A.5. OPAL RT Model Code

In this section, the code used for the OPAL-RT model is presented. This code is to be put in via Model setting > Model properties > Callback > PreLoadFcn in the Simulink environment. Similar to the other codes, this code works as an initialization function.

```
%% OPAL RT CODE TO PLACE IN:  Model setting > Model properties > Callback > PreLoadFcn
% Made By N. Lock and R.S. Deshmukh
% version 1-9-2023
% Code nearly identical to PLECS modeling, mainly serves to add in the vectors of Power to phase and

% Electrolyzer cell Modelling
% Can be divided into modelling 4 types of voltages or overpotentials.
% Reversible Voltage (Thermodynamic Effect)
% Activation Potential
% Ohmic overpotential
% 5 kW Alkaline cell cell example.

% Number of series connected cells
N_s = 36;

% Number of series connected stacks.
N_series = 1;

% Number of parallel connected stacks.
N_par = 1;

% Step - 1 Modelling Reversible Voltage of the cell.
%Cell Temperature in Celsius
T_cell_C = 15:10:65;

% Cell Temperature in Kelvin
T_cell = T_cell_C + 273.15; % K

% Constants
a_rev = [1.5421e-3, 9.526e-5, 9.84e-8];

% Temperature dependent reversible potential
U_rev_0 = (1.5184 - a_rev(1)*T_cell + a_rev(2)*log(T_cell).*T_cell + a_rev(3)*T_cell.^2);

% Alkaline electrolyte of KOH will be used therefore
% Molal Concentration of KOH 30 % wt
m = 7.64; % mol/Kg
a = -0.0151*m - (1.6788e-3)*m^2 + (2.2588e-5)*m^3;
b = 1 - (1.2062e-3)*m + (5.6024e-4)*m^2 - (7.8228e-6)*m^3;

% Vapor Pressure of H2O
P_v_H2O = exp(81.618 - 7699.7*T_cell.^-1 - 10.9*log(T_cell) + 9.589e-3*T_cell);

% Vapor Pressure of KOH
P_v_KOH = exp(2.302*a + b*log(P_v_H2O));

% Water Activity in KOH
a_H2O_KOH = exp((-51.92e-3)*m + (3.3e-3)*m^2 + (3.3177*m - 2.131*m^2)./T_cell);

% Reversible Potential
```

```
P_abs = 5;
R = 8.314463;
F = 96485;
z = 2;
U_rev = N_s*(U_rev_0 + (R.*T_cell)./(z*F).*log(((P_abs -P_v_KOH).^1.5)./a_H2O_KOH));

% Step 2 - Activation Potential
% Set of constants given in the paper by Ursua. These were obtained experimentally
% and with the help of MATLAB optimization and curve-fitting tools
S_set=  [25.23e-3, -234.0338e-6, 3.1832e-6];
T_set = [54.6185e-3, -2.4601e-3, 52.1217e-6];
V_set = [110.3623e-3, -1.6466e-3, 22.8382e-6];
W_set = [45.7027, 0.7781, -10.5743e-3];
S = S_set(1) + S_set(2).*T_cell_C + S_set(3).*T_cell_C.^2;
T = T_set(1) + T_set(2).*T_cell_C + T_set(3).*T_cell_C.^2;
V = V_set(1) + V_set(2).*T_cell_C + V_set(3).*T_cell_C.^2;
W = W_set(1) + W_set(2).*T_cell_C + W_set(3).*T_cell_C.^2;

% Capacitances associated with the double layer at electrodes
C_el_a = 0.6375;
C_el_c = 0.0307;

% Step - 3 Ohmic Losses
R_set = [59.5482e-6, -340.8224e-9, -106.9708e-6, 2.7075e-3];

% Electrode Area
A = 300e-4;

% Temperature dependent resistivity
r = R_set(1) + R_set(2).*(T_cell_C) + R_set(3)./(T_cell_C) + R_set(4)./(T_cell_C).^2;

% Do not change the number of points. This will lead to power inaccuracies.
i_cell = 0:0.01:180;
U_cell = zeros(length(T_cell_C),length(i_cell));
R_int = zeros(1,6);

for i = 1:length(T_cell_C)
    for j = 1:length(i_cell)
        % Internal Resistance
        R_int(1,i) = N_s*r(i)/A;
        %Ohmic Potential
        U_ohm = i_cell(j)*R_int(1,i);
        %Activation currents
        i_act_anode = i_cell(j);

        i_act_cathode = i_act_anode;

        U_act_anode= N_s*S(i)*log(i_act_anode/(T(i)) + 1);

        U_act_cathode= N_s*V(i)*log(i_act_cathode/(W(i)) + 1);

        U_cell(i,j) = N_series*(U_rev(i) + U_act_anode + U_act_cathode + U_ohm);
    end
end

Llk = 586e-6;
```

```
fsw = 20e3;
N = 1400/70;
V_DC = 1400;
P_cell = U_cell(1,:).*i_cell;
Deter= sqrt((-1)^2 - 8*(U_cell(1,:).*i_cell*Llk*fsw./(V_DC*U_cell(1,:)*N)));
% Correct solution
D = abs(0.5*(1 - Deter));
% Converting the calculated phase shift ratio into phase angle in radians.
phi_1= D*180/360;
```

A.6. OPAL RT Model Screenshots

In this section, screenshots for the OPAL-RT model are presented.

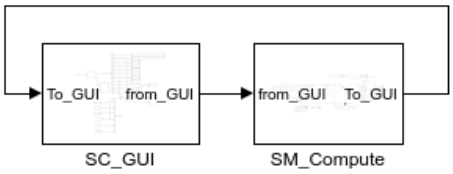

Figure A.17: OPAL-RT model top overview.

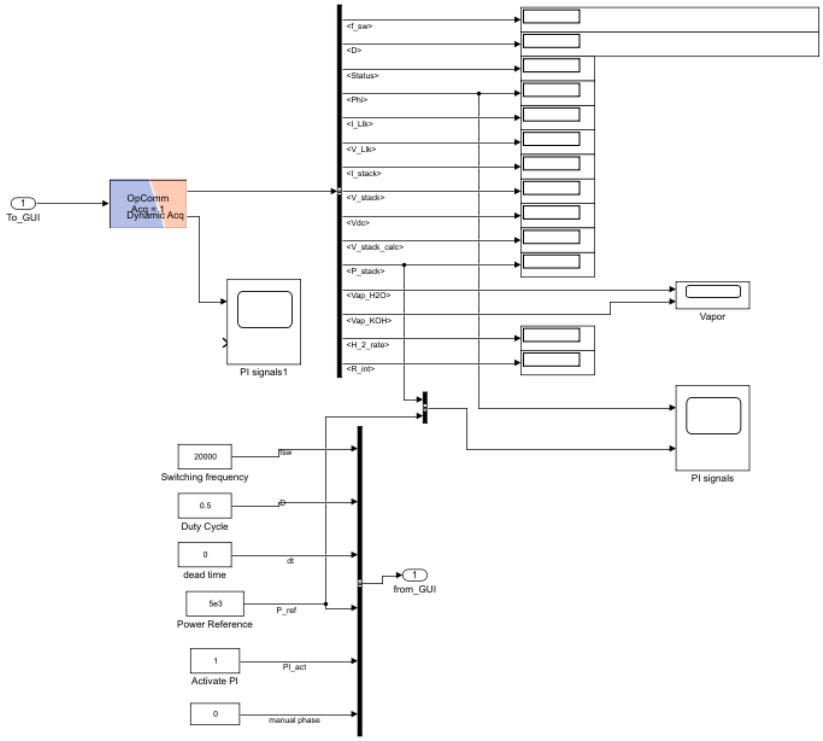

Figure A.18: OPAL-RT SC_GUI subsystem.

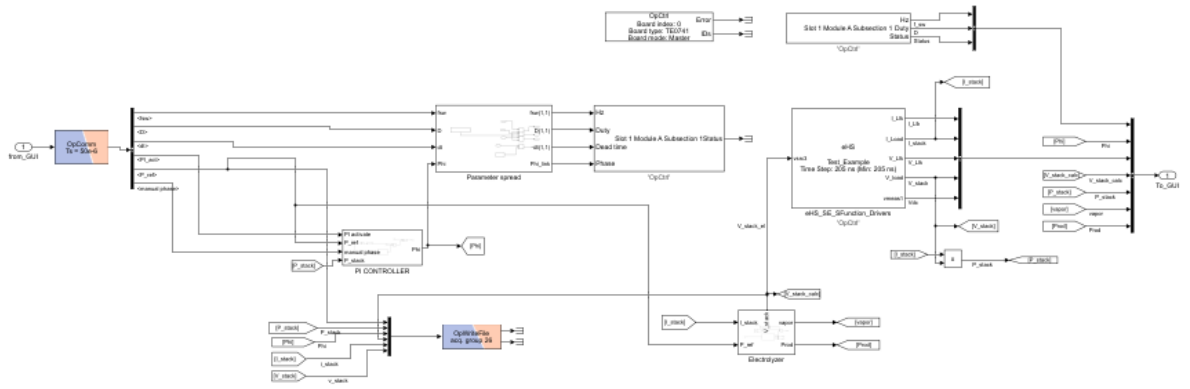

Figure A.19: OPAL-RT SM_COMPUTE subsystem.

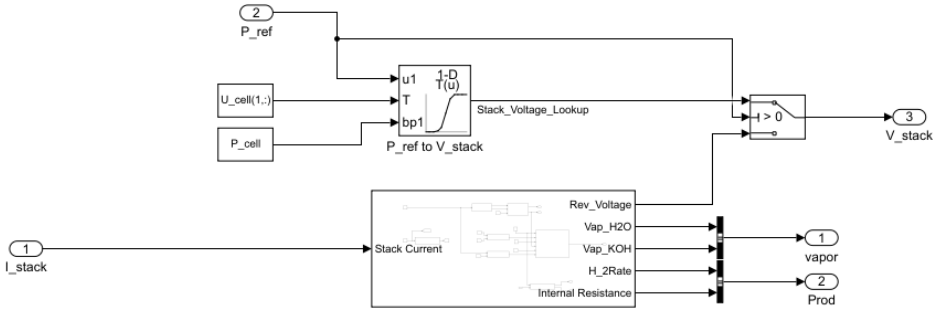

Figure A.20: OPAL Electrolyzer subsystem.

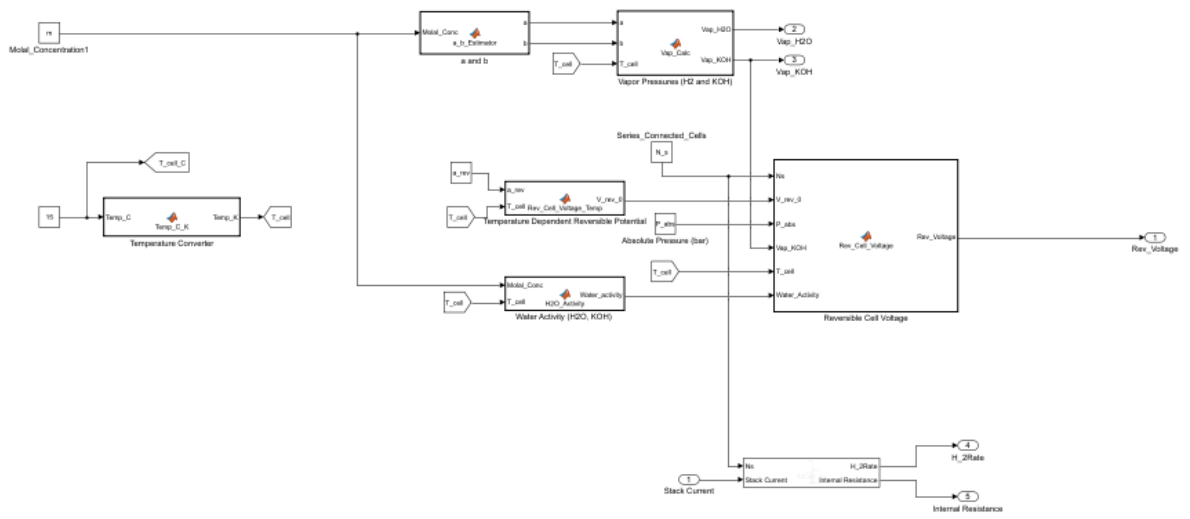

Figure A.21: OPAL Electrolyzer subsystem, chemical model.

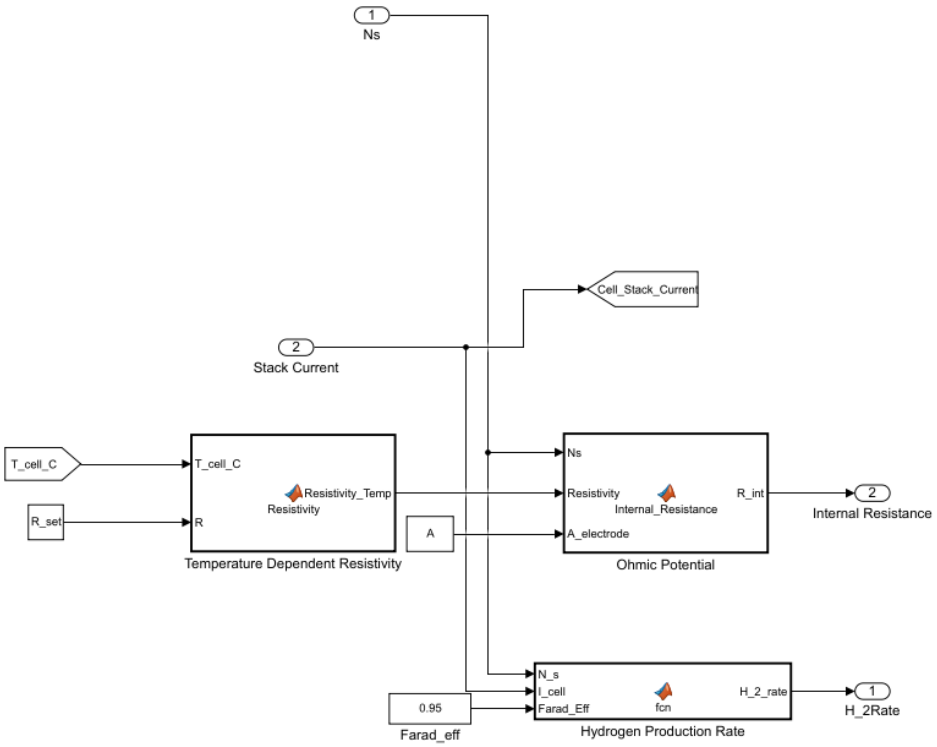

Figure A.22: Chemical subsystem continued.

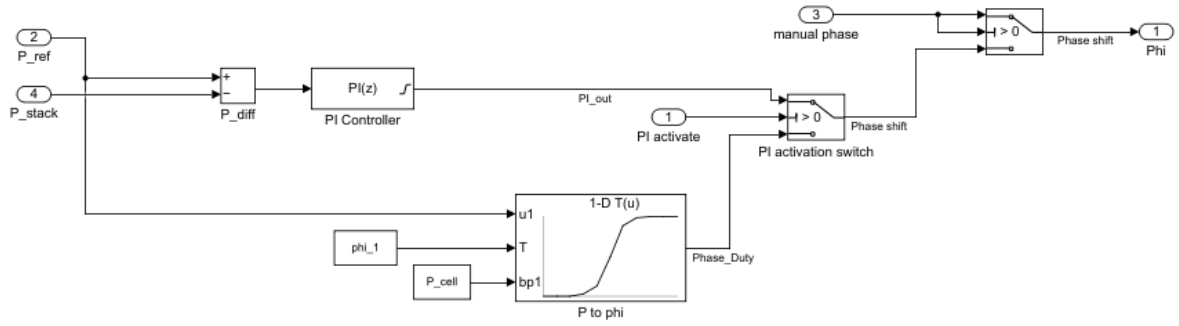

Figure A.23: OPAL-RT control subsystem.

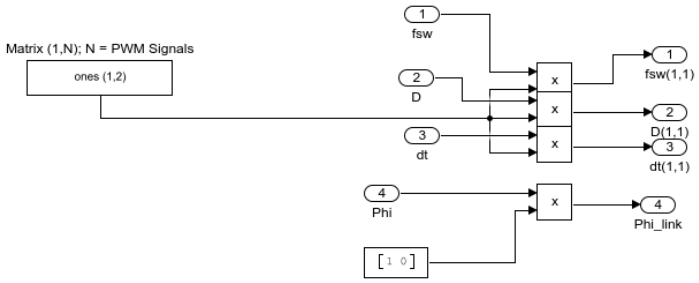

Figure A.24: OPAL-RT subsystem for input values of PWMout.

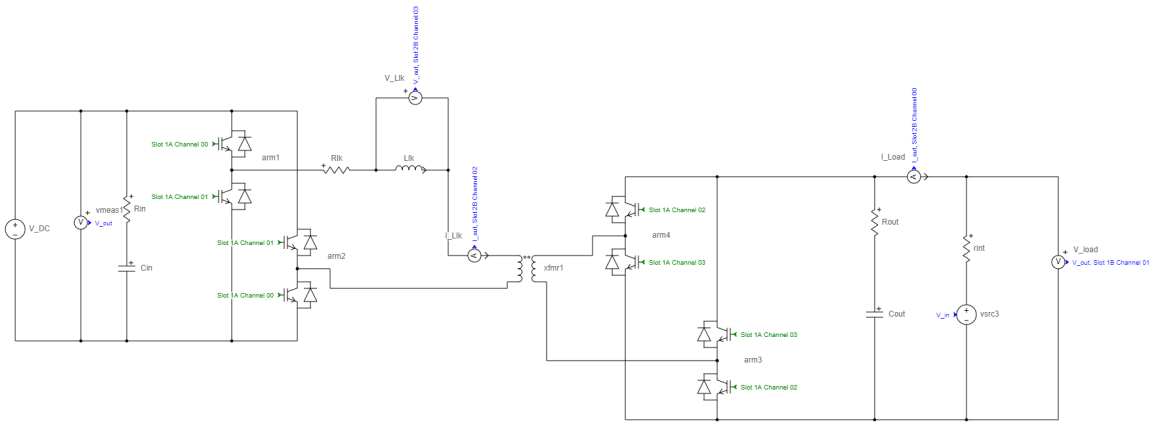

Figure A.25: eHS electrical schematic with channel routing.

B

How to run the OPAL-RT Model

This appendix covers the steps to run the model. Once the installation of the RT-Lab, eHS Toolbox, and Scopeview software is complete, the model can be run. If these programs have not been installed yet, please consult the OPAL-RT website for guidance. A package containing the files can be requested via R. S. Deshmukh: R.S.Deshmukh@tudelft.nl or via the author N. Lock: n.lock@tudelft.nl.

Start RT-Lab and create a workspace or choose an existing one.

Create a new folder in the workspace by selecting "create a new project" on the left. Give it a name and create an empty project by clicking "next" and then "finish". Double-click on the named folder to open the project. Import the models by right-clicking the folder and selecting "import..".

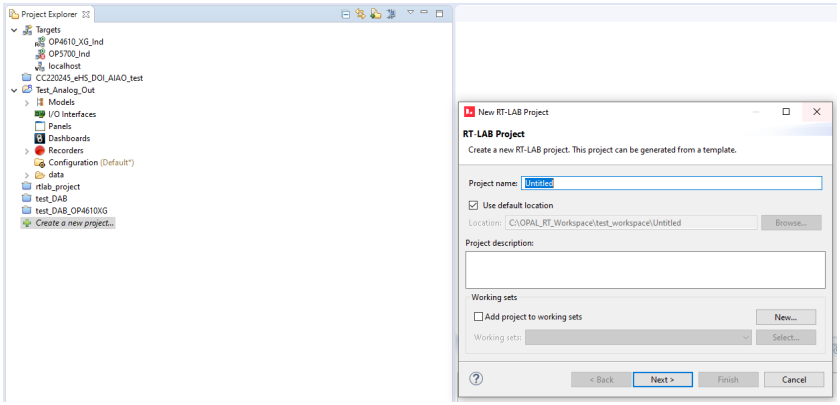

Figure B.1: Create a project.

Select "existing projects into workspace", click "Next" and choose the root directory of the obtained files.

Once the models are imported, check whether the bitstream files (.bin and .fsd) are present in the workspace folder in the Windows shell menu. If these files are not yet there, copy them and place them inside the project folder.

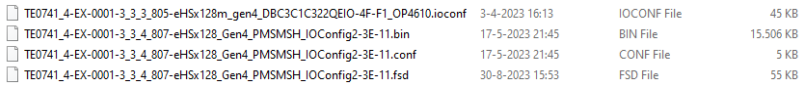

Figure B.2: Check the .bin files.

Right-click on the model name and choose to edit with Matlab 2021b. Or double-click the model name and click "edit the model" on the right. Make sure this particular Matlab version is installed.

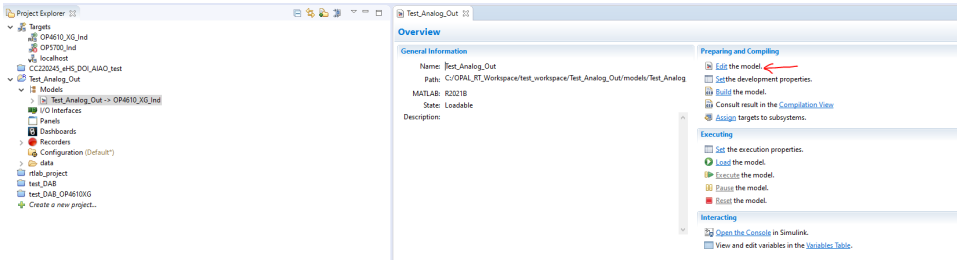

Figure B.3: Edit the model.

Check the model to see if every subsystem is included. Screenshots with the containment of the model can be found in appendix A.6. Check whether the gate DI and measurement AO channels are the same as depicted in the screenshots via the PLECS toolbox. Ensure the model code is placed in model properties -> callbacks -> initFcn

Check whether the assignment of the groups for the "PWMout" and "PWMin" are for the correct subsections of the DO and DI signal groups.

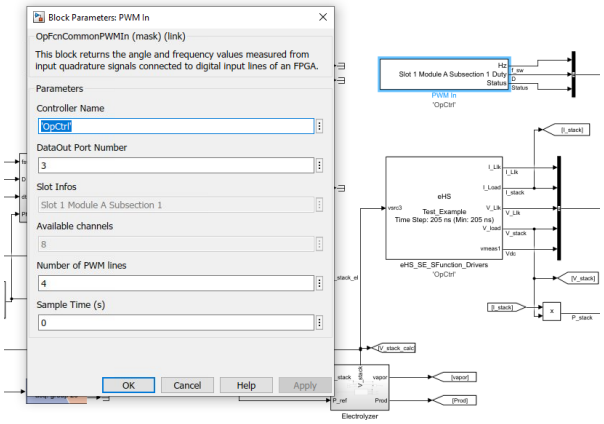

Figure B.4: PWMin settings.

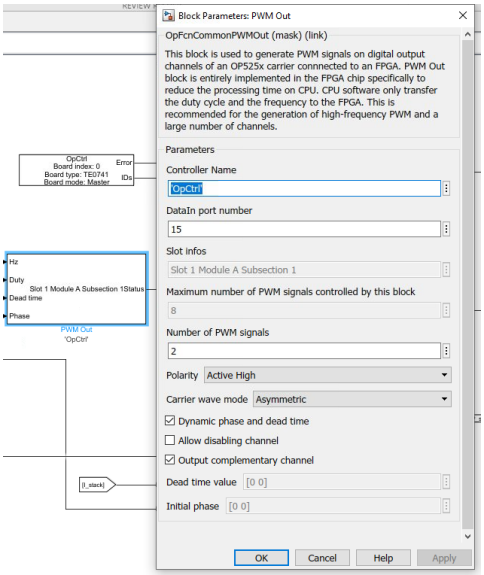

Figure B.5: PWMout settings.

Check whether the "OPctrl" block has the correct values.

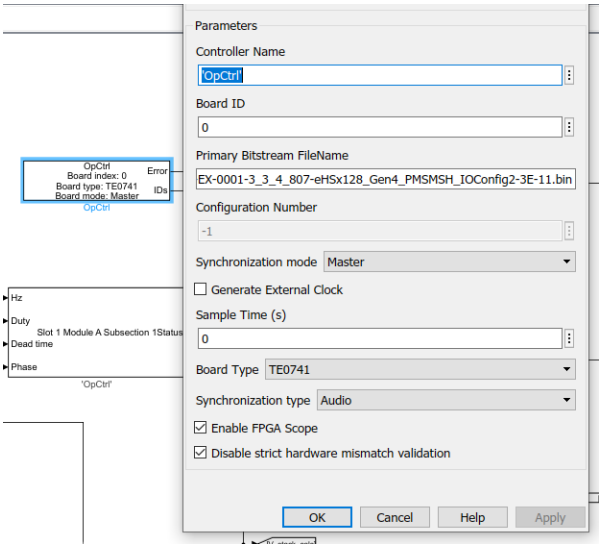

Figure B.6: OPcrtl settings.

Double click the eHS Toolbox subsystem to open it, go to firmware settings by clicking "simulate" and then "simulator setting" in the eHS toolbox. Check whether the .bin file which was earlier moved is selected t the FPGA firmware tab. If not go to "simulate and then "firmware manager" to assign the .bin file to the settings.

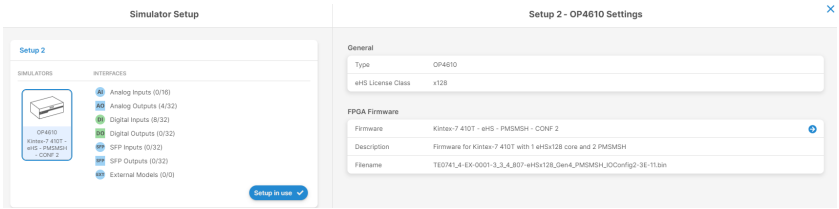

Figure B.7: Simulator setup in eHS

Check the eHS schematic to see if Slot 1A channels 00, 01, 02, and 03 are assigned to the gates and Slot 2B 00, 01, 02, and 04 are assigned to the A and V measurement blocks.

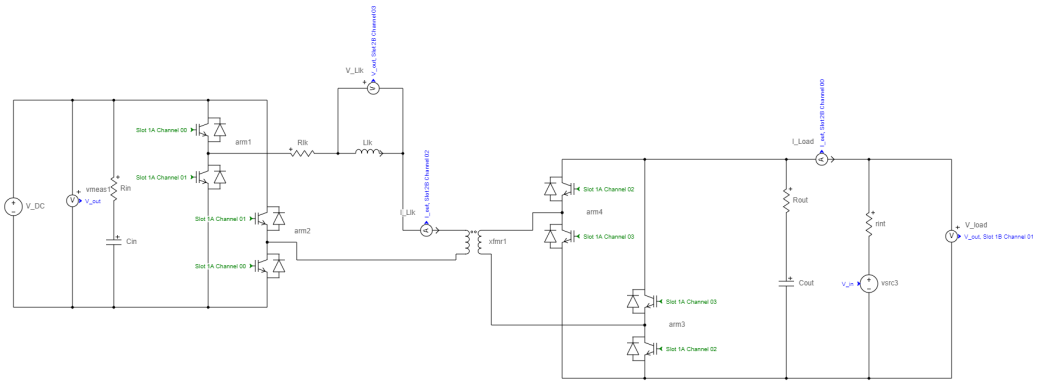

Figure B.8: eHS channel assignment.

Save the eHS model by clicking "file" and "save", in the Simulink environment, right-click on the eHS block and go to "eHS Block" -> "update block" to update the block. Compile the model by running the Simulink model with the green play button. once the model starts running stop the simulation immediately by pressing the square stop button. After that, save the model in the Simulink environment by clicking the "save" button next to the Library Browser. Close the Simulink environment.

Assign the OP4610XG as a target by double clicking the OP4610_XG_ind button at the targets tab in RT-Lab. Make a connection. The status of the connection can be checked by pinging the IP address via the CMD window in Windows.

In the model overview, check "hardware synchronized" in the execution tab.

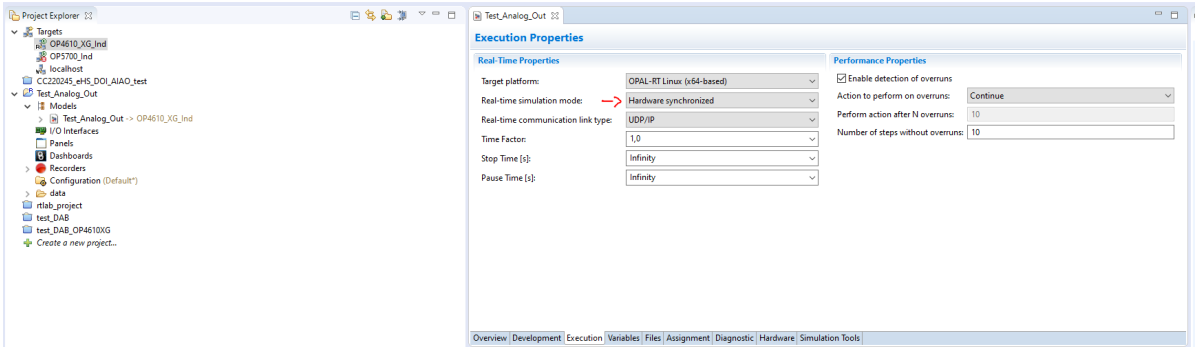

Figure B.9: Check hardware synchronized.

Right-click the project folder and select "simulation -> "Build". This will build the model, this process takes roughly 4 minutes.

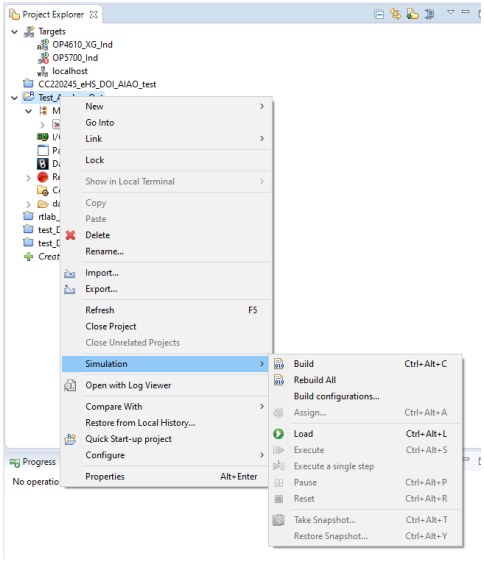

Figure B.10: Build, load, and execute the model via this drop-down menu.

Once the model is built, right-click the project folder and choose "Load", this will load the model to the OP4610XG hardware. The loading process will open the Simulink environment with the SC_GUI subsystem displayed. Do not click inside the model to prevent errors.

Once the command window shows the loading process is complete, right-click the project folder in RT-LAB, go to "simulation" and click "execute". Inside the Simulink environment, the displays will show numbers. The input variables can be double-clicked to change their values. The scopes can be opened to see the PI signals.

Whilst running the simulation, click the up arrow at the right of your Windows toolbar, right-click on the RT-Lab logo, and open Scopeview.

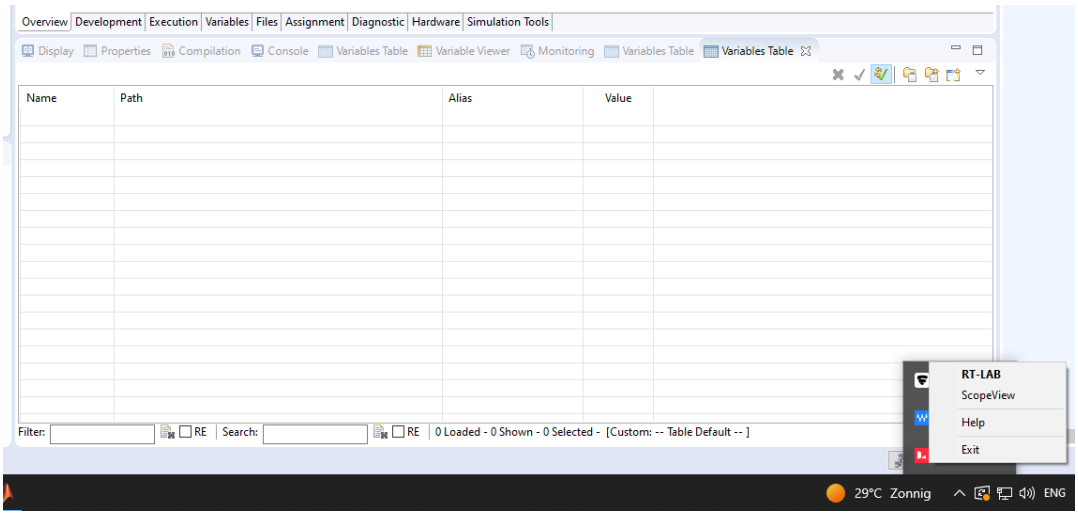

Figure B.11: Open Scopeview.

Assign the data source by putting in the IP address of the OP4610XG in the data logger tab by clicking "data source" -> "load". Choose "fetch signal groups" and pick the first one in the drop-down menu.

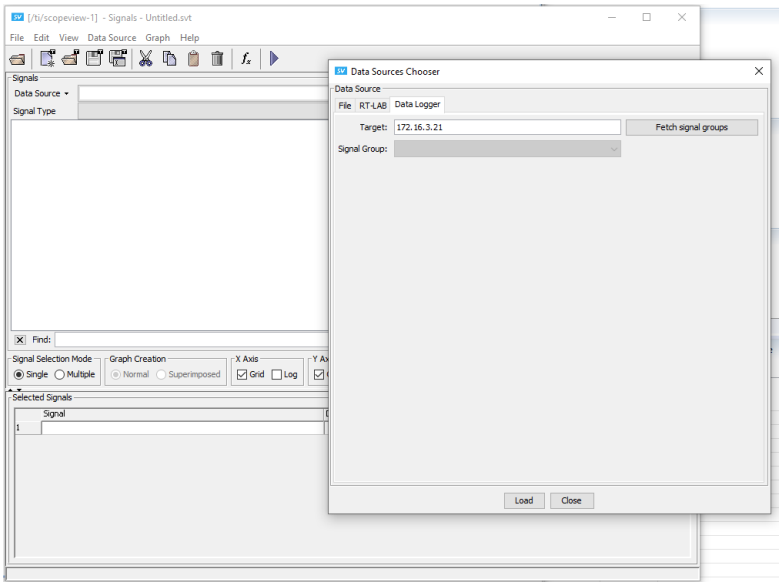

Figure B.12: Datalog tab of Scopeview, type the IP address here and fetch the signals.

Click on the AO port signals that are used in the eHS toolbox (AO CH00, CH01, CH02, CH03). By clicking this, scopes pop up on the other Scopeview screen.

Make sure that the trigger signal is set to AO00 and the trigger value is set to 0.0001.
Click the "run" button (play triangle) in Scopeview whilst the simulation is running in RT-Lab. The scopes should now be filled with signals.

After your experiment is completed, right-click the project folder in the RT-Lab and click "stop simulation". Then right-click the project folder again and close the project. Lastly, close RT-Lab.

C

Occurred errors & troubleshooting

This appendix covers a collection of errors that were found during the modeling of the Real-Time Digital Twin via RT-LAB. Troubleshooting ideas and solutions are provide for every type of error mentioned.

Compiling & Building the model
Whenever the model refuses to build, make sure all files associated with the model are not opened or in use. Save and close the Matlab and Simulink environments to ensure a correct build.

Always check whether the right .bin file containing the bitstream file is assigned at the eHS Toolbox and OPctrl blocks. The bitstream file should be placed in the model folder together with the .fsd file.

Make sure that the initialization code is located in model properties -> callbacks -> initFcn to ensure that all requisites are ready when simulating. Compiling the model in the Simulink environment is recommended to see if there are any variables or connections missing.

If a new model is made, always check whether SM_"name" is used in the name for the computational subsystem and SC_"name" is used for the subsystems. SS_ is used for the leader-follower type of subsystems of the SM_ subsystems. An SS_ subsystem should be assigned a core different from the SM_ subsystem.

Loading the model
Before using the "load model" function, always check whether the latest version of the model is built. The build statistics and specifications are depicted in the command log.

When loading fails, check whether the connection with the hardware is still present. At the top left of the RT-Lab software, the status of the hardware is presented.

Running the model
Check whether the "hardware synchronized" simulation button is marked in the model menu when it is desired to run with the OPAL-RT hardware. If the simulation is to be run in Simulink, this button should be blank.

If a previous version of the simulation was not closed properly via "stop simulation" and the RT-Lab was closed, trying to run a new model on the hardware will fail. Reset the hardware via the button on the front or, if possible, still try to stop the simulation via RT-Lab.

Always make sure "Disable strict hardware mismatch" is checked. Leaving this unchecked may leave unwanted errors when running.

Scopeview
If the Scopeview environment does not show any signals. Check in the .fsd file whether any other DO, DI, AO, or AI ports are set to 'true'. Only turn on the signals that will present data. Depending on which one is set to true or false, a trigger signal is chosen which affects when the data is read and displayed.

Another possible solution for when Scopeview is not portraying any signals is to check via SC_GUI via display whether the signal is displaying values larger than the trigger value. Signals with zero change will not be triggered. The trigger function should be turned on with an automatic trigger. Select an appropriate value to trigger for depending on the signal amplitude.

No signals displayed in Scopeview can also be caused due other signals not being changed. Sometimes the reference power signal was changed in order to read the AO signals.

If the signals come in with the wrong magnitude, check the gains set for them via the eHS Toolbox. If the values are larger than expected, the gains will not reduce them enough to prevent saturation or invisibility.

Signals behave with unexpected forms
When the signals give unexpected or incorrect waveforms, check every value of each piece modeled in eHS and Simulink. It is likely that one of the devices modeled is not assigned the right value. Redo the (electrical) connections if this does not work.
Check the pin assignment in the eHS toolbox and compare it with the pin assignments of "PWMin" and "PWMout". If the wrong DI pin is matched to the gate, the AO signals will perform very oddly.

Make sure that the acquisition numbers of "PWMin" and "PWMout" match the right groups to ensure good signal transactions between DO and DI channels.

Ensure that the transformer magnetizes, if the values of L_{m} and R_{m} are assigned incorrectly, the LV side will not work.

Errors due to modeling functionalities
When the logs say anything about the models functionalities check to see whether any connections are missing or need rerouting.

If this does not help, consult with the OPAL-RT service employees to check whether it is available on the bitstream file.

When in doubt
When in doubt, always fully close the models and close RT-Lab. Restart RT-Lab and try again. If any function were messed up, it is likely not saved when closing and restarting. This provides another chance to find out where it went wrong.

D

Conference Paper

Part of the contents of this thesis are implemented within the conference paper "Implementation of Real-Time Digital Twin of Dual Active Bridge Converter in Electrolyzer Applications" by the author of the thesis and Rohan Shailesh Deshmukh, Gautam Rituraj, Hani Vahedi, Aditya Shekhar, and Pavol Bauer of the DCE&S department of EEMCS TU Delft. This paper is also cited multiple times within this thesis. The paper has been accepted for IECON2023, the 49th annual conference of the IEEE Industrial Electronics Society. Which takes place from October 16 to October 19, 2023, at the Marina Bay Sands Expo and Convention Centre in Singapore. The paper is to be published in the last quarter of 2023.

Deshmukh, R. S. *et al.* Implementation of Real-Time Digital Twin of Dual Active Bridge Converter in Electrolyzer Applications (2023).